U. S. Department of Commerce
National Oceanic and Atmospheric Administration
National Weather Service
National Centers for Environmental Prediction
5200 Auth Road Room 207
Camp Springs, MD 20746

Technical Note

Optimum Discrete Interaction Approximations for wind waves.
Part 3: Generalized multiple DIAs.[†]

Hendrik L. Tolman [‡]

Environmental Modeling Center
Marine Modeling and Analysis Branch

October 2008

This page is intentionally left blank.

Abstract

The present report is the third in a series assessing the potential of the Discrete Interaction Approximation for representing nonlinear interactions in wind wave models. This study addresses generalization of the DIA with multiple representative quadruplets to arbitrary depth, and particularly focuses on scaling behavior of this DIA with respect to depth. Major findings are that (i) shallow water quadruplet layouts need to be considered explicitly to assure proper conservation characteristics of a DIA, (ii) full shallow water expressions are needed to retain realistic shallow water interaction shapes, (iii) separate scaling functions with appropriate shallow and deep asymptotic behavior are needed to obtain proper scaling behavior for arbitrary depth, (iv) the choice of the underlying definition of spectral space has a notable (numerical) impact on the resulting interactions. Experiments with numerical optimization show that (a) an optimized generalized DIA configured like the traditional DIA requires approximately twice the computing time of the latter, (b) generalizing the quadruplet layout increases the costs by an additional factor of just below two, and (c) that the costs of the optimized MDIA scales linearly with the number of representative quadruplet realizations.

As a side note that the assessment of the generalized multiple DIA, diffusion approaches to nonlinear interactions are addressed. It is shown that the traditional DIA with a quadruplet layout that is not resolved by the discrete spectral grid reduces to a simple diffusion operator that satisfies all conservation properties of the nonlinear interactions. A high-frequency filter based on such an approach is designed and optimized to be used in conjunction with the generalized multiple DIA, or with Neural Network Interaction Approximations.

This report is available as a pdf file from

<div align="center">

http://polar.ncep.noaa.gov/waves

</div>

Contents

This page is intentionally left blank.

1 Introduction

This study represents the third part of a study into the potential of the Discrete Interaction Approximation (DIA) to represent nonlinear interactions in a wind wave model. For a justification of this study reference is made to Tolman (2003, henceforth denoted as Part 1), Tolman (2005, henceforth denoted as Part 2) and to Tolman (2004) and Tolman and Krasnopolsky (2004). In Part 1 previously suggested modifications to the traditional DIA of Hasselmann et al. (1985) are evaluated using exact and approximated nonlinear interactions for selected test spectra. In Part 2 a more in-depth analysis of the behavior of various DIAs is presented. Instead of testing interaction approximations for selected spectra, a holistic approach is used where wave parameters resulting from model integration are optimized. It is shown that an advanced DIA optimized in this manner indeed can improve the accuracy of the wave model significantly, that is, will more closely reproduce wave model results as obtained with an exact interaction routine. The optimization in Part 2, however, was hampered by limits in the optimization procedures used. Particularly, using an unoptimized DIA implementation, in combination with a fairly simple genetic search algorithm, resulted in optimization experiments that pushed the limits of economical feasibility.

Considering the above, the study documented here is focused on the following issues. First, the basic DIA is reconsidered. The original formulation is based on a historical description of the wave field, and on the assumption of deep water. In present modeling approaches, in particular with limited water depths, this may no longer be the most appropriate approach. Second, previous diffusion approaches are considered briefly, Whereas such approaches may lack the desired accuracy, they may be considered as part of an multiple DIA to result in smoother and therefore faster integration. Finally, numerical optimization of the resulting multiple DIA is considered to obtain the most economical MDIA feasible. Parameter optimization of the resulting MDIA, using genetic or other approaches will be considered in the next report in this series.

In the previous parts of this study, the traditional spectral balance equation of Hasselmann (1960) is used, applied to deep water only. In such conditions, the evolution of the wave energy or variance spectrum $F(f, \theta)$ as a function of the spectral frequency f and direction θ can be expressed as

$$\frac{\partial F(f, \theta)}{\partial t} + \boldsymbol{c}_g \cdot \nabla F(f, \theta) = s_{in}(f, \theta) + s_{nl}(f, \theta) + s_{ds}(f, \theta) \ , \qquad (1.1)$$

where the right side of the equation represents the sources and sinks, consisting of wind input (s_{in}), nonlinear interactions (s_{nl}) and dissipation (s_{ds}) source terms. Furthermore, $\boldsymbol{c}_g$ is the group velocity with magnitude $c_g = \partial \sigma / \partial k$ and direction θ, and where $\sigma = 2\pi f$ and k $(\boldsymbol{k})$ is the wavenumber (vector).

Using the spectrum $F(f, \theta)$ has a historical background, and appears to be based on the fact that this spectrum [or at least its one-dimensional version $F(f)$] is naturally obtained from local time series observations of the water level elevation. However, the wave action, which is generally defined as $N = F/\sigma$ is the basic conserved quantity for waves propagating on mean currents and in shallow water (e.g., Bretherthon and Garrett, 1968), and spectral descriptions using the wavenumber vector $\boldsymbol{k}$ or wavenumber-direction space (k, θ) are more generally invariant with respect to limited depths. Note that the original expressions for nonlinear interactions are all expressed in terms of $n(\boldsymbol{k})$ [see Eq. (1.11)]. Because the present study is intended to ultimately replace the DIA in the WAVEWATCH III model (Tolman, 2002c; Tolman et al., 2002), the corresponding action balance equation will be used. This equation is based on the action spectrum $N(k, \theta) = F(k, \theta)/\sigma = c_g F(f, \theta)/(2\pi\sigma)$ and is given as

$$\frac{\partial N(k, \theta)}{\partial t} + \nabla_x \cdot \dot{\mathbf{x}} N(k, \theta) + \frac{\partial}{\partial k} \dot{k} N(k, \theta) + \frac{\partial}{\partial \theta} \dot{\theta} N(k, \theta) = S(k, \theta) , \qquad (1.2)$$

$$\dot{\mathbf{x}} = \mathbf{c}_g + \mathbf{U} , \qquad (1.3)$$

$$\dot{k} = -\frac{\partial \sigma}{\partial d} \frac{\partial d}{\partial s} - \boldsymbol{k} \cdot \frac{\partial \mathbf{U}}{\partial s} , \qquad (1.4)$$

$$\dot{\theta} = -\frac{1}{k} \left[\frac{\partial \sigma}{\partial d} \frac{\partial d}{\partial m} - \boldsymbol{k} \cdot \frac{\partial \mathbf{U}}{\partial m} \right] , \qquad (1.5)$$

where d is the mean water depth, $\mathbf{U}$ is the mean current velocity, s is a coordinate in the direction θ and m is a coordinate perpendicular to s, and where $S(k, \theta) = c_g s(f, \theta)/(2\pi\sigma)$ represents the sum of the three basic source terms in Eq. (1.1). The corresponding dispersion relation is given as

$$\sigma^2 = gk \tanh kd . \qquad (1.6)$$

Note that σ represents that intrinsic or relative frequency, as observed when moving with the velocity $\mathbf{U}$, and where the frequency as observed on a fixed location ω is given by the Doppler equation

$$\omega = \sigma + \boldsymbol{k} \cdot \mathbf{U} . \qquad (1.7)$$

Note, furthermore, that in WAVEWATCH III the discrete wavenumber grid is a function of the local water depth d, in such a way that the corresponding discrete frequency grid is invariant (Tolman and Booij, 1998), and that the frequency grid is logarithmic, i.e.

$$\sigma_{i+1} = X\sigma_i , \qquad (1.8)$$

where X is a constant factor.

The nonlinear interactions, which are the centerpiece of the present study, describe the resonant exchange of energy, momentum and action between a "quadruplet" of four spectral components with wavenumber vectors $\boldsymbol{k}_1$ through $\boldsymbol{k}_4$ and (radian) frequencies σ_1 through σ_4 ($\sigma = 2\pi f$). These satisfy the resonance following conditions (Hasselmann, 1962, 1963) :

$$\boldsymbol{k}_1 + \boldsymbol{k}_2 = \boldsymbol{k}_3 + \boldsymbol{k}_4 \quad , \tag{1.9}$$

$$\sigma_1 + \sigma_2 = \sigma_3 + \sigma_4 \quad . \tag{1.10}$$

The interactions are conventionally expressed in terms of the rate of change of the action spectrum $n(\boldsymbol{k}) \equiv F(\boldsymbol{k})/\sigma$ as

$$\begin{aligned}
\frac{\partial n_1}{\partial t} &= \iiint G\left(\boldsymbol{k}_1, \boldsymbol{k}_2, \boldsymbol{k}_3, \boldsymbol{k}_4\right) \, \delta_k \, \delta_\sigma \\
&\times \quad \left[n_1 n_2 \left(n_3 + n_4\right) - n_3 n_4 \left(n_1 + n_2\right)\right] \, d\boldsymbol{k}_2 \, d\boldsymbol{k}_3 \, d\boldsymbol{k}_4 \quad ,
\end{aligned} \tag{1.11}$$

where n_i is the action density at component i, $n_i = n(\boldsymbol{k}_i)$, G is a complex coupling coefficient (Webb, 1978; Herterich and Hasselmann, 1980), and δ_k and δ_σ are delta functions corresponding to the resonance conditions (1.9) and (1.10).

The DIA represents a massive simplification of these exact interactions. Originally (Hasselmann et al., 1985) the DIA is derived for the spectrum $F(f, \theta)$ in deep water. Since then, forms for other spectral descriptions and for shallow water have been suggested. These will be discussed in some more detail as relevant for the present study in Section 2. Also discussed in the following sections will be shallow water considerations, and the possible addition of in particular diffusion-type operators to the DIA.

This page is intentionally left blank.

2 The Discrete Interaction Approximation

The concept of the DIA as introduced by Hasselmann et al. (1985, henceforth denoted as HHAB) hinges on three concepts. The first is the replacement of the continuous multi-dimensional integral (1.11) by a 'discrete interaction analogue'. The second is the assumption that the interaction can be represented by discrete interactions for a limited number of representative quadruplets (eventually reduced to a single configuration with several realizations). The third is the replacement of the complex coupling coefficient G by a simple scaling function and a proportionality constant. In the above paper, the third concept is not quite obvious, as the discrete analogue presented [HHAB, their Eq. (5.4)] already implicitly includes the scaling arguments needed to replace G with a simple constant. A detailed derivation can be found in Van Vledder (2002a). However, many of the basic concept of the DIA can be constructed in a simple way, avoiding detailed mathematical derivations.

Instead of the continuous integral (1.11), HHAB consider discrete changes in *total* action δn_i at four resonant wave components in an infinitesimal time interval Δt and an infinitesimal phase-space element $\Delta \boldsymbol{k}$. Applying the principle of detailed balance (Hasselmann, 1966; Komen et al., 1994, Section II.3.8) to the discrete action changes at the four components of the quadruplet,

$$-\delta n_1 = -\delta n_2 = \delta n_3 = \delta n_4 \quad . \tag{2.1}$$

Alternatively, Eq. (1.11) can be re-written in a similar symmetric form, as is the basis of most efficient exact algorithms. Retaining the product term in square brackets in Eq. (1.11) to retain the dependence of interactions on spectral shape, replacing the coupling coefficient G with a representative nondimensional strength C', and introducing a scaling function $B(f, \boldsymbol{k}, g)$ to assure proper dimensionality and scaling behavior of the resulting equations, the basic discrete analogue to Eq. (1.11) becomes

$$\begin{pmatrix} \delta n_1 \\ \delta n_2 \\ \delta n_3 \\ \delta n_4 \end{pmatrix} = \begin{pmatrix} -1 \\ -1 \\ 1 \\ 1 \end{pmatrix} C' B \left[n_1 n_2 (n_3 + n_4) - n_3 n_4 (n_1 + n_2) \right] \Delta \boldsymbol{k} \Delta t \quad , \tag{2.2}$$

Without further justification HHAB define the scaling function B as

$$B = g^{-8} f^{19} \quad , \tag{2.3}$$

which can be derived on dimensional grounds. Note that Eqs. (2.2) and (2.3) are equivalent to Eq. (5.4) of HHAB, but do not assume that $\boldsymbol{k}_1 = \boldsymbol{k}_2$ as in the latter

equation. Note, furthermore, that the product term P is regularly expressed in two equivalent ways

$$
\begin{aligned}
P_{1234} & = & n_1 n_2 (n_3 + n_4) - n_3 n_4 (n_1 + n_2) \\
& & n_1 n_3 (n_4 - n_2) + n_2 n_4 (n_3 - n_1) \quad .
\end{aligned}
\tag{2.4}
$$

The above approach can be expanded upon by considering two different contributions to the scaling function B,

$$
B = B_1 B_2 \quad , \tag{2.5}
$$

where B_2 represents the scaling behavior of the coupling coefficient G, which for deep water can be expressed as (e.g., Van Vledder, 2002a)

$$
B_2 = g^{-4} f^{12} \quad , \tag{2.6}
$$

and where B_1 represents the 'residual' scaling function, which on dimensional grounds becomes

$$
B_1 = g^{-4} f^7 \quad . \tag{2.7}
$$

The origin and form of B_1 will be discussed in more detail in Section 2.5.

Finally, the discrete changes of action δn_i can be converted to contributions to an action density source term $\delta S_{nl,i} = \delta S_{nl}(\boldsymbol{k}_i)$ by dividing them by the time increment Δt and by distributing them over a (local) phase space element $\Delta \boldsymbol{k}_i$.

$$
\delta S_{nl,i} = \frac{\delta n_i}{\Delta \boldsymbol{k}_i \Delta t} \quad , \tag{2.8}
$$

which, combined with Eqs. (2.2), (2.4) and (2.5) gives

$$
\begin{pmatrix} \delta S_{nl,1} \\ \delta S_{nl,2} \\ \delta S_{nl,3} \\ \delta S_{nl,4} \end{pmatrix} = \begin{pmatrix} -\Delta \boldsymbol{k}/\Delta \boldsymbol{k}_1 \\ -\Delta \boldsymbol{k}/\Delta \boldsymbol{k}_2 \\ \Delta \boldsymbol{k}/\Delta \boldsymbol{k}_3 \\ \Delta \boldsymbol{k}/\Delta \boldsymbol{k}_4 \end{pmatrix} C' \, B_1 B_2 \, P_{1234} \quad , \tag{2.9}
$$

In this context it is relevant to note that HHAB make a distinction between $\Delta \boldsymbol{k}$ being a discrete interaction phase-space element, whereas $\Delta \boldsymbol{k}_i$ represents the bins in which the changes are stored in the numerical model. HHAB assume that $\Delta \boldsymbol{k}$ and $\Delta \boldsymbol{k}_i$ are similar, and that $\Delta \boldsymbol{k}_i$ may vary in phase space. Finally, HHAB convert the description of the source term defined in terms of wave action and the wavenumber vector $\boldsymbol{k}$ to a source term for wave energy (variance) in terms of wave frequency f and direction θ by applying the appropriate Jacobian transformations.

HHAB consider deep water conditions only. For restricted water depths, the deep water DIA is typically rescaled by a constant factor, which is a function of the

relative mean water depth $\overline{k}d$. This approach was introduced in the WAM model (WAMDIG, 1988), and is based on the results of Hasselmann and Hasselmann (1981), and is generally used in third-generation wind wave models.

Several observations can be made concerning shallow water applications of the nonlinear interactions in general, and the DIA in particular. First, the underlying equations are applicable in restricted water depths, as long as the proper shallow water dispersion relation is used throughout (Herterich and Hasselmann, 1980; Hasselmann and Hasselmann, 1981). For the DIA, however, extensions to shallow water are not trivial. Particularly, the conservation properties of the interactions should be considered. The interactions conserve action, energy and momentum of the waves. The conservation of action becomes clear from the detailed balance principle for the basic equations like (1.11). Because the contributing spectral components satisfy resonance conditions, energy and momentum are also conserved (e.g., Hasselmann, 1963; Webb, 1978). In the DIA, the total action is conserved by design. However, in shallow water applications, the deep water dispersion relation is still used in determining the layout of the quadruplets, deep water Jacobians are still implicitly used in the equations, and deep water scaling arguments are used in B. Hence the link between conservation of action, energy and momentum may be lost, and none of these quantities are guaranteed to be conserved.

With this in mind, several details of the DIA will be considered in more detail in the following sections. Considered are representative quadruplets and spectral sampling (Section 2.1), effects of discretization of phase space (2.2), multiple DIAs (2.3), spectral descriptions (2.4), and scaling consideration (2.5). These sections are followed by a section in which the resulting DIA is tested (in particular for shallow water), and a conclusions section in which the final DIA is summarized.

2.1   Representative quadruplets

In the DIA, the contributions to the nonlinear interactions for one or more representative quadruplets are evaluated for each discrete point in the spectral phase space in the numerical model. The discrete spectral components will be denoted here as $\boldsymbol{k}_d$. Note that this notation does not imply that the phase space is discretized by discretizing the components of $\boldsymbol{k}$ individually. In fact, wavenumber-direction (k, θ) and frequency-direction (f, θ) representations of phase space are universally used in practical wind wave models because of their isotropic directional discretization properties, which are not present in a conventionally discretized (k_x, k_y) representation of phase space. The representative quadruplets satisfy the general resonance conditions (1.9) and (1.10), as well as additional equations that constrain or define the layout of the representative quadruplet. In its most general form, the representative quadruplet is defined as (see Part 2)

Table 2.1: One two or three parameter definitions of the representative quadruplet from Part 2.

	$\boldsymbol{k}_d$	σ	$\Delta\theta$	a_1	a_2	a_3	a_4
(λ)	$\boldsymbol{k}_1$	σ_1	0	1	1	$1+\lambda$	$1-\lambda$
(λ,μ)	$\frac{1}{2}(\boldsymbol{k}_1+\boldsymbol{k}_2)$	$\frac{1}{2}(\sigma_1+\sigma_2)$		$1+\mu$	$1-\mu$	$1+\lambda$	$1-\lambda$
$(\lambda,\mu,\Delta\theta)$	Eq. (2.11)	σ_1	$\Delta\theta$	$1+\mu$	$1-\mu$	$1+\lambda$	$1-\lambda$

$$\left.\begin{array}{rcl} \sigma_1 & = & a_1\sigma \\ \sigma_2 & = & a_2\sigma \\ \sigma_3 & = & a_3\sigma \\ \sigma_4 & = & a_4\sigma \\ \theta_2 & = & \theta_1 \pm \Delta\theta \end{array}\right\} \quad , \tag{2.10}$$

where $a_1 + a_2 = a_3 + a_4$ to satisfy Eq. (1.10) and where the necessity to explicitly define $\Delta\theta$ depends on the actual definition of σ and a_1 through a_4, and on the relation between $\boldsymbol{k}_1$ through $\boldsymbol{k}_4$ and $\boldsymbol{k}_d$. Following Part 2, a distinction is made between a one, two and three parameter definition of the representative quadruplet. These definitions are presented in Table 2.1.

The one-parameter definition of the representative quadruplet was introduced by HHAB. With the assumption that $\boldsymbol{k}_1 = \boldsymbol{k}_2$ (which is equivalent to $a_1 = a_2$ and $\Delta\theta = 0$), two mirror image quadruplet layouts can be found (see Part 2). The complete source term is found by summation of individual contributions from Eq. (2.9) for the two realizations for $\boldsymbol{k}_1$ equal to each discrete $\boldsymbol{k}_d$[1].

The two-parameter definition of the representative quadruplet was introduced in Part 1. By assuming that $\boldsymbol{k}_d$ and σ satisfy the dispersion relation, $\Delta\theta$ is implicitly defined. For each $\boldsymbol{k}$ valid values of $\boldsymbol{k}_3$ and $\boldsymbol{k}_4$ are identical to those of the one-parameter quadruplet with identical λ. However, now $\boldsymbol{k}_1 \neq \boldsymbol{k}_2$. Contrary to the one-parameter layout, four quadruplets can be found for each parameter setting. To assure that this parameterization defaults to the original DIA, Part 1 therefore introduced a factor $1/2$ in the right side of Eq. (2.9) (taking half the contribution of pairs of two equal solutions).

The three-parameter definition was introduced in Part 2, and represents a symmetric version of the three-parameter definition introduced by Van Vledder (2001). The phase space is sampled by considering quadruplets for each discrete wavenumber

$$\boldsymbol{k}_d = \frac{||\boldsymbol{k}_1||}{||\boldsymbol{k}_1+\boldsymbol{k}_2||}\left(\boldsymbol{k}_1+\boldsymbol{k}_2\right) \quad , \tag{2.11}$$

---

[1] as well as for extensions to the discrete grid from where contributions occur inside the discrete phase domain.

which results in symmetric sets of four resulting quadruplets.

It should be noted that for a given quadruplet layout, spectral space can be sampled in many different ways. For instance, $\boldsymbol{k}_d = \boldsymbol{k}_i$ will give a valid sampling scheme for each i. However, as is illustrated in Part 2, all such sampling methods are essentially identical. Hence, the sampling scheme is chosen to maximize symmetry in the resulting quadruplet, which in turn minimizes mathematical operations required for the computation of the source term.

The procedure to evaluate the layout of quadruplets is as follows. Equation (2.10) and Table 2.1 with appropriate values for λ, μ and $\Delta\theta$ depending on the one-, two-, or three-parameter definition of the quadruplet automatically satisfy the resonance conditions for the corresponding frequencies σ_i. The frequency σ_i and the water depth d uniquely define the (scalar) wavenumbers k_i through the dispersion relation (1.6). The angles between the wavenumbers, and hence the wavenumber vectors $\boldsymbol{k}_i$ then follow from simple trigonometry. Equations for the quadruplets for deep water are presented in Appendix A of Part 2. For convenience, define

$$\boldsymbol{k}_c = \boldsymbol{k}_1 + \boldsymbol{k}_2 = \boldsymbol{k}_3 + \boldsymbol{k}_4 \quad , \quad k_c = ||\boldsymbol{k}_c|| \quad . \tag{2.12}$$

Note that $\boldsymbol{k}_c$ is always explicitly defined by the quadruplet, because $\boldsymbol{k}_1$ and $\boldsymbol{k}_2$ are always explicitly defined. Note also that $\boldsymbol{k}_c$ and $\boldsymbol{k}_d$ share the same direction to maximize the symmetry in the quadruplet. Defining the directions of the components of the quadruplet relative to the direction of $\boldsymbol{k}_d$ or $\boldsymbol{k}_c$ as θ_i, the angles θ_1 and θ_2 become

$$\theta_1 = \pm \arccos\left(\frac{k_1^2 + k_c^2 - k_2^2}{2\,k_c\,k_1}\right) \quad , \tag{2.13}$$

$$\theta_2 = \mp \arccos\left(\frac{k_2^2 + k_c^2 - k_1^2}{2\,k_c\,k_2}\right) \quad , \tag{2.14}$$

where the positive value of θ_1 corresponds to the negative value of θ_2 and vise versa. Similarly, the angles θ_3 and θ_4 become

$$\theta_3 = \pm \arccos\left(\frac{k_3^2 + k_c^2 - k_4^2}{2\,k_c\,k_3}\right) \quad , \tag{2.15}$$

$$\theta_4 = \mp \arccos\left(\frac{k_4^2 + k_c^2 - k_3^2}{2\,k_c\,k_4}\right) \quad . \tag{2.16}$$

With these equations, there are two solutions for $\boldsymbol{k}_1$ and $\boldsymbol{k}_2$, similarly there are two solutions for $\boldsymbol{k}_3$ and $\boldsymbol{k}_4$, resulting in a total of four different quadruplets.

For practical applications, it is important to establish the range of valid values for the parameters defining the quadruplet. Generally, frequencies need to be positive. The symmetry of the interactions furthermore show that the interaction

9

are insensitive to sign changes in any of the three parameters. Thus, generally, the three parameter can be limited as

$$
\left.
\begin{array}{ccccc}
0 & \leq & \lambda & \leq & 1 \\
0 & \leq & \mu & \leq & 1 \\
0 & \leq & \Delta\theta & \leq & 180°
\end{array}
\right\} \quad ,
\tag{2.17}
$$

Moreover, it is required that the length of k_3 and k_4 combined is as least the length of k_c, and that the difference in lengths is no greater than k_c

$$
k_3 + k_4 \geq k_c \quad ,
\tag{2.18}
$$

$$
k_3 - k_4 \leq k_c \quad .
\tag{2.19}
$$

As $\boldsymbol{k}_c$ is generally defined by μ and $\Delta\theta$, this potentially provides additional limitations on valid values for λ.

In Part 2, Eqs. (2.13) through (2.16) are presented in terms of nondimensional wavenumbers $\tilde{k}_i$, this being convenient in assessing valid solutions according to Eqs. (2.18) and (2.19). Assuming deep water, a natural definition of a nondimensional wavenumber is in terms of the frequency σ and the acceleration of gravity g. Expanding the definition of Part 2 to arbitrary water depths,

$$
\tilde{k}_i = \frac{gk_i}{\sigma^2} = \frac{\sigma_i^2}{\sigma^2 \tanh k_i d} = \frac{a_i^2}{\tanh k_i d} \quad .
\tag{2.20}
$$

For the general three-parameter quadruplet layout, $\tilde{k}_c$ can be written as

$$
\tilde{k}_c^2 = \tilde{k}_1^2 + 2\tilde{k}_1\tilde{k}_2 \cos\Delta\theta + \tilde{k}_2^2 \quad ,
\tag{2.21}
$$

or

$$
\tilde{k}_c = \left[\left(\frac{(1+\mu)^2}{\tanh k_1 d} \right)^2 + \frac{2(1-\mu^2)^2 \cos\Delta\theta}{\tanh k_1 d \ \tanh k_2 d} + \left(\frac{(1-\mu)^2}{\tanh k_2 d} \right)^2 \right]^{\frac{1}{2}} \quad .
\tag{2.22}
$$

For the one- and two-parameter quadruplet these equations reduce to

$$
\tilde{k}_c = 2\tilde{k}_d = \frac{2}{\tanh k_d d} \quad ,
\tag{2.23}
$$

Multiplying Eqs. (2.18) and (2.19) with $g\sigma^{-2}$ results in similar equations in terms of $\tilde{k}_i$, which can be written as

$$
\frac{(1+\lambda)^2}{\tanh k_3 d} + \frac{(1-\lambda)^2}{\tanh k_4 d} \geq \tilde{k}_c \quad ,
\tag{2.24}
$$

$$
\frac{(1+\lambda)^2}{\tanh k_3 d} - \frac{(1-\lambda)^2}{\tanh k_4 d} \leq \tilde{k}_c \quad ,
\tag{2.25}
$$

For deep water, all hyperbolic tangents in the above equations become 1, and solving the above equations reproduces the explicit limits for λ from Part 2

$$\sqrt{\max\left(0., \frac{1}{2}\tilde{k}_c - 1\right)} \leq \lambda \leq \frac{1}{4}\tilde{k}_c \quad . \tag{2.26}$$

For the one- and two-parameter quadruplet definition, $\tilde{k}_c = 2$, and this equation reduces even further to

$$0 \leq \lambda \leq \frac{1}{2} \quad , \tag{2.27}$$

which is more restrictive than the general limitations on λ presented in Eq. (2.17).

For restricted water depths, solutions to Eqs. (2.24) and (2.25) are not trivial, because k_3 and k_4 are implicit functions of λ. The corresponding limiting values of λ will be assessed numerically below. First, however, analytical solutions will be considered for extremely shallow water.

The nondimensional wavenumber $\tilde{k}_i$ is not convenient for extremely shallow water as $\tilde{k}_i \rightarrow \infty$ for $k_i d \rightarrow 0$. In this case, it is more convenient to define a nondimensional wavenumber in terms of d, as well as σ and g. Furthermore considering that in sufficiently shallow water $\tanh kd \rightarrow kd$, a suitable nondimensional wavenumber can be defined as

$$\hat{k}_i = \frac{k_i\sqrt{gd}}{\sigma} = a_i \quad . \tag{2.28}$$

Substitution in Eq. (2.18) results in

$$2 \leq \hat{k}_c \quad . \tag{2.29}$$

Because λ has disappeared from this equation, this equation now in fact may limit μ and $\Delta\theta$. Considering that generally

$$\hat{k}_c^2 = \hat{k}_1^2 + 2\hat{k}_1\hat{k}_2 \cos \Delta\theta + \hat{k}_2^2 \quad , \tag{2.30}$$

$\hat{k}_c$ can in general be expressed in terms of μ and $\Delta\theta$ as

$$\hat{k}_c^2 = 2\left\{1 + \mu^2 + (1 - \mu^2)\cos \Delta\theta\right\} \tag{2.31}$$

Substitution in Eq. (2.29) yields

$$4 \leq 2\left\{1 + \mu^2 + (1 - \mu^2)\cos \Delta\theta\right\} \quad , \tag{2.32}$$

which in turn reduces to

$$1 \leq \cos \Delta\theta \quad , \tag{2.33}$$

11

Equation (2.18), therefore, does not provide additional constraints for λ, μ or $\Delta\theta$ in the shallow water limit. Substitution of $\hat{k}_i$ in Equation (2.19) results in

$$\lambda \leq \frac{1}{2}\hat{k}_c \qquad (2.34)$$

For the one- and two-parameter quadruplet definition, $\hat{k}_c = 2$, and λ thus is limited to

$$0 \leq \lambda \leq 1 \quad . \qquad (2.35)$$

A comparison of Eqs (2.27) and (2.35) shows that extremely shallow water is less restrictive with respect to valid quadruplet parameters than deep water.

Having established the valid range of the quadruplets in limiting cases, the quadruplet evolution as a function of general depths will be assessed numerically, starting with the one-parameter quadruplet. For this quadruplet, Eqs. (2.24) and (2.25) become

$$\frac{(1+\lambda)^2}{\tanh k_3 d} + \frac{(1-\lambda)^2}{\tanh k_4 d} \geq \frac{2}{\tanh k_1 d} \quad , \qquad (2.36)$$

$$\frac{(1+\lambda)^2}{\tanh k_3 d} - \frac{(1-\lambda)^2}{\tanh k_4 d} \leq \frac{2}{\tanh k_1 d} \quad . \qquad (2.37)$$

The first equation represents the lower valid limit of λ. Substituting $\lambda = 0$ (which implies $k_1 = k_3 = k_4$) results in $2 \geq 2$, identifying $\lambda = 0$ as the lower limit irrespective of the water depth. The second equation represents the upper limit of λ. Because λ uniquely defines k_3 and k_4, a simple root finding algorithm is sufficient to solve for the maximum valid λ.

Apart from the limiting value of λ the evolution of the shape of the quadruplet with depth is interesting. This shape is defined by the ratios k_3/k_1 and k_4/k_1, and by the internal angles θ_3 and θ_4. Using the dispersion relation (1.6) and the definition of k_3, the wavenumber ratios can be expressed as

$$\frac{k_3}{k_1} = (1+\lambda)^2 \frac{\tanh k_1 d}{\tanh k_3 d} \quad , \qquad (2.38)$$

$$\frac{k_4}{k_1} = (1-\lambda)^2 \frac{\tanh k_1 d}{\tanh k_4 d} \quad . \qquad (2.39)$$

It is easily verified that these ratios are monotonic functions of the relative depth. The ratios of wavenumbers as a function of $k_1 d$ are presented in Figs 2.1 for several values of λ. Indeed, both ratios systematically move closer to 1 for decreasing water depths. For $\lambda = 0.5$ (thick solid lines) or smaller, valid quadruplets can be found irrespective of the relative depth. For restricted water depths, valid quadruplets can be found for larger λ. From the dashed lines in Fig. 2.1 it can
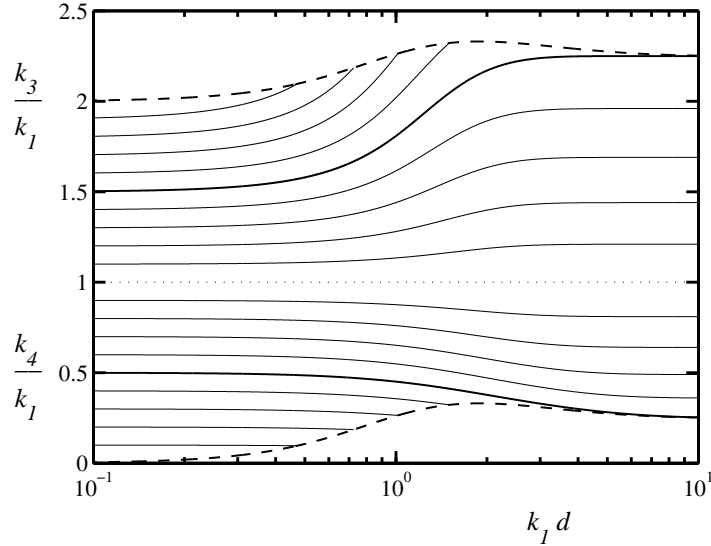
Fig. 2.1 : The wavenumber ratios k_3/k_1 (> 1) and k_4/k_1 (< 1) as a function of the relative water depth k_1d for the one-parameter definition of the quadruplet and for λ increasing from 0 to 1 in increments of 0.1. Dotted line: $\lambda = 0$. Thick lines: $\lambda = 0.5$. Dashed lines: the boundary of the area with valid solutions.

be observed that the maximum allowable value of λ monotonically increases with decreasing depth. This implies that every quadruplet layout that is valid in deep water has a valid solution in shallow water, but that for valid quadruplet layouts in shallow water with $\lambda > 0.5$ no valid deep water quadruplet layout exists.

Figure 2.2 presents the corresponding internal quadruplet angles θ_3 and θ_4. Note that the boundaries of the areas with valid solutions in this parameter space are given by $\theta_4 = 180°$, and $\theta_3 = 0°$. θ_4 systematically decreases with decreasing depth for a given values of λ. The behavior of θ_3 with decreasing depth is more complicated. Initially, θ_3 increases, but after reaching its maximum (absolute) values, it decreases monotonically.

A design feature of the two-parameter quadruplet is that it leaves the behavior of $\boldsymbol{k}_3$ and $\boldsymbol{k}_4$ with respect to λ and d unchanged compared to the one-parameter quadruplet definition. Moreover, the behavior of $\boldsymbol{k}_1$ and $\boldsymbol{k}_2$ with respect to μ and d can be obtained from the former by proper exchange of parameters. This implies that the above analysis for the one-parameter quadruplet definition can be applied directly to the two-parameter quadruplet. However, due to the symmetry of the definition, exchanging λ and μ results in an identical interaction. Hence, it is sufficient to consider
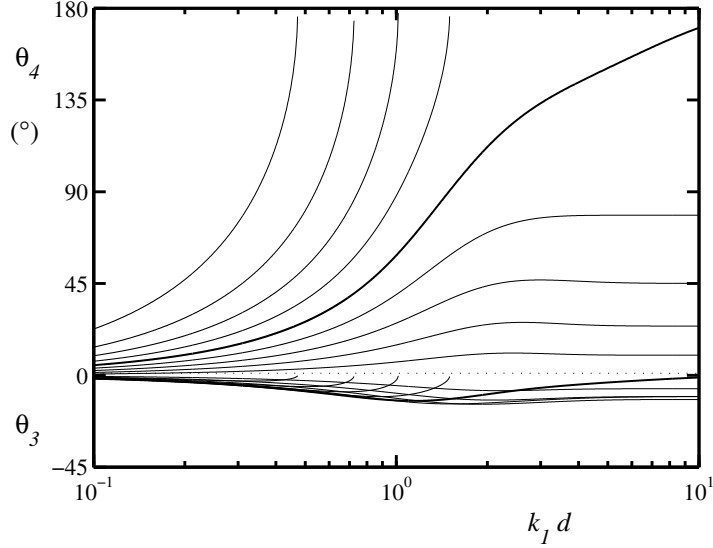
Fig. 2.2 : Like Fig. 2.1 for internal angles θ_3 and θ_4.

$$0 \leq \mu \leq \lambda \leq \lambda_{\max} \quad . \tag{2.40}$$

For the three-parameter quadruplet, a separate analysis is required. Most important is the range of valid parameter values as a function of the depth. This range can again be established from Eqs. (2.24) and (2.25), substituting the general expression for $\tilde{k}_c$ from Eq. (2.22). $\tilde{k}_c$ is a function of μ and $\Delta\theta$ only. For the general range of valid values for the latter two parameters as given in (2.17). Note that λ and μ are no longer exchangeable, as $\tilde{k}_c$ is a function of μ, but not of λ. If however, $\Delta\theta$ is adjusted to reflect θ_3 and θ_4 from the original quadruplet, an identical quadruplet can be obtained by exchanging λ and μ and by taking

$$\Delta\theta = |\theta_3 - \theta_4| \quad , \tag{2.41}$$

where θ_3 and θ_4 are taken from the original values of λ and μ.

Figure 2.3 presents the minimum and maximum valid λ as a function of μ and $\Delta\theta$ for deep water. Several observations can be made from this figure. First, for a given $\Delta\theta$, $\tilde{k}_c$ of Eq. (2.21) or (2.22) increases monotonically with μ. This implies that both $\lambda_{\min}$ and $\lambda_{\max}$ increase monotonically with μ for a given $\Delta\theta$. Similarly, $\tilde{k}_c$ decreases monotonically with increasing $\Delta\theta$ for a given μ, resulting in a corresponding behavior of $\lambda_{\min}$ and $\lambda_{\max}$. Furthermore, special conditions occur for $\Delta\theta \to 180°$ and $\mu \to 0$, for which both $\lambda_{\min}$ and $\lambda_{\max}$ approach 0. Also, for $\mu \to 1$, $\lambda_{\min}$ and $\lambda_{\max}$ both approach 1. In both cases, the range of valid

14
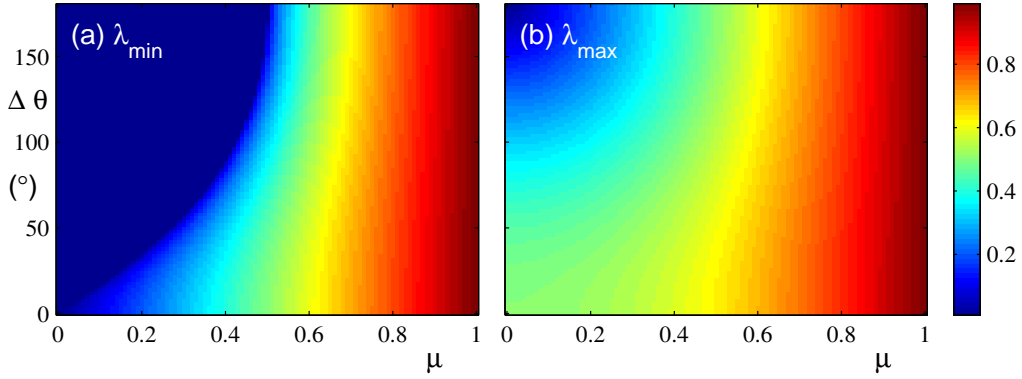
Fig. 2.3 : Minimum valid λ (panel a) and maximum valid λ as a function of μ and $\Delta\theta$ for the three parameter quadruplet layout for deep water $kd = 10$.
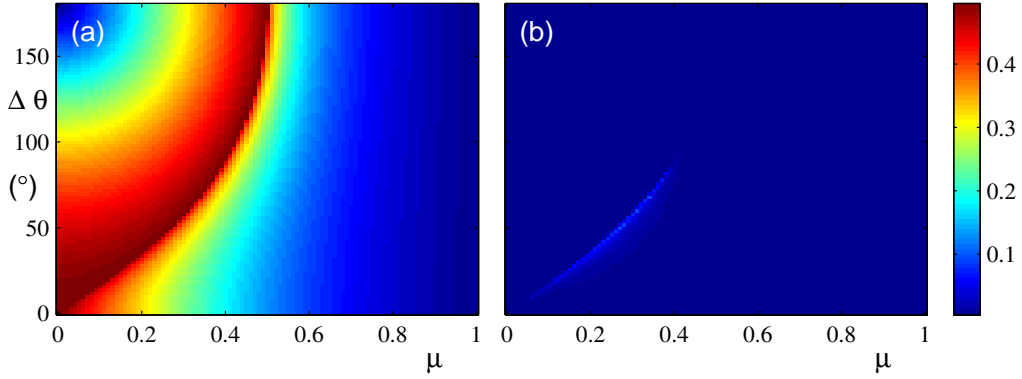
Fig. 2.4 : Range of valid values of λ corresponding to Fig. 2.3 (panel a) and maximum $\lambda_{\max}$ for all water depths minus its deep water value (panel b).

values of λ collapses to a single value. The maximum range of valid values for λ in deep water is 0.5, as is illustrate in Fig. 2.4a.

If the water depth is reduced, $\lambda_{\min}$ generally decreases, whereas $\lambda_{\max}$ generally increases. This is illustrated in Figs. 2.5 and 2.6 for relative water depths $kd = 1$ and $kd = 0.1$, respectively. It can be shown numerically that $\lambda_{\max}$ increases systematically with decreasing kd for al μ and $\Delta\theta$ (figures not presented here). However, the decrease of $\lambda_{\min}$ with decreasing kd is not monotonic, as is illustrated in Fig. 2.4b. This figure presents the maximum values of $\lambda_{\min}$ for all relative depths, minus its value for deep water. Hence, a value of 0 indicates that the deep water value of $\lambda_{\min}$ indeed is the most restrictive for all water depths, but values larger than 0 indicate that the most restrictive conditions occur for restricted water depths. Figure 2.4b indicates that there is a restricted area in $(\mu, \Delta\theta)$ space where $\lambda_{\min}$ increases by up to 0.1 from its deep water value. However, if λ

15
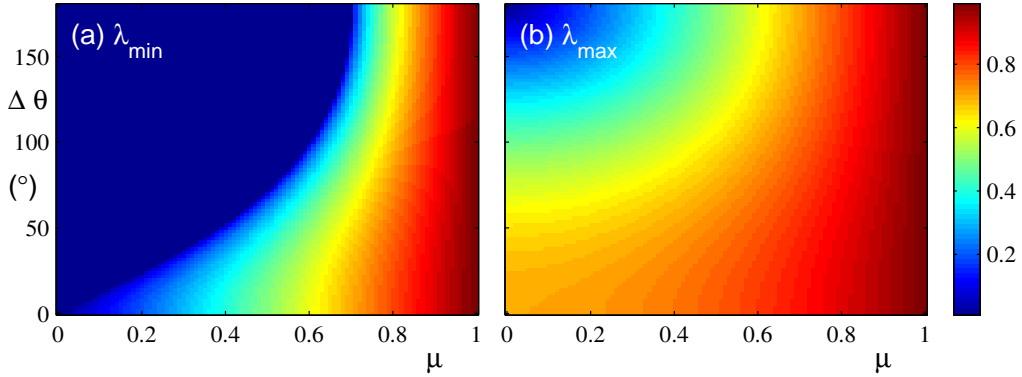
Fig. 2.5 : Like Fig. 2.3 for $kd = 1.0$.
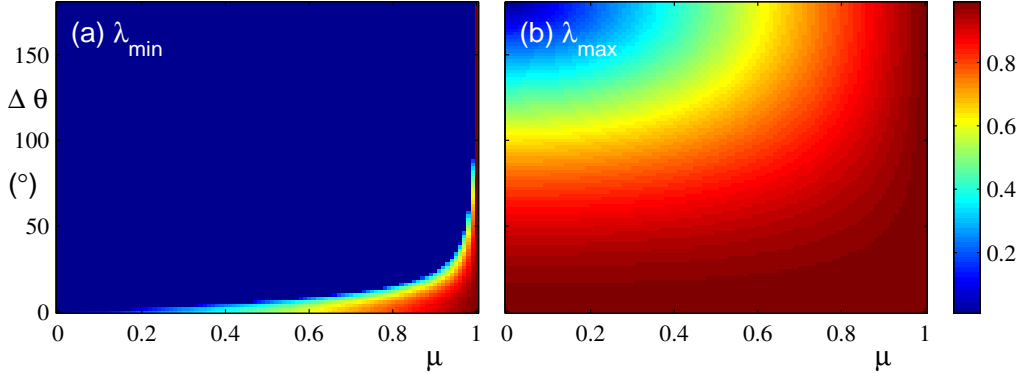
Fig. 2.6 : Like Fig. 2.3 for $kd = 0.1$.

and μ are ordered according to Eq. (2.40), if necessary using the transformation described in conjunction with (2.41), λ is always larger than λ_{min} as, by definition, $\lambda_{min} < \mu$. For such a quadruplet definition, valid layouts for deep water always result in valid layouts for restricted water depth (figures not presented here).

Without going into detail in the behavior of the quadruplet layout as a function of diminishing depth, it should be noted that the two- and three-parameter quadruplet are expected to behave systematically different, as θ_1 and θ_2 develop differently as a function of depth for the two- or three-parameter definition. In the former case, these angles change as a function of μ and kd identical to the changes of θ_3 and θ_4 as a function of λ and kd as presented in Fig. 2.2. For the three-parameter definition, however, simple trigonometry requires that

$$|\theta_1 - \theta_2| = \Delta\theta \quad . \tag{2.42}$$

This implies that for the three-parameter quadruplet definition internal angles in the quadruplet remain large even for small kd, whereas such angles are systemically reduced in the two-parameter definition. This may have a significant

16

impact on shallow water behavior of both quadruplet definitions, as will be discussed later.

2.2 Discretization of phase space

Some complications occur in the DIA because the phase space is discretized. In general, it will be impossible to completely align quadruplets with the discrete grid. This has two consequences for the DIA. First, the action densities n_i needed to evaluate the product term P_{1234} in Eq. (2.9) are estimated by bi-linear interpolation from the four surrounding action densities at discrete points in phase space.

$$n_i = \sum_{j=1}^{4} w_{i,j} n_j \quad , \tag{2.43}$$

where the counter j identifies the four surrounding discrete points in phase space, and where $w_{i,j}$ are the corresponding weight factors. Because these interpolations are performed only to compute the strength of the interactions in Eq. (2.9), they have no impact on the conservation properties of the interactions. Second, the contribution $\delta S_{nl,i}$ do not coincide with the discrete grid in phase space. These contributions are similarly distributed over the surrounding grid points as

$$\delta S_{nl,i,j} = w_{i,j} \delta S_{nl,i} \quad . \tag{2.44}$$

This redistribution of the contributions over the discrete phase-space grid potentially has an impact on the conservation characteristics of the DIA. Such characteristics are most elegantly addressed by considering the conservation characteristics of a single redistribution of quantities for a single quadruplet. Note that in practice, some quadruplets will straddle the outer limits of a discrete phase space grid. Because contributions of such quadruplets are partially unresolved by the discrete model grid, total interactions for a finite discrete phase space grid are generally not conserved, even if individual contributions for each quadruplet are conserved. Addressing the conservation characteristics of a single quadruplet therefore is more elegant and more relevant than addressing the conservation of quantities in a finite phase space.

For simplicity we will consider the traditional one parameter quadruplet defined in terms of λ only. Furthermore, consider the traditional DIA in terms of the energy spectrum $F(f, \theta)$, and the corresponding source term $s_{nl}(f, \theta)$. Dropping common terms for all four contributions, the source term contributions are proportional to [cf. Eq. (2.5) of Part 2].
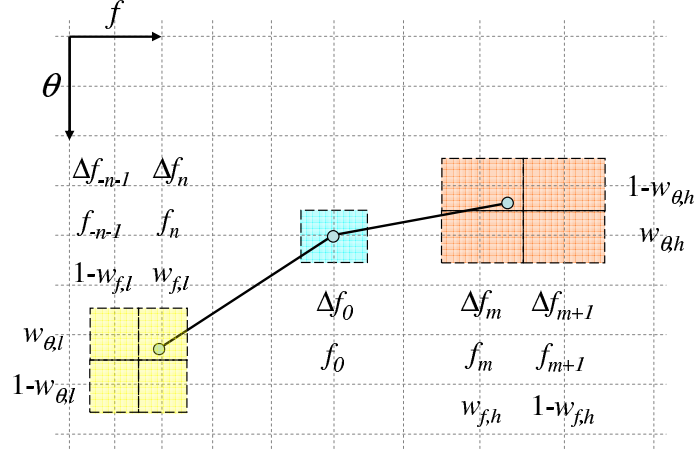
Fig. 2.7 : Schematic layout of redistribution of contributions for a traditional
DIA quadruplet with $\lambda = 0.25$ and a grid with $X = 1.1$ and $\Delta\theta = 15°$.
Dashed lines represent grid lines in phase space. Boxes represent 'bins'
in phase space.

$$\begin{pmatrix} \delta s_{nl,1} \\ \delta s_{nl,2} \\ \delta s_{nl,3} \\ \delta s_{nl,4} \end{pmatrix} \propto \begin{pmatrix} -1 \\ -1 \\ 1 \\ 1 \end{pmatrix} \quad , \tag{2.45}$$

For the traditional quadruplet with $\lambda = 0.25$ in a traditional phase space dis-
cretization where $\Delta\theta = 15°$ and $X = 1.1$ in Eq. (1.8) the impacted spectral bins
are graphically depicted in Fig. 2.7. First, the conservation of energy will be
considered. The central (blue) bin receives the contributions of $\boldsymbol{k}_1$ and $\boldsymbol{k}_2$, and
the energy change according to Eq. (2.45) is proportional to

$$-2\Delta f_0 \Delta\theta \tag{2.46}$$

For $\boldsymbol{k}_3$ (the yellow bins), energy is contributed to four bins. Considering weight
factors $w_{\theta,l}$ and $w_{f,l}$ in θ and f-space, respectively, and offsets in frequency space
relative to the central bin of n and $n-1$, respectively, and considering that $\Delta f_m = X^m \Delta f_0$ and that $\Delta\theta$ is uniform throughout the grid, the four contributions can
be written as

$$X^{-n} \left[w_{f,l} + (1 - w_{f,l})X^{-1} \right] \Delta f_0 \Delta\theta \quad . \tag{2.47}$$

Substituting the frequency weight factor

$$w_{f,l} = \frac{(1 - \lambda) - X^{-n-1}}{X^{-n} - X^{-n-1}} \quad , \tag{2.48}$$

18

shows that the total change in energy at $\boldsymbol{k}_3$ in (2.45) is proportional to

$$(1 - \lambda)\Delta f_0 \Delta \theta \quad . \tag{2.49}$$

Similarly, the change of energy in terms of weights, the weight function and the resulting total change of energy at $\boldsymbol{k}_4$ (orange bins) become

$$X^m \left[w_{f,h} + (1 - w_{f,h})X \right] \Delta f_0 \Delta \theta \quad , \tag{2.50}$$

$$w_{f,h} = \frac{X^{m+1} - (1 + \lambda)}{X^{m+1} - X^m} \quad , \tag{2.51}$$

$$(1 + \lambda)\Delta f_0 \Delta \theta \quad . \tag{2.52}$$

Adding the contributions from $\boldsymbol{k}_1$ through $\boldsymbol{k}_4$ shows that the total change of energy is proportional to

$$\left[(1 - \lambda) + (1 + \lambda) - 2 \right] \Delta f_0 \Delta \theta = 0 \quad . \tag{2.53}$$

Hence, the total energy is conserved with the distribution of changes of energy to discrete grids points in Eq. (2.44).

The source term for action density $S_{nl}(f, \theta)$ corresponding to Eq. (2.45) can be written as

$$\begin{pmatrix} \delta S_{nl,1} \\ \delta S_{nl,2} \\ \delta S_{nl,3} \\ \delta S_{nl,4} \end{pmatrix} \propto \begin{pmatrix} -\sigma_1^{-1} \\ -\sigma_2^{-1} \\ \sigma_3^{-1} \\ \sigma_4^{-1} \end{pmatrix} \quad . \tag{2.54}$$

For the traditional DIA quadruplet of Fig. 2.7, the contribution for the wavenumbers $\boldsymbol{k}_1$ and $\boldsymbol{k}_2$ to the total change of action is proportional to ($\sigma_1 = \sigma_2 = \sigma$)

$$-2\sigma^{-1}\Delta f_0 \Delta \theta \tag{2.55}$$

The corresponding contributions at wavenumber $\boldsymbol{k}_3$ become proportional to

$$X^{-n} \left[w_{f,l} + (1 - w_{f,l})X^{-1} \right] \sigma_3^{-1}\Delta f_0 \Delta \theta \quad . \tag{2.56}$$

Considering the corresponding contributions to the energy change, this expression can be written as

$$(1 - \lambda)\,\sigma_3^{-1}\Delta f_0 \Delta \theta = \sigma^{-1}\Delta f_0 \Delta \theta \quad . \tag{2.57}$$

Similarly, it can be shown that the contribution at wavenumber $\boldsymbol{k}_4$ becomes

$$(1 + \lambda)\,\sigma_4^{-1}\Delta f_0 \Delta \theta = \sigma^{-1}\Delta f_0 \Delta \theta \quad . \tag{2.58}$$

Hence, the total wave action is conserved as

$$(-2 + 1 + 1)\, \sigma^{-1} \Delta f_0 \Delta \theta = 0 \quad . \tag{2.59}$$

Finally, contributions to the source term for wave momentum $\delta M(f, \theta)$, similar to Eq. (2.54) can be written as

$$\begin{pmatrix} \delta M_{nl,1} \\ \delta M_{nl,2} \\ \delta M_{nl,3} \\ \delta M_{nl,4} \end{pmatrix} \propto \begin{pmatrix} -\boldsymbol{k}_1 \sigma_1^{-1} \\ -\boldsymbol{k}_2 \sigma_2^{-1} \\ \boldsymbol{k}_3 \sigma_3^{-1} \\ \boldsymbol{k}_4 \sigma_4^{-1} \end{pmatrix} \quad . \tag{2.60}$$

Using the above results for change of action, it is easily shown that the change of momentum is proportional to

$$(-\boldsymbol{k}_1 - \boldsymbol{k}_2 + \boldsymbol{k}_3 + \boldsymbol{k}_4)\, \sigma^{-1} \Delta f_0 \Delta \theta \quad . \tag{2.61}$$

Using the resonance condition (1.10), the momentum is therefore also conserved. Hence, the distribution of contributions to the interactions over discrete points in phase space according to Eq. (2.44) results in proper conservation of energy action and momentum for the conventional quadruplet of the DIA. Expansion for arbitrary quadruplets is trivial, and will not be presented here.

The above analysis of the conservation properties of the DIA can be extended to the conventional shallow water version of the DIA, where the DIA is simply rescaled by a constant factor, which is a function of the mean relative depth $\overline{kd}$. The layout of the quadruplet is still evaluated assuming deep water. Inspection of the above considerations for conservation of energy and action show that both quantities are still conserved in shallow water, even if the resonance conditions are evaluated for deep water. If, however, deep water dispersion is used in shallow water to evaluate the quadruplet, the wave number resonance condition (1.10) is violated. Thus, Eq. (2.61) no longer is zero, and wave momentum no longer is conserved. Therefore, it is important to evaluate resonance for the actual water depth, in order to guarantee conservation of all three wave quantities (action, energy and momentum).

2.3 Multiple representative quadruplets

With the above, the basic method to evaluate a DIA for a given discrete spectrum is outlined. For each individual quadruplet and each discrete spectral components with which the quadruplet is aligned, up to 16 contributions $\delta S_{nl,i,j}$ are computed according to Eq. (2.44). For each discrete spectral point several quadruplets are found for a single quadruplet layout; 2 for the conventional one-parameter definition, 4 for the two- and three-parameter quadruplet definition. Introducing l as the counter of discrete spectral points for which quadruplets are evaluated,

and m as the number of valid quadruplet realizations s for a single representative quadruplet definition $(\lambda, \mu, \Delta\theta)$, the total source term becomes

$$S_{nl} = \sum_{\forall i,j,l,m} \delta S_{nl,i,j,l,m} \quad , \tag{2.62}$$

ignoring contributions outside the discrete spectral domain.

This definition is easily expanded to include multiple representative quadruplet definitions $(\lambda, \mu, \Delta\theta)$, as this simply adds quadruplet realizations m. Considering that here are M_1 quadruplets satisfying a single definition $(\lambda, \mu, \Delta\theta)$, and that there are M_2 such definitions, $m \in [1, M_1]$ for a traditional DIA with a single representative quadruplet definition, and $m \in [1, M_1 M_2]$ for a DIA with multiple quadruplet definitions. The latter is generally designated as a Multiple DIA (MDIA).

It is considered desirable that an MDIA with multiple but identical quadruplet definitions reduces to the corresponding (single) DIA. This requires the DIA to be scaled with M_2^{-1}. Furthermore, generally $M_1 = 4$, with two sets of identical quadruplets for the one-parameter quadruplet layout. To assure that the general MDIA reduces to the original DIA, a second scaling factor $2M_1^{-1} = 1/2$ is needed. Thus, the general MDIA that properly reduces to the original DIA for $M_2 = 1$ with $\mu = 0$ and $\Delta\theta = 0$ is defined as

$$S_{nl} = \frac{1}{2M_2} \sum_{\forall i,j,l,m} \delta S_{nl,i,j,l,m} \quad . \tag{2.63}$$

2.4 Spectral description

Traditionally, interactions and nonlinear properties of wind waves are investigated by considering the spectrum in terms of both the wavenumber vector and the frequency $(\boldsymbol{k}, \sigma)$. The spectral description, and the underlying Fourier transform of the surface, is inherently linear. Using the linear dispersion relation (1.6), the three-dimension spectral space becomes two-dimensional. In theoretical work, the two-dimensional phase space traditionally is described by the wavenumber vector $(\boldsymbol{k})$, for instance as above with the wavenumber action density spectrum $n(\boldsymbol{k})$. For numerical models, however, the description of the spectral or phase space with $\boldsymbol{k}$ is not convenient, because discretization of $\boldsymbol{k}$ introduces a directional anisotropy in the discretized space. Directional isotropy can be achieved by describing the phase space with wavenumber and direction (k, θ) or frequency and direction $(f, \theta$ or $\sigma, \theta)$. The wavenumber description is theoretically preferred, due to its invariance characteristics with respect to depth changes, but has a numerical disadvantage of loss of resolution in shallow water (e.g., Tolman and Booij, 1998). In the WAVEWATCH III model, this disadvantage is mitigated

by solving equations for the wavenumber-directing (k, θ) spectrum on a spatially invariant frequency (σ) grid (Tolman and Booij, 1998).

Furthermore, a choice needs to be made between action or energy descriptions of the wave field. The former are preferable in models, due to the conservation characteristics for arbitrary (slowly) varying media (e.g., Bretherthon and Garrett, 1968), whereas the latter are conventionally used, as they are more naturally observed. Note that in this context, the so-called energy spectrum as obtained by a Fourier transform of observations of surface elevations most often in fact is a variance spectrum. The true energy spectrum is obtained by multiplying this variance spectrum with ρg. Defining $N(\iota)$ as an action density spectrum with an arbitrary description of the phase space ι, and $F(\iota)$ as the corresponding energy (variance) density spectrum, the relation between the two is given as

$$F(\iota) = \sigma \, N(\iota) \ . \tag{2.64}$$

Changing the phase space description ι is governed by the corresponding Jacobian transformations. The conversion of the vector wavenumber spectrum $F(\boldsymbol{k})$ to the wavenumber-direction spectrum $F(k, \theta)$ can be done in two fundamentally different ways. Adopting a polar perspective on (k, θ) space, the surface of an infinitesimal phase space element becomes $\delta k \times k \delta \theta$. and the total wave energy becomes

$$E = \int k \, F(k, \theta) \, dk d\theta \ . \tag{2.65}$$

Because this represents a simple rotation of the phase space element $\delta k_x \times \delta k_y$, the corresponding Jacobian transformation becomes[2]

$$F(k, \theta) = F(\boldsymbol{k}) \ . \tag{2.66}$$

Alternatively, a Cartesian perspective can be adopted where the surface of a phase space element becomes $\delta k \times \delta \theta$. and the total wave energy becomes

$$E = \int F(k, \theta) \, dk d\theta \ , \tag{2.67}$$

with a corresponding Jacobian transformation

$$F(k, \theta) = k \, F(\boldsymbol{k}) \ . \tag{2.68}$$

Both definitions are equally valid. The polar definition of the (k, θ) is generally preferred by mathematicians, whereas the Cartesian definition is universally used in practical wave models (e.g., HHAB). The preference for the latter in practical wave modeling appears to have its roots in history. The first wave spectra were based on points observation, from which the one-dimensional frequency

---

[2] With θ in radians. Conversion to degrees requires another Jacobian transformation.

spectrum $F_1(f)$ can be obtained by Fourier transform. From this spectrum the one-dimensional wavenumber spectrum can be obtained by transformation as $F_1(k) = \frac{c_g}{2\pi} F_1(f)$. From the latter spectrum a two-dimensional spectrum can be obtained in a simple way by using a normalized directional distribution $D(\theta)$ as $F(k, \theta) = F_1(k)D(\theta)$. This spectrum is compatible with the Cartesian definition, for which

$$F_1(k) = \int F(k, \theta) \, d\theta \quad . \tag{2.69}$$

However, the polar definition of the spectrum is not similarly compatible since

$$F_1(k) = k^{-1} \int F(k, \theta) \, d\theta \quad . \tag{2.70}$$

The Cartesian definition and the corresponding Eq. (2.68) will be used here. The conversions between phase space descriptions including the wave direction θ are unambiguous. For the energy spectrum F they are defined as

$$F(\sigma, \theta) = \frac{\partial k}{\partial \sigma} F(k, \theta) = c_g^{-1} F(k, \theta) \quad , \tag{2.71}$$

$$F(f, \theta) = \frac{\partial \sigma}{\partial f} F(\sigma, \theta) = 2\pi \, F(\sigma, \theta) \quad . \tag{2.72}$$

The basic DIA formulation of Eq. (2.9) can be converted to arbitrary spectra and phase space definitions using the definition (2.64) and the transformations (2.68), (2.71) and (2.72). In the following sections, the main attention will be on the scaling of the interactions with depth. Because this is assessed by addressing the impact for the conventional $F(f, \theta)$ spectrum, the corresponding DIA formulations for arbitrary and deep water will be considered in the present section. The WAVEWATCH III model, however, is based on the action spectrum $N(k, \theta)$. The optimum expressions used in this model are guided by numerical economy, and will be discussed in Section 4.

The adaptation to the DIA for the spectrum $F(f, \theta)$ are governed by the conversions

$$n(\boldsymbol{k}) = \frac{c_g \, F(f, \theta)}{2\pi \, k\sigma} \quad , \tag{2.73}$$

$$n(\boldsymbol{k}) = \frac{g^2 \, F(f, \theta)}{2 \, (2\pi)^5 \, f^4} \quad , \tag{2.74}$$

which are valid for arbitrary depth and deep water, respectively. Defining $F_i = F(f_i, \theta_i)$, and using the definition of the quadruplet, the product terms (2.4) for arbitrary and deep water, respectively, become

23

$$P_{1234} = B_3 \left[\frac{c_{g,1}F_1}{k_1\sigma_1} \frac{c_{g,2}F_2}{k_2\sigma_2} \left(\frac{c_{g,3}F_3}{k_3\sigma_3} + \frac{c_{g,4}F_4}{k_4\sigma_4} \right) - \right.$$
$$\left. \frac{c_{g,3}F_3}{k_3\sigma_3} \frac{c_{g,4}F_4}{k_4\sigma_4} \left(\frac{c_{g,1}F_1}{k_1\sigma_1} + \frac{c_{g,2}F_2}{k_2\sigma_2} \right) \right] \quad , \quad B_3 = \frac{1}{(2\pi)^3} \quad . \quad (2.75)$$

$$P_{1234} = B_3 \left[\frac{F_1}{a_1^4} \frac{F_2}{a_2^4} \left(\frac{F_3}{a_3^4} + \frac{F_4}{a_4^4} \right) - \frac{F_3}{a_3^4} \frac{F_4}{a_4^4} \left(\frac{F_1}{a_1^4} + \frac{F_2}{a_2^4} \right) \right] \quad ,$$
$$B_3 = \frac{g^6}{2^3 (2\pi)^{15} f^{12}} \quad , \tag{2.76}$$

where a_i and $f = \sigma/2\pi$ are defining the quadruplet as in Eq. (2.10). The factor B_3 is of a form similar to the scaling functions B, and will be combined with them in the final expression for the DIA. The other part of Eq. (2.9) that is affected by the transformation are the vectors left and right of the equal sign, which can be written in a more compressed form as

$$\delta S_{nl,i} = \mp \frac{\Delta \boldsymbol{k}}{\Delta \boldsymbol{k}_i} \times \dots \quad , \tag{2.77}$$

where ... represents the common terms independent of the quadruplet component i. For later reference, it is advantageous to first consider the effect of arbitrary conversions on these terms. Consider the conversion of the description of the phase space with the wavenumber vector $\boldsymbol{k}$ to arbitrary coordinates ι, governed by the Jacobian J. The grid elements are then related as

$$\Delta \boldsymbol{k} = J \Delta \iota \quad , \tag{2.78}$$

and the corresponding conversion from action spectrum $n(\boldsymbol{k})$ to energy spectrum $F(\iota)$ becomes

$$n(\boldsymbol{k}) = (\sigma J)^{-1} F(\iota) \quad . \tag{2.79}$$

Using an identical transformation between the source terms $S_{nl}(\boldsymbol{k})$ and $s_{nl}(\iota)$, and using Eq. (2.10), the equation considered becomes

$$(\sigma J)_i^{-1} \delta s_{nl,i} = \mp \frac{J \Delta \iota}{J_i \Delta \iota_i} \times \dots \quad , \tag{2.80}$$

or

$$\delta s_{nl,i} = \mp a_i \sigma J \frac{\Delta \iota}{\Delta \iota_i} \times \dots \quad . \tag{2.81}$$

24

Clearly, this transformation only adds a component to the common scaling functions, but is otherwise transparent. With σJ defined by Eqs. (2.73) and (2.79) for arbitrary depths, and assuming that $\Delta \theta_i = \Delta \theta$ the source term becomes

$$
\begin{pmatrix} \delta s_{nl,1} \\ \delta s_{nl,2} \\ \delta s_{nl,3} \\ \delta s_{nl,4} \end{pmatrix} = \begin{pmatrix} -a_1 \Delta f / \Delta f_1 \\ -a_2 \Delta f / \Delta f_2 \\ a_3 \Delta f / \Delta f_3 \\ a_4 \Delta f / \Delta f_4 \end{pmatrix} \frac{C'}{(2\pi)^2} \, B \, \frac{k\sigma}{c_g} \times
$$

$$
\left[\frac{c_{g,1} F_1}{k_1 \sigma_1} \frac{c_{g,2} F_2}{k_2 \sigma_2} \left(\frac{c_{g,3} F_3}{k_3 \sigma_3} + \frac{c_{g,4} F_4}{k_4 \sigma_4} \right) - \frac{c_{g,3} F_3}{k_3 \sigma_3} \frac{c_{g,4} F_4}{k_4 \sigma_4} \left(\frac{c_{g,1} F_1}{k_1 \sigma_1} + \frac{c_{g,2} F_2}{k_2 \sigma_2} \right) \right] , \quad (2.82)
$$

For deep water with σJ defined by Eqs. (2.74) and (2.79), and using Eq. (2.3), the expression for the source term is greatly simplified

$$
\begin{pmatrix} \delta s_{nl,1} \\ \delta s_{nl,2} \\ \delta s_{nl,3} \\ \delta s_{nl,4} \end{pmatrix} = \begin{pmatrix} -a_1 \Delta f / \Delta f_1 \\ -a_2 \Delta f / \Delta f_2 \\ a_3 \Delta f / \Delta f_3 \\ a_4 \Delta f / \Delta f_4 \end{pmatrix} \frac{C'}{2^2 (2\pi)^{10}} \, g^{-4} f^{11} \times
$$

$$
\left[\frac{F_1}{a_1^4} \frac{F_2}{a_2^4} \left(\frac{F_3}{a_3^4} + \frac{F_4}{a_4^4} \right) - \frac{F_3}{a_3^4} \frac{F_4}{a_4^4} \left(\frac{F_1}{a_1^4} + \frac{F_2}{a_2^4} \right) \right] . \quad (2.83)
$$

Finally adopting the frequency grid from Eq. (1.8), which implies that $\Delta f_i = a_i \Delta f$, and adopting the quadruplet definition from HHAB (i.e., the values of a_i as summarized in Table 2.1), the DIA of HHAB is reproduced. The constant C of HHAB thus is defined as

$$
C = \frac{C'}{2^2 (2\pi)^{10}} . \quad (2.84)
$$

The latter two equations will be used to asses the (potential) performance of the (M)DIA in restricted water depth. However, the scaling function B for restricted water depths needs to be considered before such an assessment can be made.

2.5   Scaling considerations

The scaling factor B has two contributions, as discussed in the context of Eq. (2.5). First, the contribution of the interaction coefficient will be considered [B_2 in Eq. (2.5)]. This function is defined by the substitution of the coefficient G in Eq. (1.11) with a constant included in C' in Eq. (2.9),

$$
G \propto B_2 \, C' . \quad (2.85)
$$

In Eq. (2.6) a valid deep water expression is given for B_2. Being expressed in terms of the frequency f only, this scaling factor is invariant with depth. However, it is well known that the coupling coefficient G is sensitive to depth. It may thus be useful to reconsider the scaling function to optimally capture the depth sensitivity of G. This approach is fundamentally different from the approach introduced in the original DIA (WAMDIG, 1988). The present approach considers scaling locally in the phase space, whereas the latter applies a global rescaling after all interactions have been computed. It should be noted that even if the B_2 captures the changes of G with depth perfectly, this is no guarantee that the corresponding MDIA will deal with restricted water depth appropriately. The latter depends also on the representativeness of the quadruplets chosen.

Expression for the coupling coefficient G for arbitrary water depths have first been presented by Herterich and Hasselmann (1980), henceforth denoted as HH80. Corresponding deep-water expressions were earlier given by Webb (1978), although the latter paper contained several errors (e.g., Dungey and Hui, 1979). The present study follows HH80, particularly their Appendix B. At the center of the interaction coefficient stands the complex function D [HH80 Eqs. (B1) and (B2)].

$$D = \frac{1}{3} \left(D_{\boldsymbol{k}_1 \boldsymbol{k}_2 - \boldsymbol{k}_3}^{\;1\;\;1\;-1} + D_{\boldsymbol{k}_2 - \boldsymbol{k}_3 \boldsymbol{k}_1}^{\;1\;-1\;\;1} + D_{-\boldsymbol{k}_3 \boldsymbol{k}_2 \boldsymbol{k}_2}^{-1\;\;1\;\;1} \right) \;, \qquad (2.86)$$

with

$$
\begin{aligned}
D_{\boldsymbol{k}_2 \boldsymbol{k}_2 \boldsymbol{k}_3}^{s_1 s_2 s_3} =\; & \frac{i D_{23}}{\sigma_{23}^2 - (\sigma_2 + \sigma_3)^2} \left\{ 2(\sigma_1 + \sigma_2 + \sigma_3) \left(\frac{\sigma_1^2 \sigma_{23}^2}{g^2} - \boldsymbol{k}_1 \cdot \boldsymbol{k}_{23} \right) \right. \\
& \left. - \frac{\sigma_1 k_{23}^2}{\cosh^2 k_{23} d} - \frac{(\sigma_2 + \sigma_3) k_1^2}{\cosh^2 k_1 d} \right\} - i D_{23} \frac{\sigma_1}{g^2} \left(\sigma_1^2 + \sigma_{23}^2 \right) \\
& + E_{23} \left\{ \frac{\sigma_1^3 (\sigma_2 + \sigma_3)}{g} - g \boldsymbol{k}_1 \cdot \boldsymbol{k}_{23} - \frac{g k_1^2}{\cosh^2 k_1 d} \right\} \\
& + \frac{\sigma_1}{2g^2} (\boldsymbol{k}_2 \cdot \boldsymbol{k}_3) \left\{ (\sigma_1 + \sigma_2 + \sigma_3)(\sigma_2^2 + \sigma_3^2) + \sigma_2 \sigma_3 (\sigma_2 + \sigma_3) \right\} \\
& - \frac{\sigma_1 \sigma_2^2 k_3^2}{2g^2} (\sigma_1 + \sigma_2 + 2\sigma_3) - \frac{\sigma_1 \sigma_3^2 k_2^2}{2g^2} (\sigma_1 + 2\sigma_2 + \sigma_3) \;, \qquad (2.87)
\end{aligned}
$$

and

$$
\begin{aligned}
D_{23} =\; & i(\sigma_2 + \sigma_3) \left(\frac{\sigma_2^2 \sigma_3^2}{g^2} - \boldsymbol{k}_2 \cdot \boldsymbol{k}_3 \right) \\
& - 0.5 i \left(\frac{\sigma_2 k_3^2}{\cosh^2 k_3 d} + \frac{\sigma_3 k_2^2}{\cosh^2 k_2 d} \right) \;, \qquad (2.88)
\end{aligned}
$$

$$E_{23} = \frac{1}{2g} \left\{ \boldsymbol{k}_2 \cdot \boldsymbol{k}_3 - \frac{\sigma_2 \sigma_3}{g^2} \left(\sigma_2^2 + \sigma_3^2 + \sigma_2 \sigma_3 \right) \right\} \;, \qquad (2.89)$$

26

where $\sigma_i = s_i \sigma(\boldsymbol{k}_i)$, according to the dispersion relation (1.6), $\boldsymbol{k}_{23} = \boldsymbol{k}_2 + \boldsymbol{k}_3$ and $\sigma_{23} = \sigma(\boldsymbol{k}_{23})$. Equation (2.88) is somewhat simplified from HH80 by substituting $k_i \tanh(k_i d) = \sigma_i^2 g^{-1}$. Several observations can be made from these equations. First, they present a complex set of equations, however, the final Eq. (2.87) has no imaginary part. Second, this set of equations is invariant under permutation of the wavenumbers of the quadruplet, as long as the wavenumbers in Eq. (2.87) satisfy the resonance conditions, that is

$$ \boldsymbol{k}_4 = \boldsymbol{k}_1 + \boldsymbol{k}_2 - \boldsymbol{k}_3 \quad . \tag{2.90} $$

Comparing HH80 Eq. (1) with the present Eq. (1.11), the interaction coefficient G is computed from D as

$$ G = \frac{9\pi \ g^4 D^2}{4 \ \sigma_1 \sigma_2 \sigma_3 \sigma_4} \quad . \tag{2.91} $$

Note that this conversion differs from the conversion given by Webb (1978) or Dungey and Hui (1979) in two ways. First, the latter authors consider wave energy spectra instead of wave variance spectra. This adds factors ρg to the source term and product terms, hence introducing a factor $(\rho g)^{-2}$ on the right side of their version of Eq. (2.91). Second, the deep water expression for D in the latter papers includes all three contributions in (2.87), but does not include the factor $\frac{1}{3}$. Hence D in the latter papers is larger by a factor 3 than D in HH80 as used here. The expression for G in the latter papers, therefore, drops the factor 9 in the present Eq. (2.91).

Analysis of Eqs. (2.87) through (2.89) and Eq. (2.91) shows that, in deep water,

$$ B_2 \propto g^4 f^{-4} \left(g^{-4} f^8 \right)^2 \quad , \tag{2.92} $$

where the term in brackets represents the scaling behavior of D, and the term in front of the brackets is contributed by the conversion to G. In deep water, this corresponds to Eq. (2.6). The contribution of the conversion in Eq. (2.91) indeed is expressed in terms of frequencies only, and hence should be equally valid in shallow and deep water. The contribution of D, however, is made up of products of frequencies and wavenumbers, and hence is not expected to produce proper scaling behavior in shallow water. Close inspection of these equations shows that there is no common combination of wavenumbers and frequencies in the terms making up these equations. Hence, there is no obvious way to modify this scaling behavior to be applicable to shallow water. Tentatively, a formulation could be sought that mixes frequency and wavenumber products, without modifying the deep water expression. This implies substituting $2\pi f$ in the contribution of D with $(gk)^{1/2}$, or rewriting Eq. (2.92) as

$$ B_2 = (2\pi)^{-2m} g^{m-4} f^{12-2m} k^m \quad , \tag{2.93} $$

27
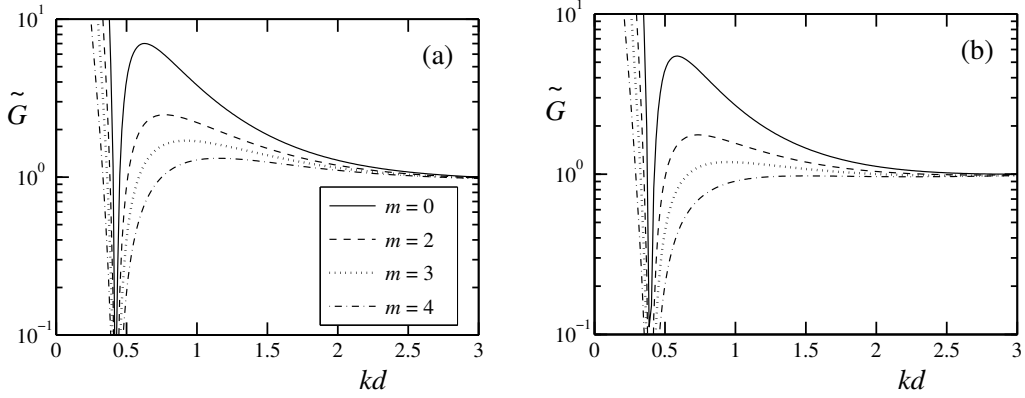
Fig. 2.8 : Normalized nondimensional interaction coefficient $\tilde{G}$ according to Eqs. (2.93) through (2.95) for the traditional one-parameter quadruplet with (a) $\lambda = 0,25$ and (b) $\lambda = 0.15$.
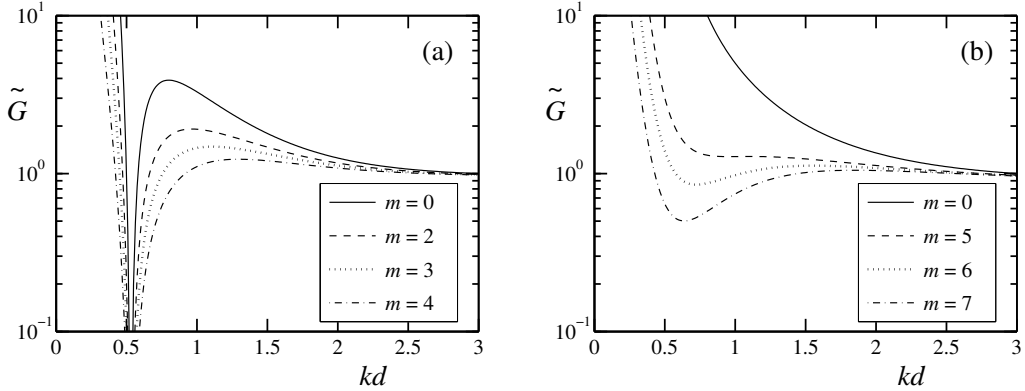
Fig. 2.9 : Like Fig. 2.8 for (a) a two-parameter quadruplet with $\lambda = 0.25$ and $\mu = 0.10$, and (b) a three-parameter quadruplet with $\lambda = 0.25$ and $\mu = 0.10$ and $\Delta\theta = 0°$.

with, tentatively, $m \in [0, 8]$. For $m = 0$ or for deep water in general, this equation reduces to Eq. (2.6). Using this scaling function, a nondimensional interaction coefficient $\hat{G}$ can be defined as

$$\hat{G}(kd) = G(kd)/B_2 \quad , \tag{2.94}$$

which in turn can be normalized as

$$\tilde{G}(kd) = \hat{G}(kd)/\hat{G}(\infty) \quad . \tag{2.95}$$

Examples of $\tilde{G}$ for selected quadruplet definitions are presented in Figs. 2.8 and 2.9. Figure 2.8a presents results for the conventional quadruplet definition of HHAB (one parameter, $\lambda = 0.25$). If G is scaled for deep water only (solid

line), the behavior of G with relative depth is displayed. For relative depths decreasing from 3 (deep water) to about 0.75, G systematically increases by up to an order of magnitude. For shallower depths, G rapidly decreases, until for relative depths just below 0.5 $D = 0$ and changes sign, resulting in $G = 0$. For even smaller relative depths, G again drastically increases. This region of kd space is considered the transition area between weak interactions (in deep water) and strong interactions (in shallow water).

For moderately shallow water (approximately $kd > 0.75 \sim 1$), G is a well behaved function of kd and the scaling function (2.93) with $m \approx 4$ describes the scaling relatively well ($\tilde{G} \approx 1$, chain line in Fig. 2.8a). For smaller relative depths, however, it is obvious that the scaling function cannot represent the behavior of $G(kd)$. This behavior is not typical for the quadruplet chosen. For the one-parameter quadruplet with $\lambda = 0.15$ (Fig. 2.8b), or the two parameter quadruplet with $\lambda = 0.25$ and $\mu = 0.10$ (Fig. 2.9a), similar behavior is found, with subtle but important differences in the location of the relative depth where $G = 0$, and with different optimal values of m in Eq. (2.93). For some quadruplets, however, the behavior is completely different, as is illustrated in Fig. 2.9b with results for the three-parameter quadruplet with $\lambda = 0.25$, $\mu = 0.10$ and $\Delta\theta = 0°$.

Considering the above, a DIA with a scaling factor for G can only be expected to give reasonable results for intermediate water depths with $kd > 0.75 \sim 1.0$. Similarly, the scaling factor for the entire DIA source term as introduced in WAMDIG (1988) is considered adequate for $kd > 1$ only. However, many recent applications of in particular the third generation SWAN model (Booij et al., 1999; Ris et al., 1999) apply the DIA to shallow water including the surf zone, where $kd \ll 1$. In such conditions, a DIA with a bulk scaling function, or a DIA where G is represented with a scaling function line (2.93) is bound to fail. However, due to the small number of quadruplets used in the MDIA, and the feasibility to pre-calculate them, it does not appear necessary to replace the actual interaction expressions (2.87) through (2.91) with a constant and a simple scaling function,

$$B_2 = G(d) \ .$$ (2.96)

Or, in order to be able to revert to the traditional deep water DIA, an appropriate choice would be

$$B_2 = \frac{f^{12} \, G(d)}{g^4 \, G_{\text{deep}}} \ .$$ (2.97)

The behavior with $G \to 0$ for a critical relative depth kd deserves additional attention. If the interactions are dominated by a small number of quadruplet configurations, this might mean that the interactions have a distinct minimum in kd space. This hypothesis appears supported by a narrow band approximation presented by HH80, their Fig. 1. However, these authors also state that their approach has limited validity, particularly in this specific range of relative depths.

Hasselmann and Hasselmann (1985), however, suggests that for practical wind sea spectra, the local minimum in the overall interaction strength for $kd < 1$ does not exist (their Fig. 3). Because a MDIA only considers a small number of interaction configurations, it might be sensitive to reproducing behavior similar to narrow band approximation. This will be addressed in tests in the following section.

This leaves the 'residual' scaling function B_1 in Eq. (2.5). Part of this term arises when the resonance conditions in Eq, (1.11) are used to reduce the number of integration spaces by integrating along paths that satisfy such conditions only. This integration introduces a Jacobian in the integration (see Van Vledder, 2002a, his page 35). Note that this Jacobean is applied along the locus of integration, and will therefore not result in a single scaling factor. However, this Jacobian scales with inverse local group velocities. In the simplified DIA, it therefore appears reasonable to express this Jacobian in terms of the inverse general group velocity c_g corresponding to f, σ and k. A second scaling factor occurs due to the transitions from the vector wavenumber space to the Cartesian definition of the (k, θ) space according to Eq. (2.68). Note that this conversion should be applied to the original integral (1.11), and not to the discrete analogues (2.2). This adds the Jacobian from Eq. (2.68) to three more integration spaces in the detailed balance equation on which (2.2) is based. This more formally defines the scaling factor of Eq. (2.5) as

$$B_1 = k^3 c_g^{-1} \quad , \tag{2.98}$$

which in deep water can be written as

$$B_1 = 2 \left(2\pi\right)^7 g^{-4} f^7 \quad . \tag{2.99}$$

This scaling factor indeed corresponds to the factor of the DIA in Eq. (2.7), with the addition of a constant factor.

2.6   Putting it all together

With all considerations from the previous paragraphs, practical DIAs can be constructed for arbitrary depths and various spectral space descriptions, and for energy or action spectra. In this, the expansion to a multiple DIA according to Eq. (2.63) will be omitted as being trivial. Also, considerations regarding the layout of the quadruplet do not need to be revisited here.

First, contributions to the interactions $\delta s_{nl}(f_i \theta_i) = \delta s_{nl,i}$ for the conventional energy spectrum $F(f_i, \theta_i) = F_i$ will be considered, consistent with the original DIA of HHAB. In this approach, it is also assumed that the frequency grid discretization of Eq. (1.8) is used, as is presently commonplace in third generation

wave models. The corresponding contributions to the nonlinear interactions are found in Eq. (2.82), where the scaling function B of Eq. (2.5) is defined by its constituents B_1 according to Eq. (2.98) and B_2 according to Eq. (2.93) or (2.97)

$$
\begin{pmatrix} \delta s_{nl,1} \\ \delta s_{nl,2} \\ \delta s_{nl,3} \\ \delta s_{nl,4} \end{pmatrix} = \begin{pmatrix} -1 \\ -1 \\ 1 \\ 1 \end{pmatrix} C' \, B' \left[\frac{c_{g,1}F_1}{k_1\sigma_1} \frac{c_{g,2}F_2}{k_2\sigma_2} \left(\frac{c_{g,3}F_3}{k_3\sigma_3} + \frac{c_{g,4}F_4}{k_4\sigma_4} \right) \right.
$$

$$
\left. - \frac{c_{g,3}F_3}{k_3\sigma_3} \frac{c_{g,4}F_4}{k_4\sigma_4} \left(\frac{c_{g,1}F_1}{k_1\sigma_1} + \frac{c_{g,2}F_2}{k_2\sigma_2} \right) \right] \quad , \quad (2.100)
$$

where

$$
B' = \frac{k^{4+m}\sigma^{13-2m}}{(2\pi)^{14}\, g^{4-m}\, c_g^2} \quad , \tag{2.101}
$$

or

$$
B' = \frac{k^4 \sigma^{13} \tilde{G}}{(2\pi)^{14}\, g^4\, c_g^2} \quad , \tag{2.102}
$$

with $\tilde{G}$ being the coefficient G normalized with its deep water value. The deep water equivalent of the scaling factor in terms of f and g only becomes

$$
B' = 2^2 \, (2\pi)^9 \, f^{23} \, g^{-10} \quad . \tag{2.103}
$$

For deep water the full expressions greatly simplify. The expression follows from Eq. (2.83), also accounting for the constant factor in Eq. (2.99)

$$
\begin{pmatrix} \delta s_{nl,1} \\ \delta s_{nl,2} \\ \delta s_{nl,3} \\ \delta s_{nl,4} \end{pmatrix} = \begin{pmatrix} -1 \\ -1 \\ 1 \\ 1 \end{pmatrix} \frac{C'}{2(2\pi)^3} \, g^{-4} f^{11} \times
$$

$$
\left[\frac{F_1}{a_1^4} \frac{F_2}{a_2^4} \left(\frac{F_3}{a_3^4} + \frac{F_4}{a_4^4} \right) - \frac{F_3}{a_3^4} \frac{F_4}{a_4^4} \left(\frac{F_1}{a_1^4} + \frac{F_2}{a_2^4} \right) \right] \quad . \tag{2.104}
$$

Finally, the relation between the proportionality constant of (C) HHAB and the present constant (C') becomes

$$
C = (2\pi)^{-3} \, C' \quad , \tag{2.105}
$$

where a final factor 2 is added to account for the fact that the general quadruplet generates four mirror image representations, whereas the original quadruplet generates only two such contributions.

This expanded DIA for deep water is identical to the DIA presented by HHAB if a_1 through a_2 from the first line of Table 2.1 are substituted, and if the product terms of wave energies are rearranged according to Eq. (2.4). The DIA for arbitrary depths defined by Eqs. (2.100) through (2.102) is considerably more complicated. The product terms in Eq. (2.100) become more complicated due to the inclusion of Jacobians for limited water depths. Second, the scaling function B' according to Eq. (2.101) or (2.102) is more complicated, particularly if the normalized interaction coefficient $\tilde{G}$ is included explicitly. Note, however, that this scaling function is a function of the spectral frequency only, and is therefore not expected to dominate computational costs.

So far, the interactions have been expressed in the traditional wave modeling framework of the wave energy spectrum in terms of the wave frequency and direction $F(f, \theta)$. However, as expressed in the Section 1, the DIA that is being developed here is intended to be implemented in the WAVEWATCH III model. It is therefore more sensible to express the interactions directly in terms of the spectral description used in this model as illustrated in Eq. (1.2). This model uses the action density spectrum as a function of wavenumber and direction, which relates to the above energy spectrum as

$$N(k, \theta) = \frac{c_g}{2\pi \, \sigma} F(f, \theta) \quad , \tag{2.106}$$

With this conversion, the basic expression for the expanded DIA for WAVE-WATCH III becomes

$$
\begin{pmatrix} \delta S_{nl,1} \\ \delta S_{nl,2} \\ \delta S_{nl,3} \\ \delta S_{nl,4} \end{pmatrix}
=
\begin{pmatrix} -1 \\ -1 \\ 1 \\ 1 \end{pmatrix}
C' \, \frac{k^{4+m} \sigma^{12-2m}}{(2\pi)^{12} \, g^{4-m} \, c_g}
$$
$$
\times \left[\frac{N_1}{k_1} \frac{N_2}{k_2} \left(\frac{N_3}{k_3} + \frac{N_4}{k_4} \right) - \frac{N_3}{k_3} \frac{N_4}{k_4} \left(\frac{N_1}{k_1} + \frac{N_2}{k_2} \right) \right], \tag{2.107}
$$

or

$$
\begin{pmatrix} \delta S_{nl,1} \\ \delta S_{nl,2} \\ \delta S_{nl,3} \\ \delta S_{nl,4} \end{pmatrix}
=
\begin{pmatrix} -1 \\ -1 \\ 1 \\ 1 \end{pmatrix}
C' \, \frac{k^4 \sigma^{12} \tilde{G}}{(2\pi)^{12} \, g^4 \, c_g}
$$
$$
\times \left[\frac{N_1}{k_1} \frac{N_2}{k_2} \left(\frac{N_3}{k_3} + \frac{N_4}{k_4} \right) - \frac{N_3}{k_3} \frac{N_4}{k_4} \left(\frac{N_1}{k_1} + \frac{N_2}{k_2} \right) \right]. \tag{2.108}
$$

For deep water the scaling term becomes
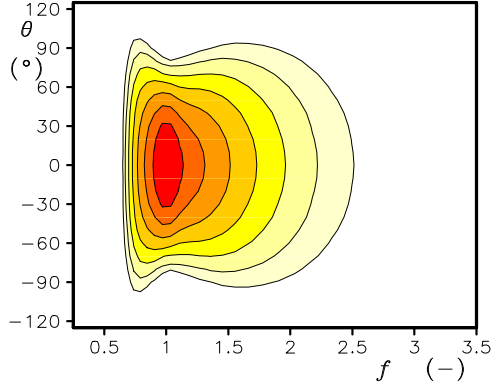
Fig. 2.10 : *Spectrum used for scaling tests. Lowest contour level at 2% of the spectral peak energy density. Contour lines at factor 2 increments. Frequencies relative to peak frequency.*

$$\frac{k^4 \sigma^{12} \tilde{G}}{(2\pi)^{12} g^4 c_g} \rightarrow 2 \, (2\pi)^9 \, g^{-9} \, f^{21} \quad . \tag{2.109}$$

2.7   Testing

The generalized (multiple) DIA developed in the previous sections in principle should have a more realistic shape and scaling behavior than the traditional (multiple) DIA. To be able to design a strategy to optimize the generalized DIA for arbitrary depths, this behavior needs to be tested. Because the testing should focus on the scaling and shape of interaction, a simple test is sufficient here. Considering this, the deep water test of Tolman (2004, 2005) and Tolman and Krasnopolsky (2004) is adopted for arbitrary water depths.

Following the test setup of Section 4.1 of Tolman (2004), a JONSWAP spectrum (Hasselmann et al., 1973) with a peak enhancement factor $\gamma = 2$ and a normalized peak spread $\sigma = 0.07$ are adopted. The directional distribution of Hasselmann et al. (1980), with a switch-over to a parametric tail for higher frequencies consistent with numerical wave models. The spectrum is presented in Fig. 2.10. For the present test, this spectrum is applied for relative depths ranging from deep water ($kd = 10$) to extremely shallow water ($kd = 0.20$), as outlined in Table 2.2. It should be noted that the spectrum of Fig. 2.10 is not representative for the shallowest water conditions in Table 2.2. Because of the focus on shape and scaling of interactions, this is not a major limitation here.

Figure 2.11 presents the exact interactions for the relative depths from Table 2.2. These source terms are computed using the Webb-Resio-Tracy (WRT) (Webb, 1978; Tracy and Resio, 1982; Resio and Perrie, 1991). Calculations are
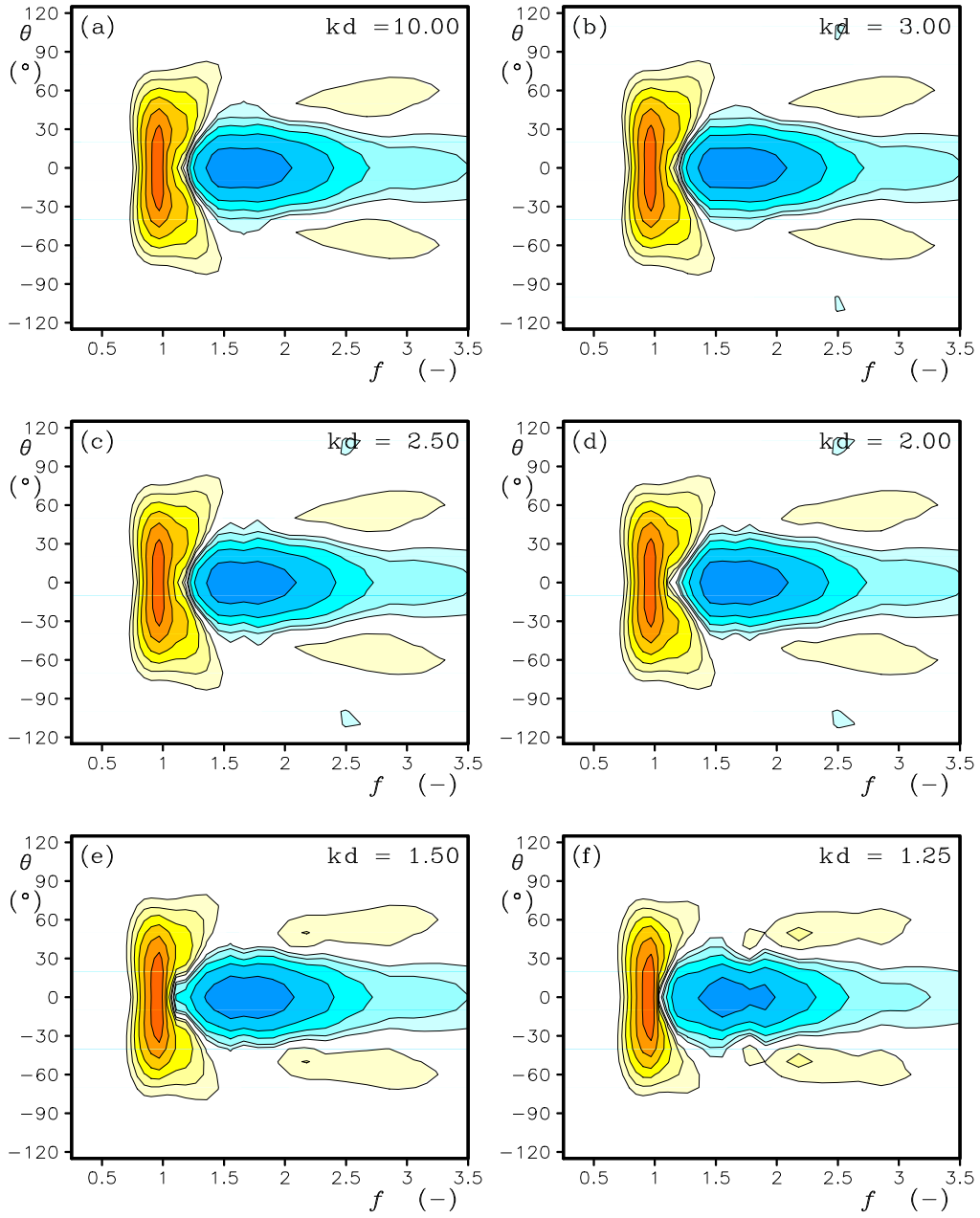
Fig. 2.11 : Exact nonlinear interactions obtained with the WRT method for a range of relative depths (kd). Lowest contour level at ±2% of the maximum absolute interaction per depth. Contours at factor 2 increments. Frequencies relative to peak frequency. Spectrum from Fig. 2.10.
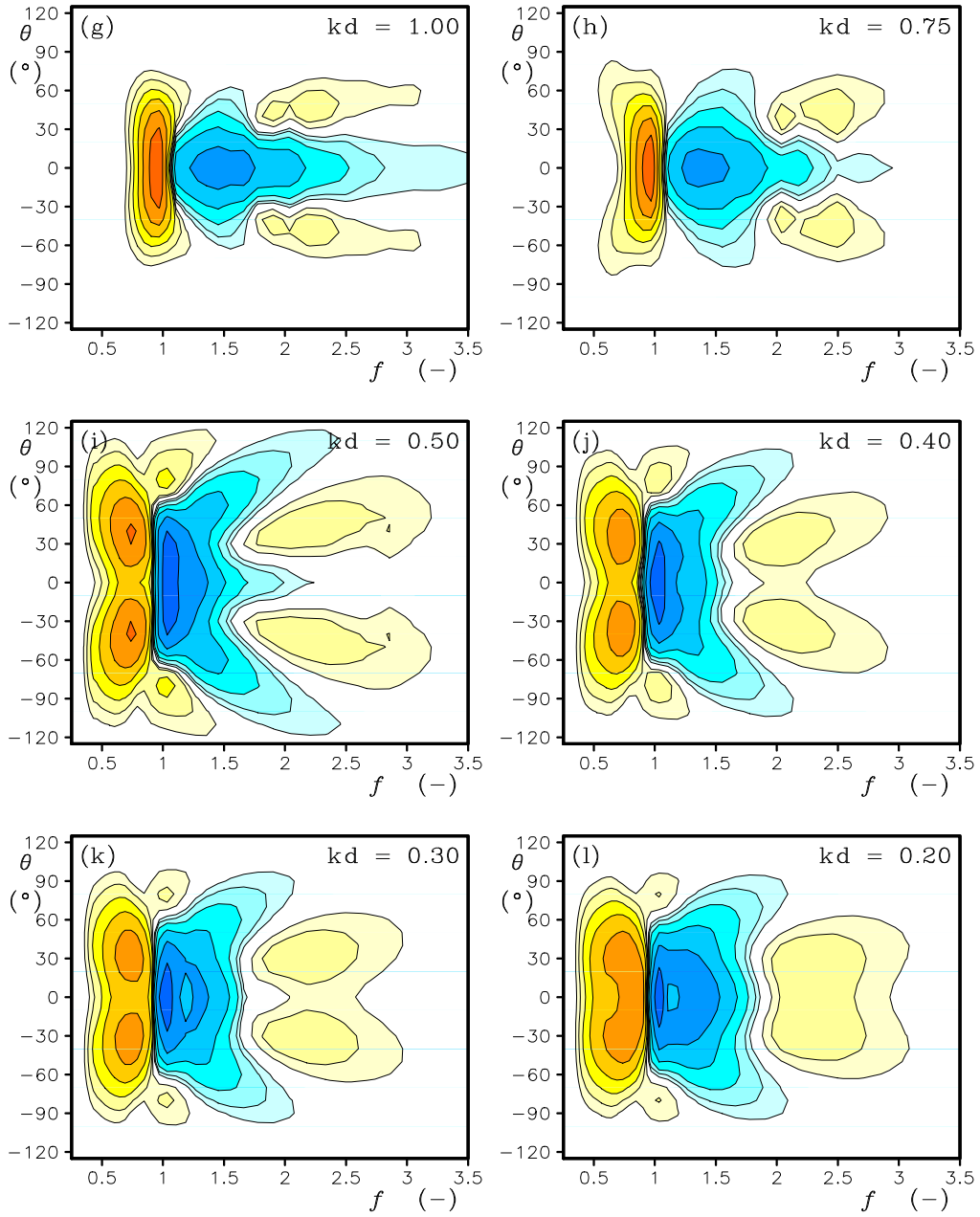
Figure 2.11 continued.

35

Table 2.2: *Relative water depths kd used in the scaling test (top line) and corresponding physical water depths d in meter for a spectral peak frequency $f_p = 0.1Hz$ (second line). The third line presents the normalized scaling factors used in Fig. 2.11 and the bottom line represent the original DIA depth scaling of Eqs. (2.110).*

10.00	3.00	2.50	2.00	1.50	1.25	1.00	0.75	0.50	0.40	0.30	0.20
248.4	74.2	61.3	47.9	33.7	26,3	18,9	11.8	5.74	3.78	2.94	0.98
1	0.972	0.958	0.955	1.03	1.32	1.87	3.70	16.6	173	2740	99400
1	0.928	0.887	0.845	0.877	1.02	1.43	2.51	4.43	4.43	4.43	4.43

performed with the portable package developed by Van Vledder (2002b, 2006)[3]. Each source term is normalized with its own maximum absolute value, so that the focus can be on the spectral shape. The corresponding scale factors are presented at the middle line of Table 2.2. At a later stage source terms obtained with approximations will be normalized with the same values as these WRT results, to asses scaling behavior of approximate solutions with respect to the exact WRT results.

For $kd > 3$, the water is considered to be deep. The corresponding source terms for $kd = 10.00$ and $kd = 3.00$ look virtually identical (Fig. 2.11a,b), and the scaling factors differ by less than 3% (Table 2.2). For depths reduced to $kd = 2.50$, 2.00 and 1.50, source term shapes and scaling factors remain virtually unchanged. For relative depths kd decreasing further to 1.25, 1.00 and 0.75, clear changes in the shape of the source terms start to occur, while the scaling factors start to increase systematically. For relative depths $kd = 0.50$ and smaller, the shape of the source term converts to an apparently different regime, and the scaling factors increase by orders of magnitude. This corresponds to the local minimum of the interaction coefficient $\tilde{G}$ around $kd = 0.5$ as is illustrated in Figs. 2.8 and 2.9, and corresponds to a transition from weak interactions in deeper water to strong interactions in extremely shallow water. Note that the signature of the source term becomes more one-dimensional, with a signature mainly in frequency space.

The first approximate solution for the exact interactions to be considered is the original DIA with $\lambda = 0.306$ and $C = 2.49\,10^6$. These parameter settings represent an optimized traditional DIA for the input spectrum of Fig. 2.10. In the traditional DIA approach, the interaction is always computed for deep water. Effects of shallow water are introduced only by multiplying the deep water interactions with a constant factor D (Hasselmann and Hasselmann, 1985)

$$D = 1 + \frac{5.5}{\bar{k}d}\left[1 - \frac{5}{6}\bar{k}d\right]e^{-1.25\bar{k}d}.$$
(2.110)

---

[3] Model version 5.04 used here.

where $\bar{k}$ represents a conventional mean wavenumber from the spectrum. For numerical reasons, however, the mean relative depth is estimated as

$$\bar{k}d = 0.75\hat{k}d\,, \tag{2.111}$$

where $\hat{k}$ is defined as

$$\hat{k} = \left(\overline{1/\sqrt{k}}\right)^{-2}\,. \tag{2.112}$$

The shallow water correction of Eq. (2.110) is valid for intermediate depths only. For this reason the mean relative depth $\bar{k}d$ is not allowed to become smaller than 0.5.

Figure 2.12 shows the interactions according to the original DIA, scaled with the same values as used in Fig. 2.11 for the exact (WRT) interactions. From the previous sections, it is clear that this approximation does not conserve momentum. Furthermore, the shape of the interactions is independent of depth, and hence this DIA approach by definition cannot reproduce the transition from weak to strong interactions as displayed by the WRT approach. The traditional DIA approach does, however, reasonably capture the change of scales of interactions for relative depths down to $kd = 0.75$. This is also illustrated with the scaling factor D as presented on the bottom line of Table 2.2. For relative depths $kd < 0.5$, the traditional DIA grossly underestimates the strength of the interactions, with the strength of the interactions negligible compared to the corresponding panels in Fig. 2.11. Note that any other modified and or multiple DIA that uses this quasi-deep water approach will suffer from the same behavior and deficiencies and does therefore not need to be discussed in this context.

Figure 2.13 shows the interactions obtained with the proper shallow water quadruplet layout, and the shallow water product term, but still with a scaling function for deep water, i.e., Eqs. (2.100) and (2.103). Note that Eq. (2.105) is used to be able to use the proportionality constant C consistent with the HHAB approach. A comparison of Figs. 2.12 and 2.13 shows that for intermediate depths with $kd \leq 1$ the DIA becomes slightly stronger, without significant changes to the shape of the interactions. Compared to the exact interactions in Fig. 2.11 this can be considered as a minor improvement. For more shallow water, the shape of the interactions seems to change, but the strength of the interactions is even more underestimated than by the original DIA. For the smallest depth, the underestimation is increased by a factor 200, increasing the overall underestimation to eight orders of magnitude for $kd = 0.2$ The changing shape of the interactions can be addressed if the interactions are normalized with their own maximum absolute value (Fig. 2.14). This shows strong interactions at higher frequencies, whereas the exact computations shift the main interactions to lower frequencies (Fig. 2.11). Hence, this partial shallow water DIA represents the strong interactions for depths $ks < 1$ very poorly indeed.
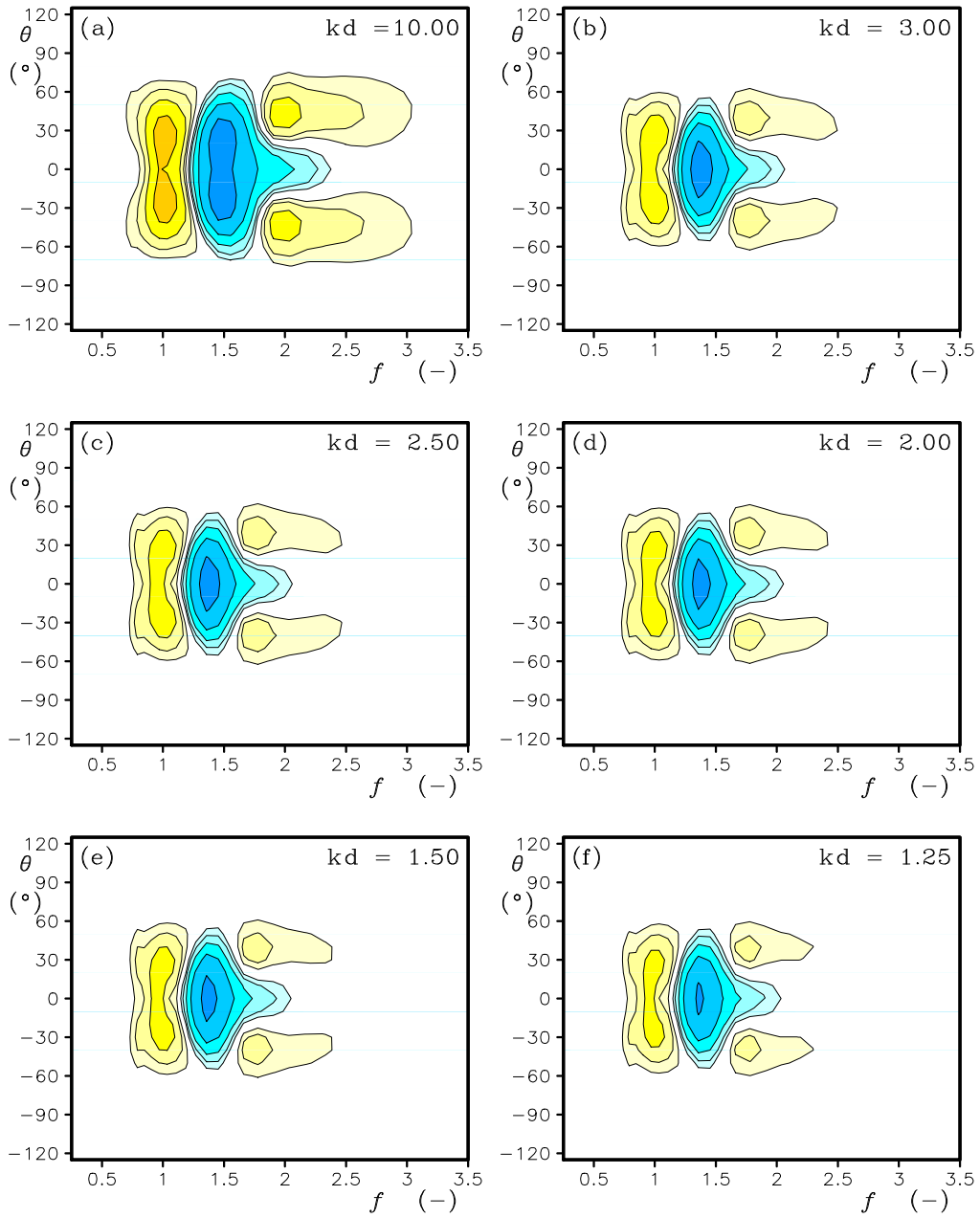
Fig. 2.12 : Like Fig. 2.11 for the traditional DIA approach with $\lambda = 0.306$ and $C = 2.4910^6$. Each panel is scaled with the corresponding maximum absolute source term from the WRT method.
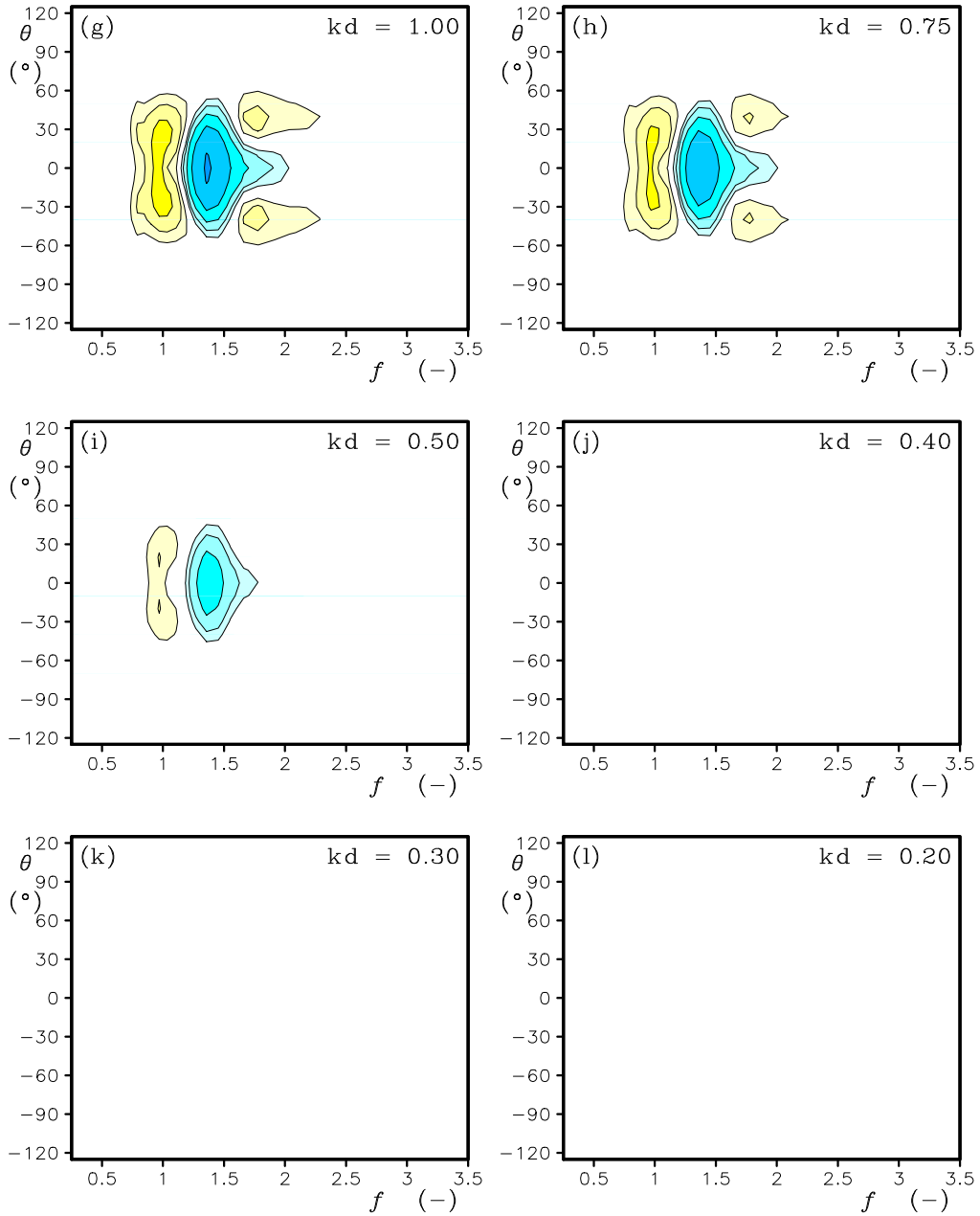
Figure 2.12 continued.
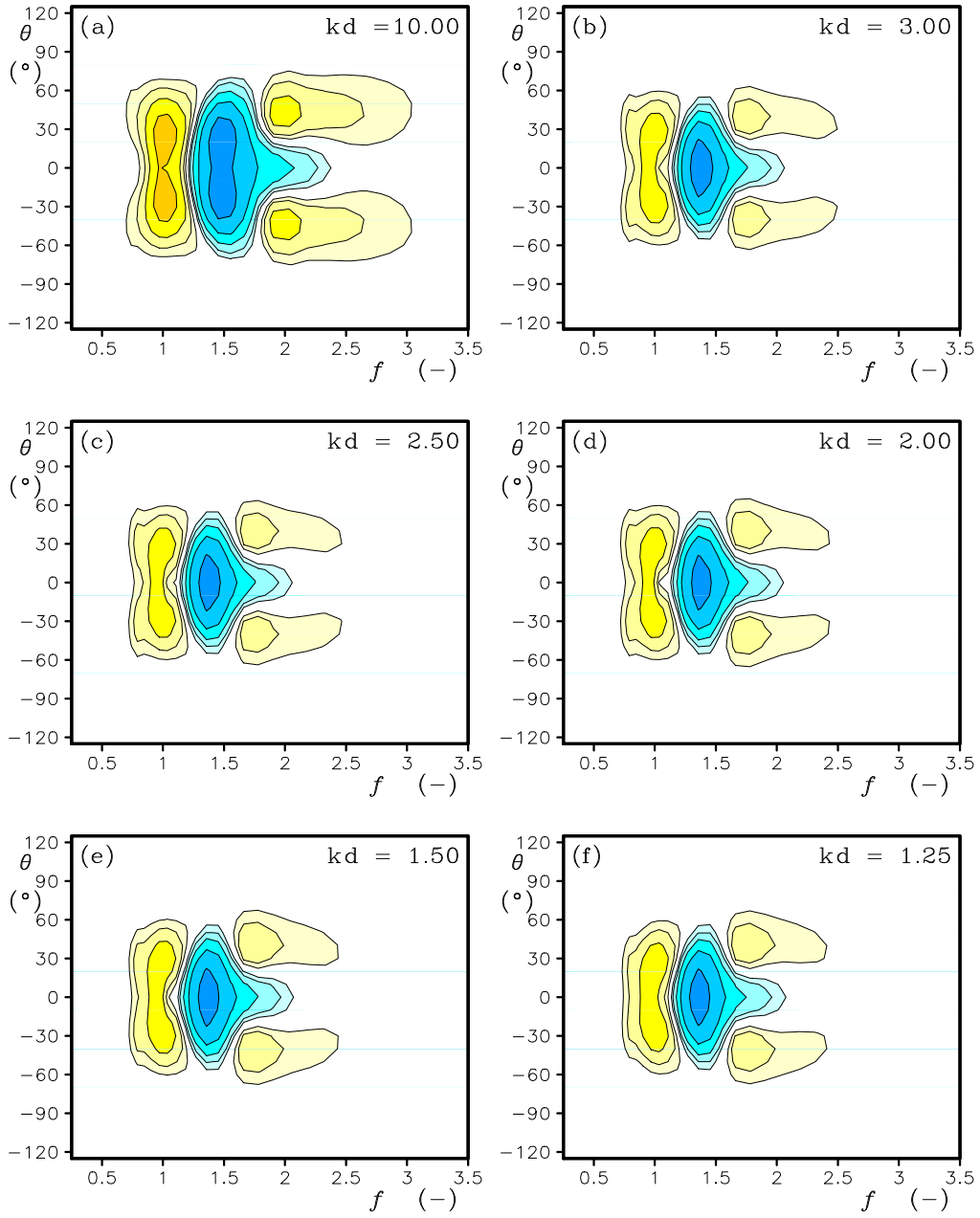
Fig. 2.13 : Like Fig. 2.12 for the traditional DIA approach with $\lambda = 0.306$ and $C = 2.49\,10^6$, but using the shallow water dispersion relation in the determination of the quadruplet layout, and with the proper form of the product terms for shallow water.

40
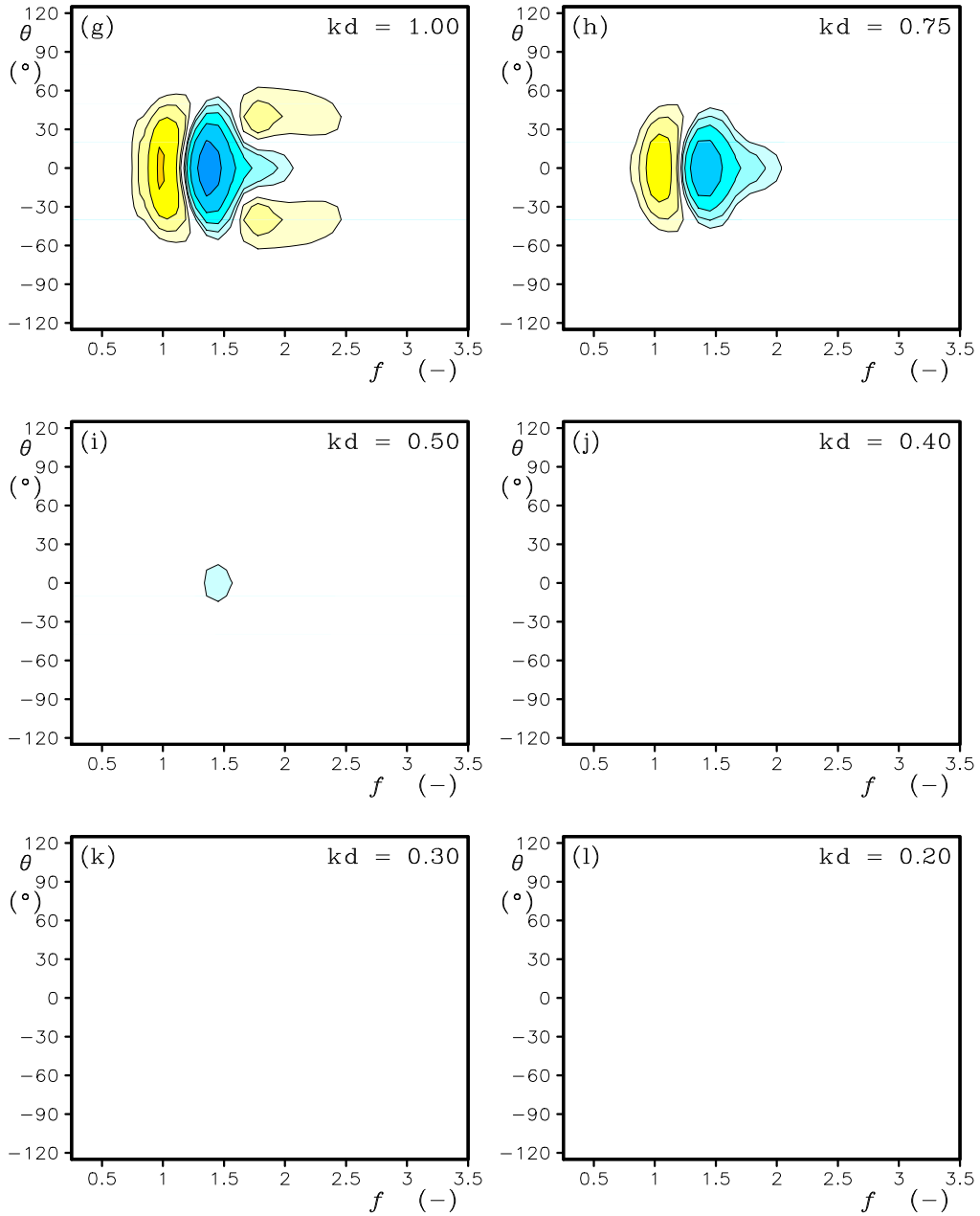
Figure 2.13 continued.
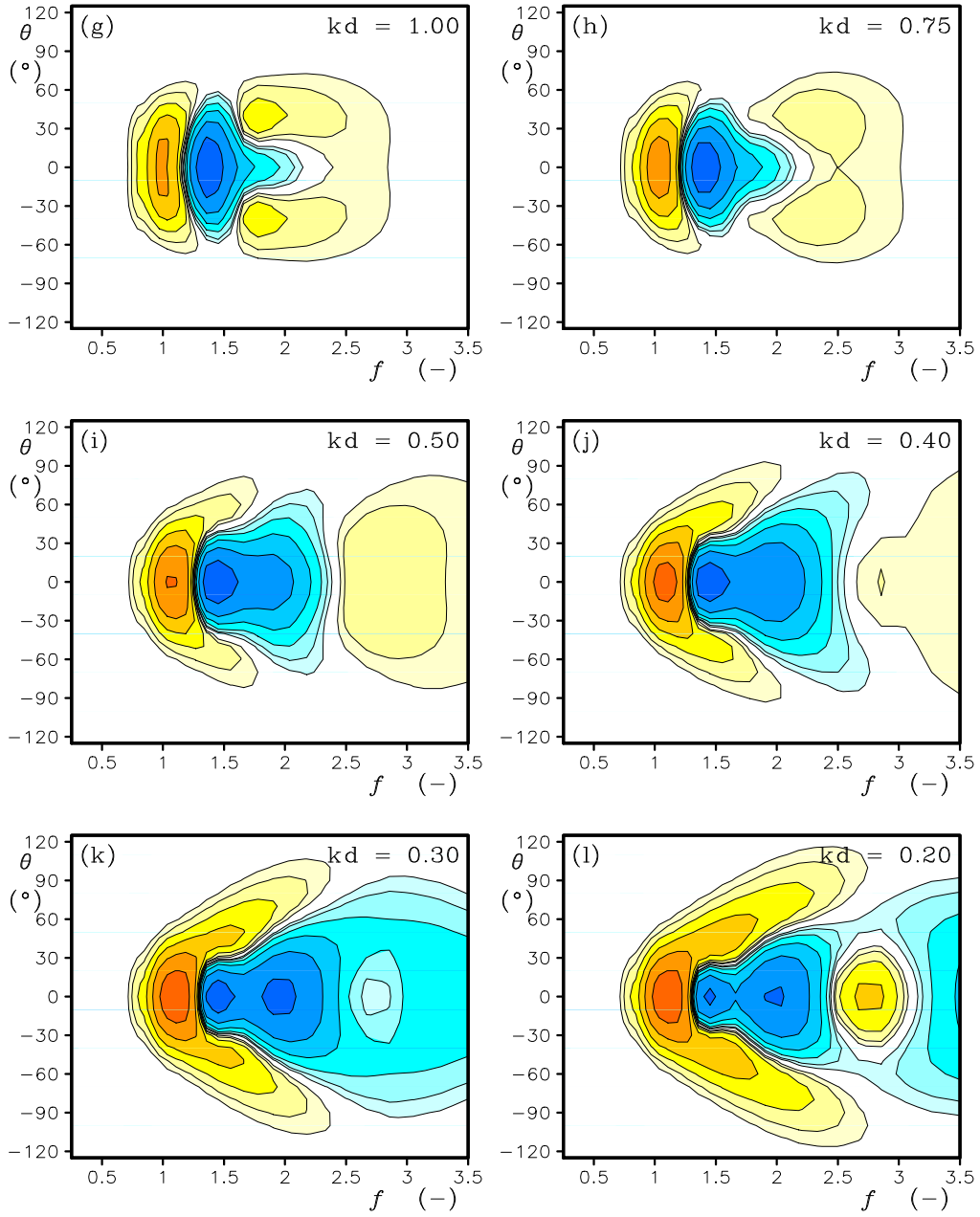
Fig. 2.14 : Like Fig. 2.13, scaled with maximum interaction for the DIA at each relative depth.
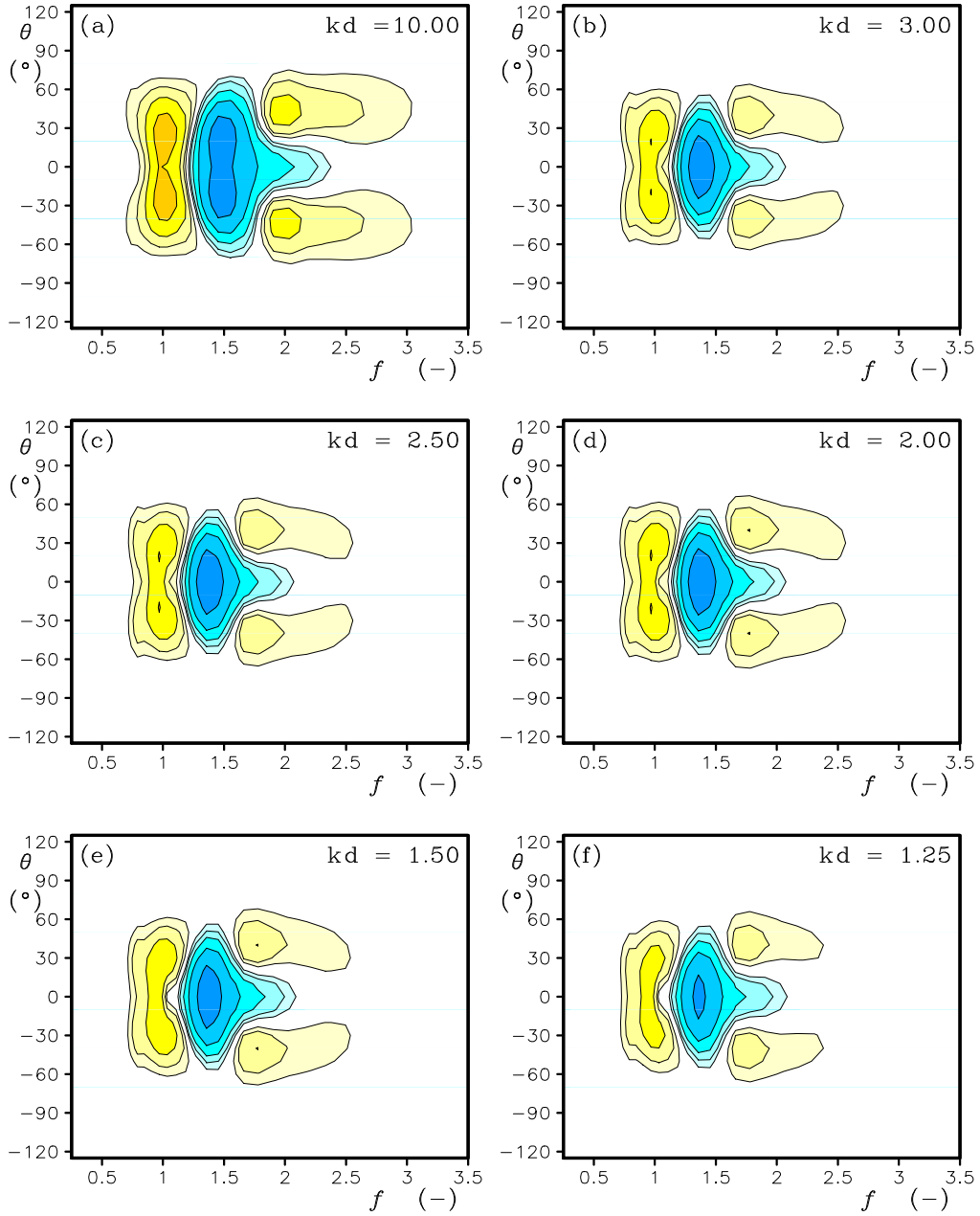
Fig. 2.15 : Like Fig. 2.12 for the expanded DIA approach of Eqs. (2.100) and (2.101) with $\lambda = 0.306$, $C = 2.49\,10^6$, and $m = 0$.
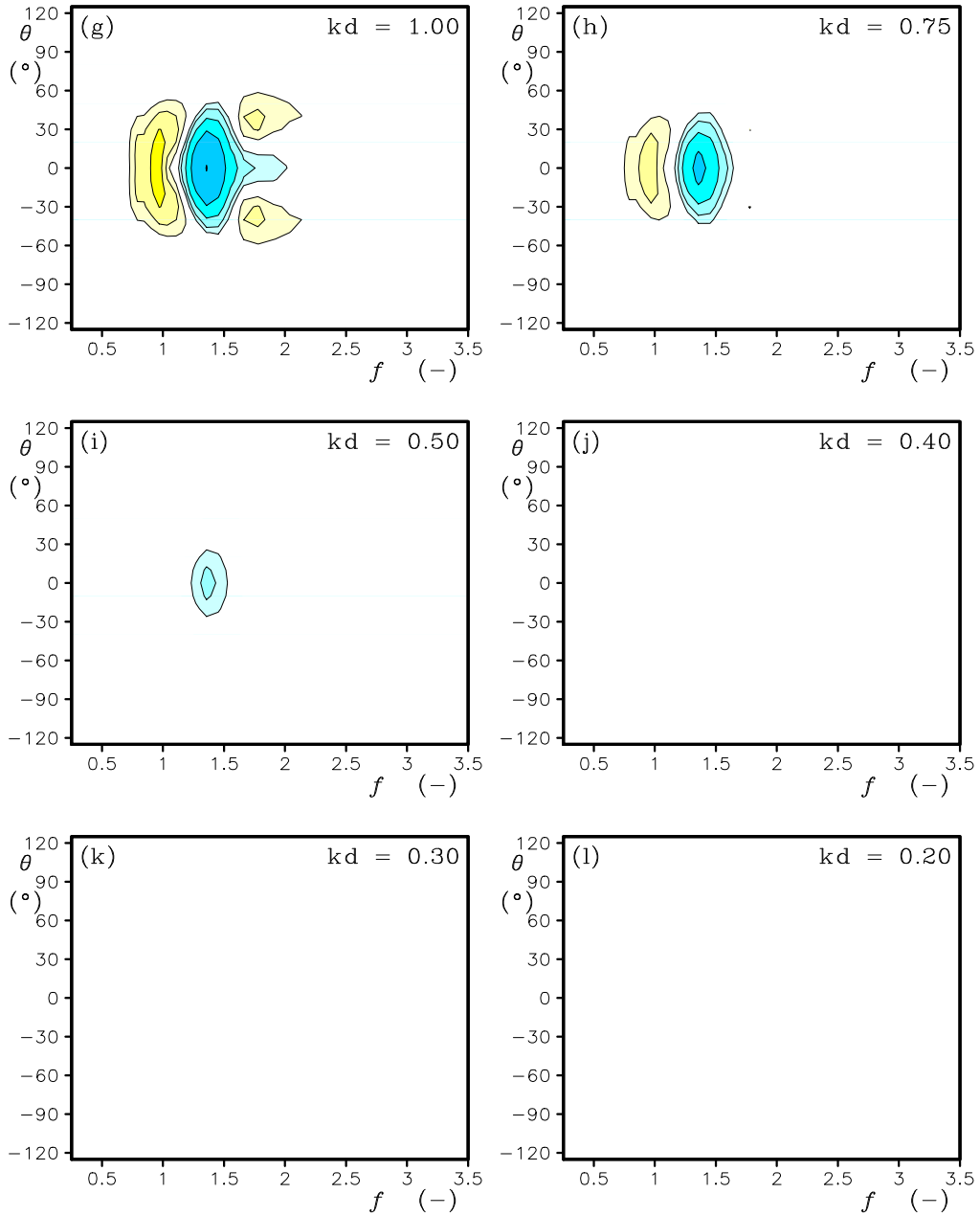
Figure 2.15 continued.

44
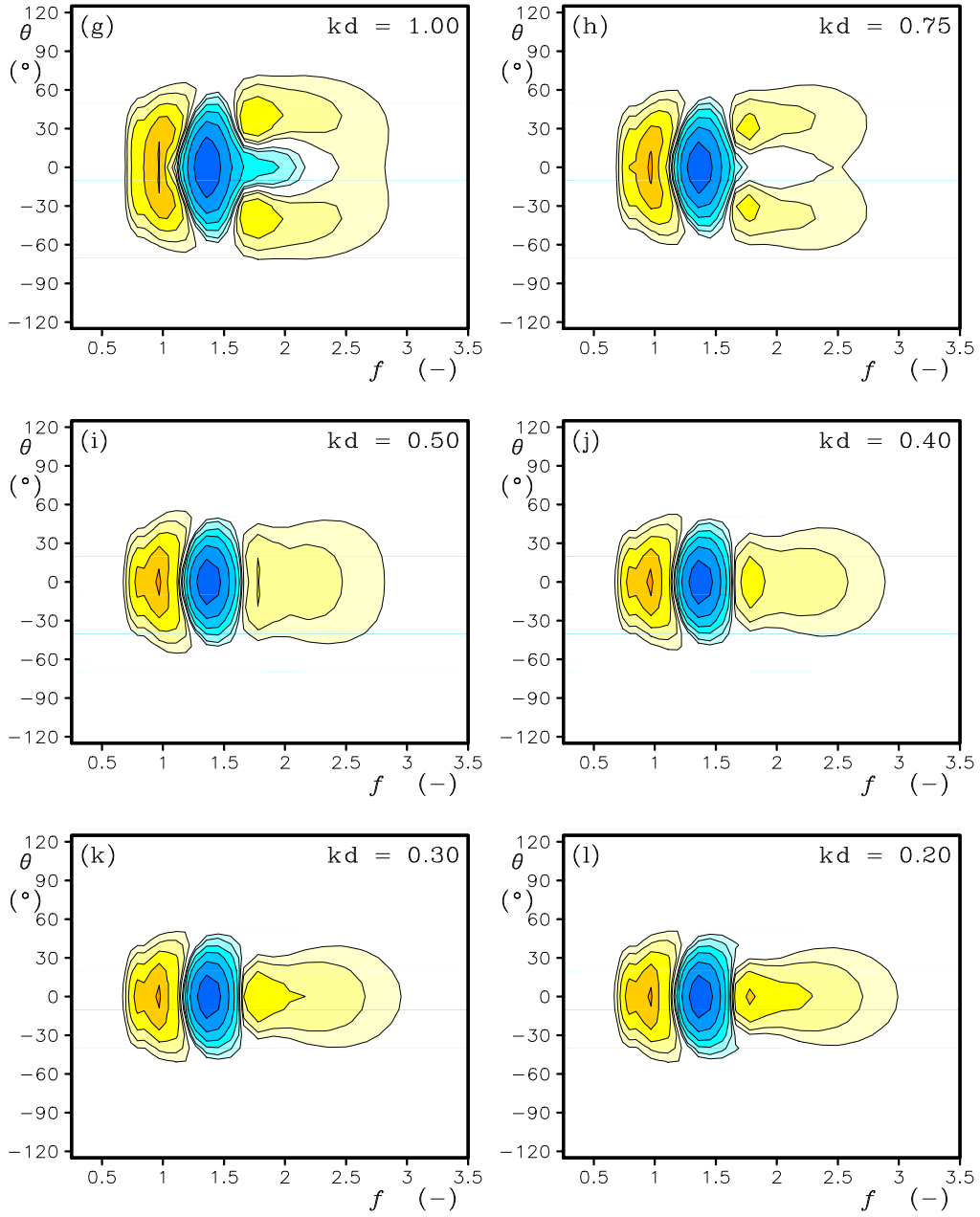
Fig. 2.16 : Like Fig. 2.15, scaled with maximum interaction for the DIA at each relative depth.

The next incremental adjustment of the DIA is to incorporate the scaling function of Eq. (2.101). Figure 2.15 shows the results for $m = 0$. This corresponds to adoption the proper shallow water form of the 'residual' scaling factor B_1 of Eq. (2.98), but retaining the deep water form of the scaling function B_2 for the interactions coefficient G from Eq. (2.6). For intermediate water depths with $kd < 1$, results remain very similar to those of the original DIA from Fig. 2.12. For more shallow water, the underestimation of the strength of the interaction now is also virtually identical to the underestimation of the original DIA, with an underestimation of five orders of magnitude for $kd = 0.2$. The shape of the interactions for shallow water, however, is much more realistic than when the deep water scaling function is used (compare Figs. 2.16, 2.14, and 2.11).

Some of the shallow water scaling of the coupling coefficient can be introduced by setting $m = 4$ in Eq. (2.101). The results presented in Fig. 2.17 show that this modification expands the range of proper scaling behavior to depths as low as $kd = 0.5$. For $kd = 0.2$, the underestimation of the strength of the interactions is reduced to a factor of approximately 150, down from five orders of magnitude for the original DIA. The shape of the interactions for these extremely small depths also remains much more realistic (Fig. not shown here). Further increase of m reduces the scaling errors for extremely shallow depths even further, with results for $m = 7$ giving near-perfect scaling behavior for $kd = 0.35$. This is illustrated in Fig. 2.18. Note that the improved behavior for extremely shallow water is achieved at the cost of an overestimation of the strength for intermediate depths ($kd \approx 1$), and that the asymptotic scaling behavior for $kd \to 0$ does not match that of the WRT method.

One reason why the expanded DIA does not seem to be able to reproduce the scaling behavior of the WRT method for extremely shallow water, is because the scaling function (2.101) is not set up for such conditions. Using the shallow water dispersion relation

$$\sigma^2 = k^2 \, gd \quad , \tag{2.113}$$

and using this to replace frequencies in the scaling function except for B_1 results in

$$B' = g^2 \, (2\pi)^{-14} \, k^{11} \, c_g^{-1} \, (kd)^n \quad . \tag{2.114}$$

where theoretically $n = 6$, but where n can be considered as a tunable constant. Numerical experiments show that $n = -3.5$ results in reasonable scaling behavior for extremely shallow water. This is illustrated in Fig. 2.19. If the resulting interactions are rescaled by an additional factor 0.08, results for $kd < 0.5$ show excellent scaling behavior compared to the exact WRT results. For larger depths the interactions now are too small, and virtually disappear for $kd > 0.75$. Because this equation gives good scaling for shallow depths, and virtually no interactions
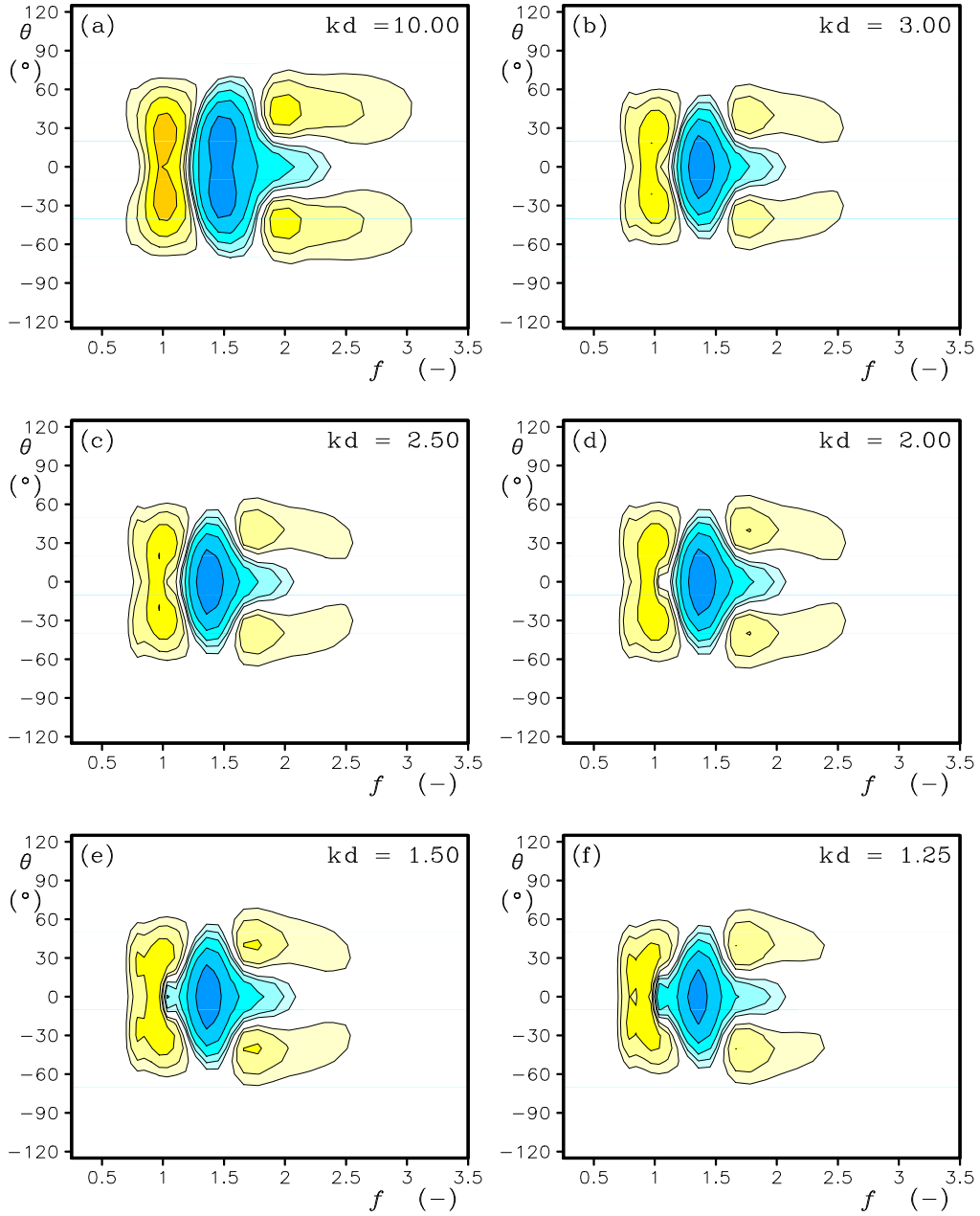
Fig. 2.17 : Like Fig. 2.12 for the expanded DIA approach of Eqs. (2.100) and (2.101) with $\lambda = 0.306$, $C = 2.49\,10^6$, and $m = 4$.
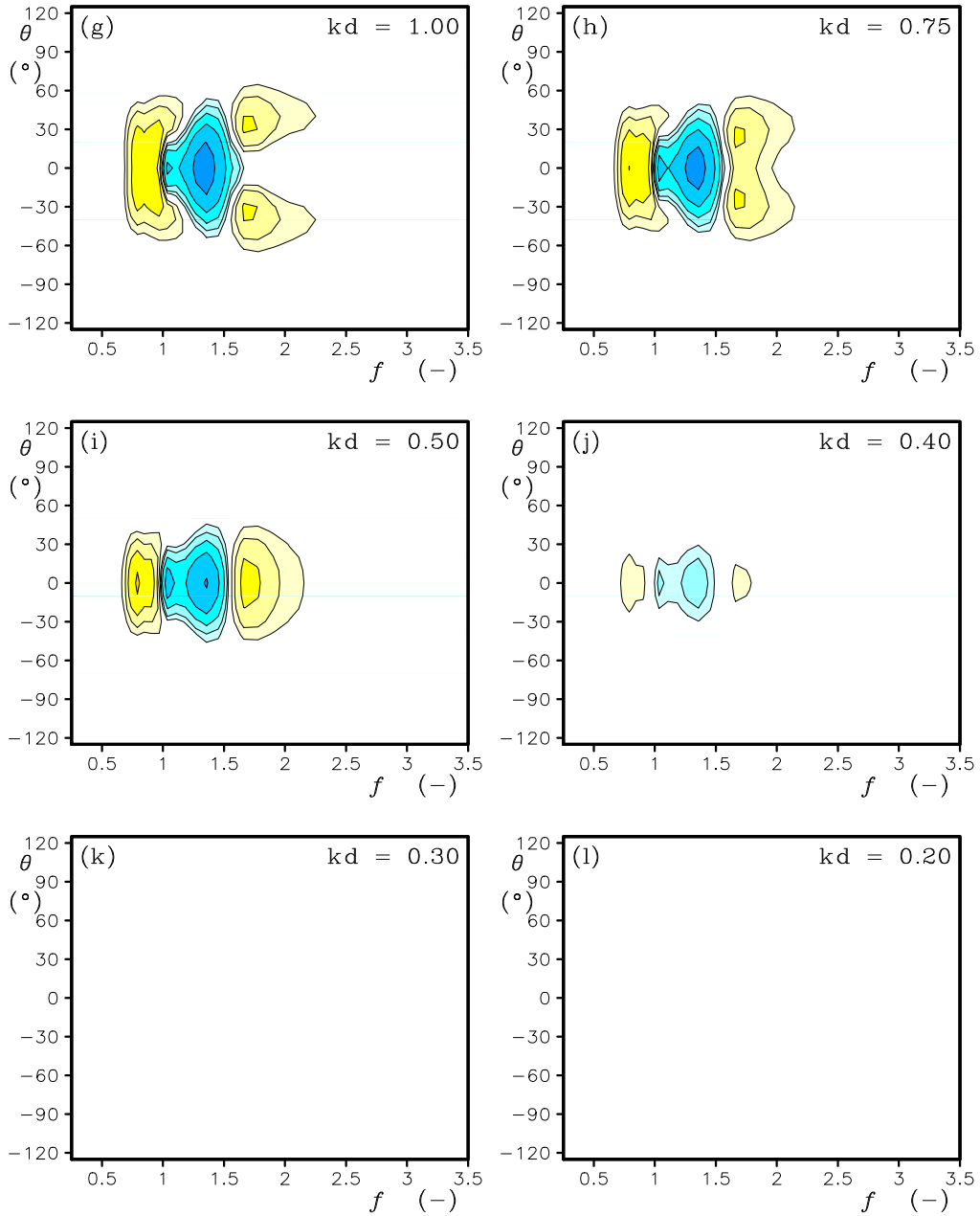
Figure 2.17 continued.

48
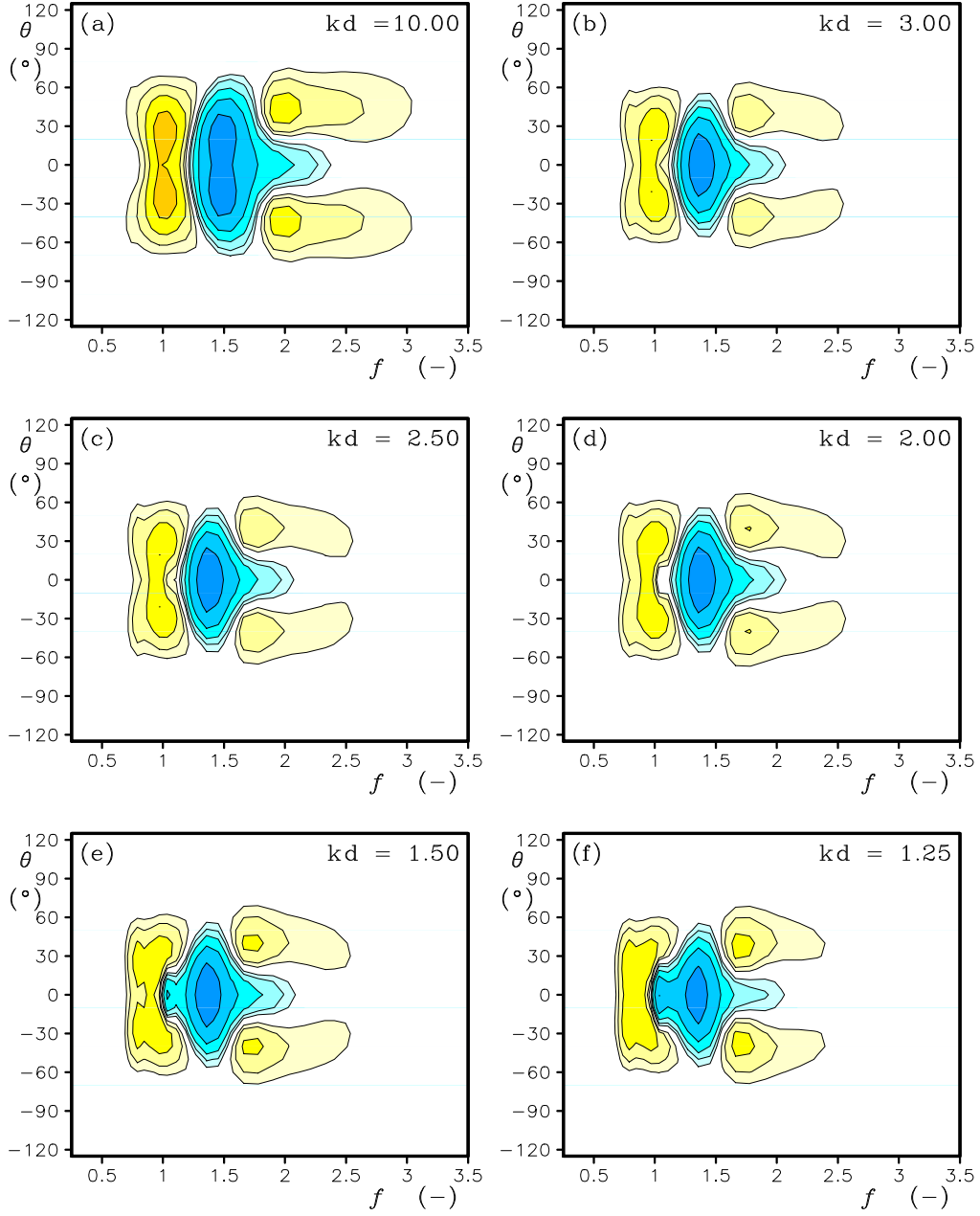
Fig. 2.18 : Like Fig. 2.12 for the expanded DIA approach of Eqs. (2.100) and (2.101) with $\lambda = 0.306$, $C = 2.49\,10^6$, and $m = 7$.
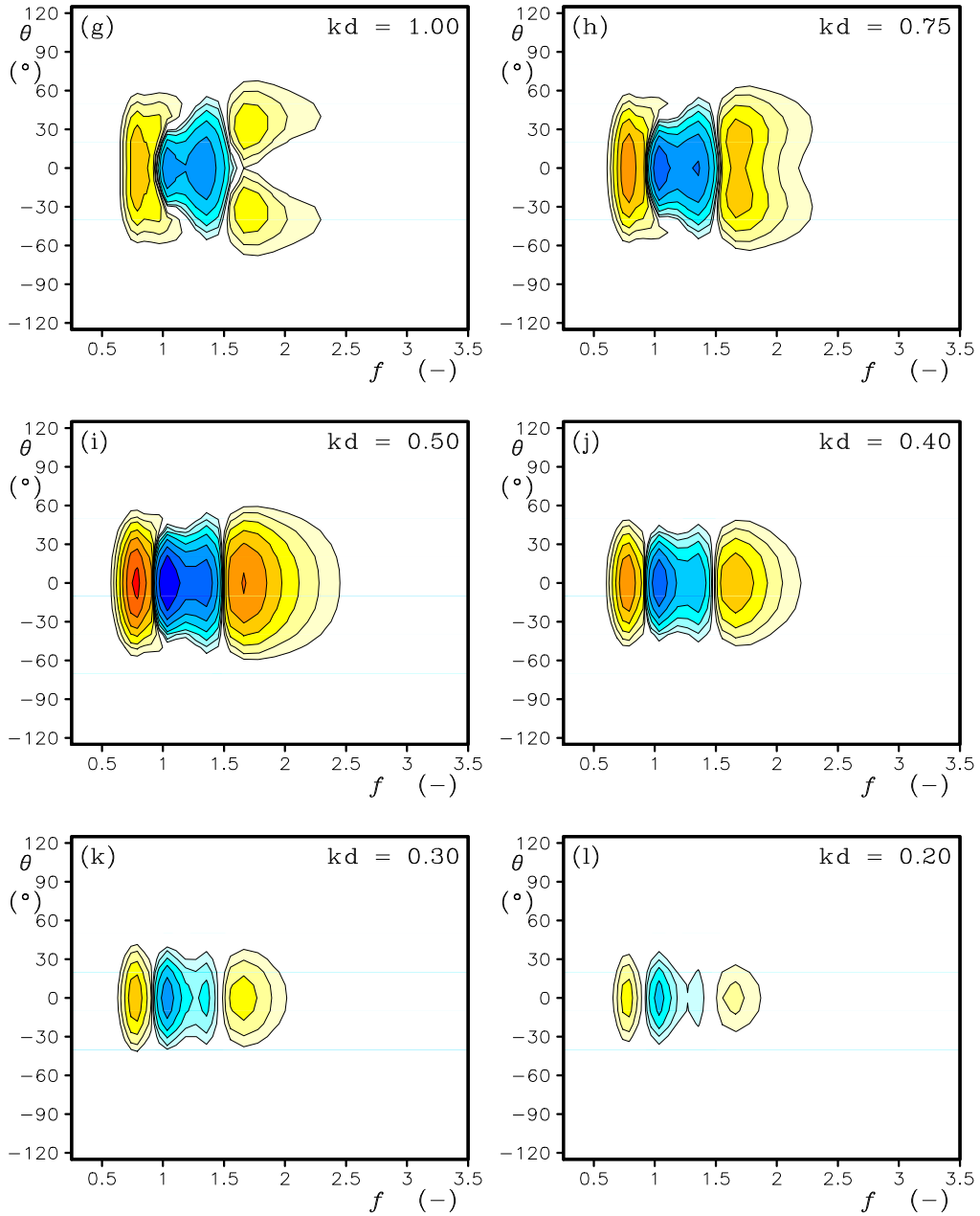
Figure 2.18 continued.

50
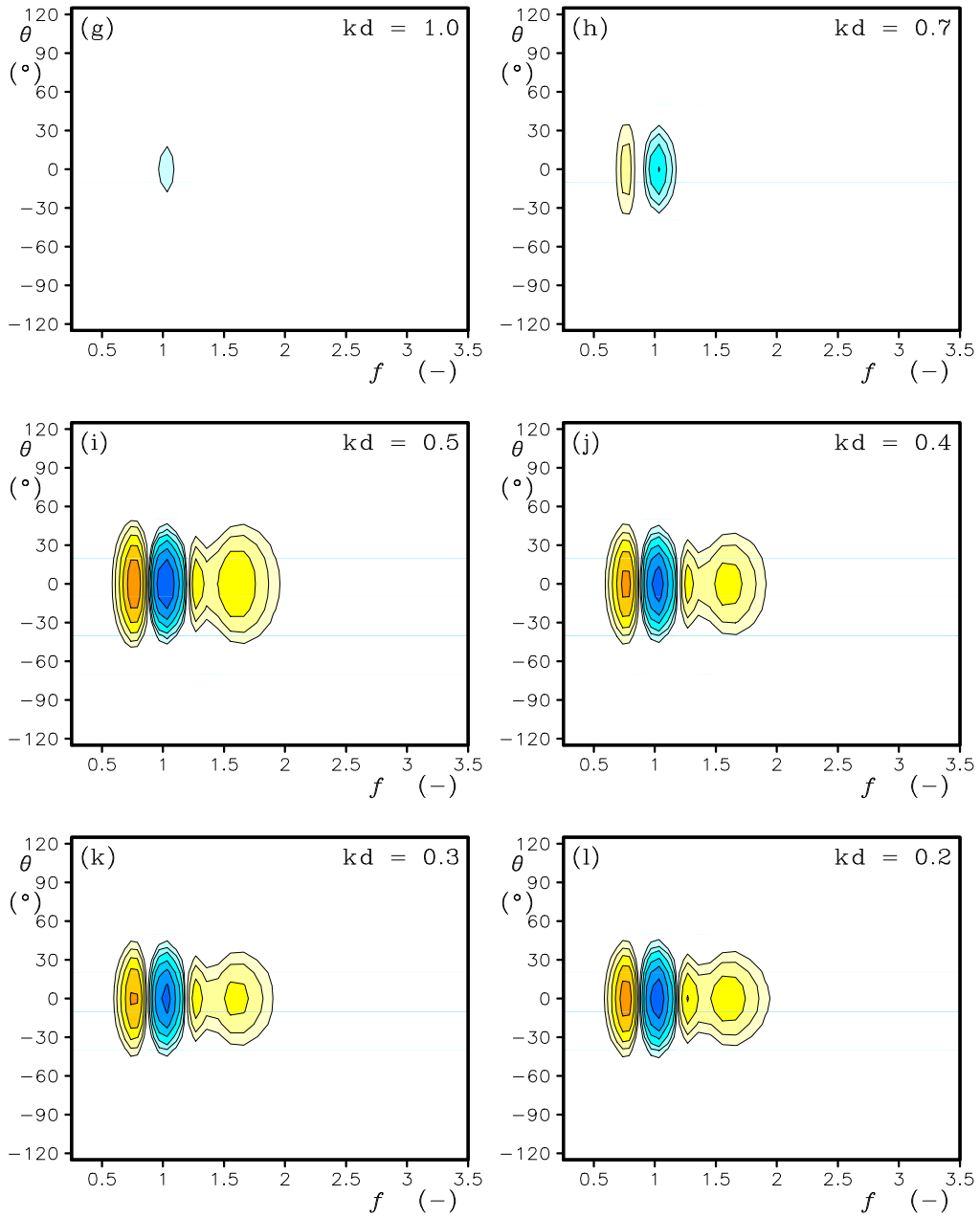
Fig. 2.19 : Like Fig. 2.12 for the expanded DIA approach of Eqs. (2.100) and (2.104) with $\lambda = 0.306$, $C = 2.49 10^6$, and $n = -3.5$. All sources rescaled with local WRT value and an additional factor of 0.08.

51
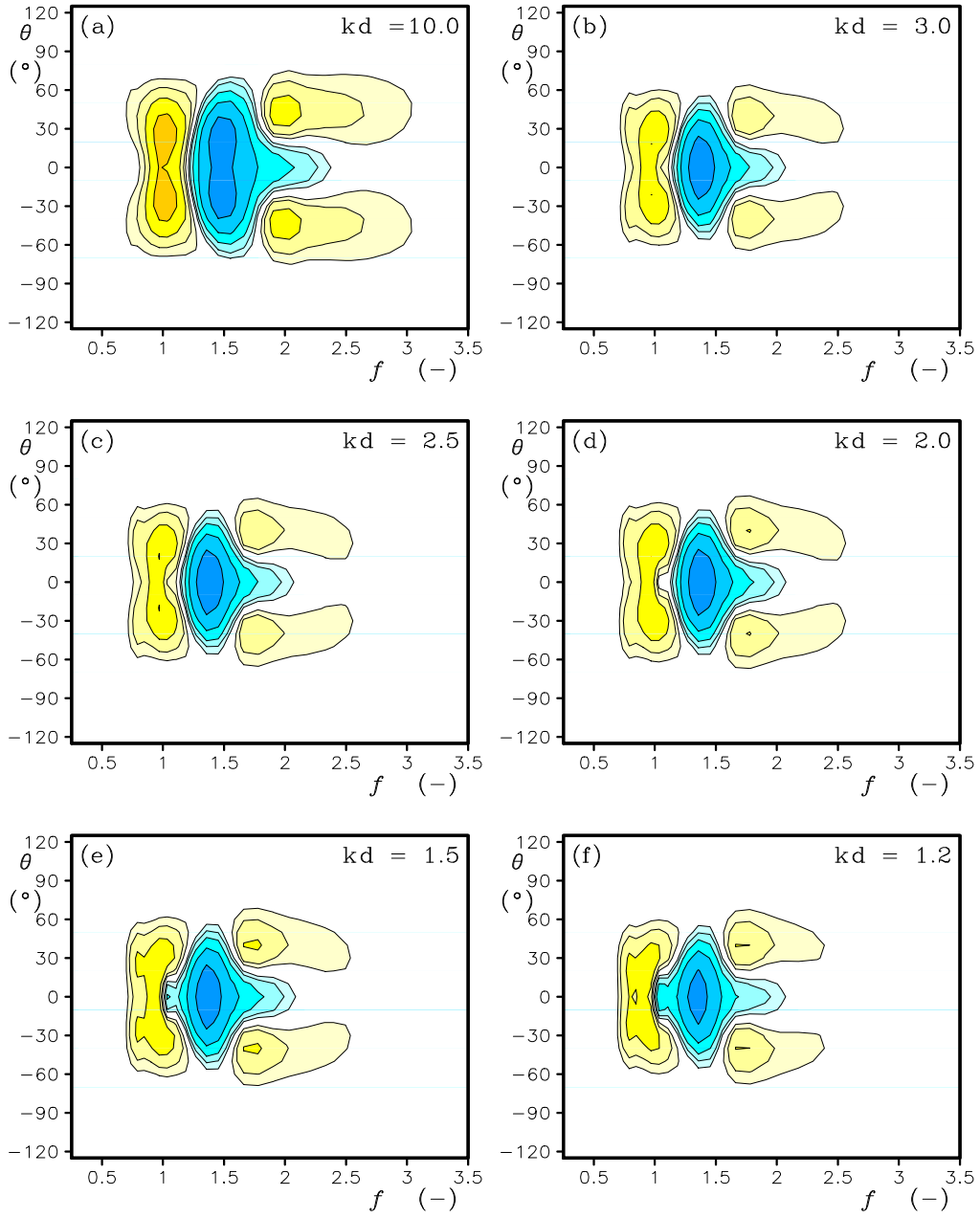
Fig. 2.20 : Like Fig. 2.12 for the expanded DIA approach of Eqs. (2.100) and (2.115) with $\lambda = 0.306$, $C = 2.49\,10^6$, $m = 4$, $n = -5.5$ and $C'_s = 3.8\,10^{-6}$.
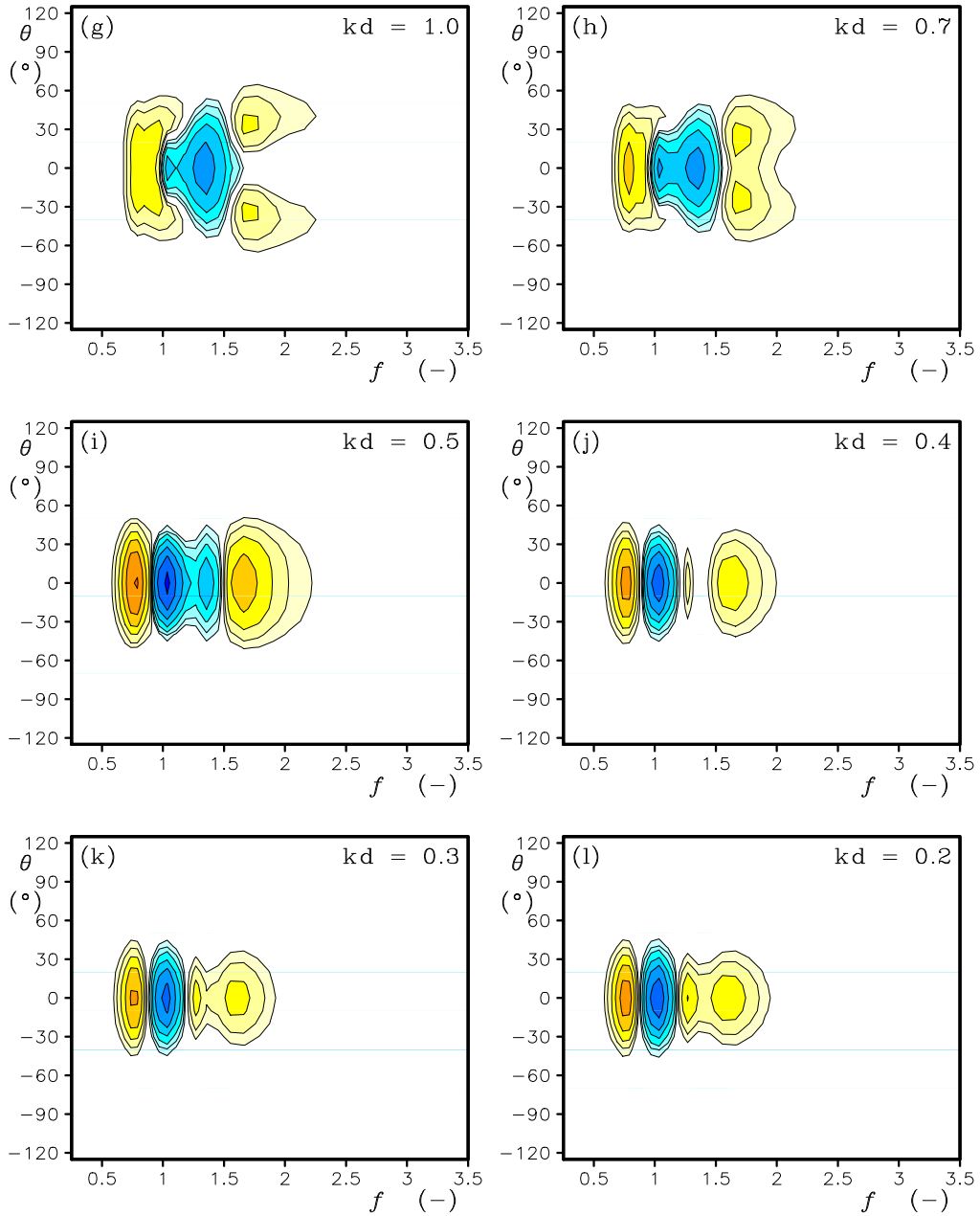
Figure 2.20 continued.

53

for deep water, and because Eq. (2.101) shows the opposite behavior, it is logical to combine the two scaling behaviors in a single formulation

$$B' = \frac{k^{4+m}\sigma^{13-2m}}{(2\pi)^{14}\, g^{4-m}\, c_g^2} + C'_s\, \frac{g^2\, k^{11}\, (kd)^n}{(2\pi)^{14}\, c_g} \quad . \tag{2.115}$$

Figure 2.20 shows the results for the expanded DIA of Eq. (2.100) with this scaling function B' with $m = 4$, $n = -3.5$ and $C'_s = 0.08$. Within the limitations of the DIA with a single quadruplet to reproduce the shape of the interactions, this DIA accurately reproduces the interactions across the entire range of relative depths considered here.

The final possible upgrade of the DIA to be considered is the introduction of the full nonlinear scaling of the coupling coefficient G by using Eqs. (2.100) and (2.102). Results for this approach with the single component DIA are presented in Fig. 2.21. For water depths $kd > 0.75$ this approach shows reasonable results. For shallower water, however, the scaling behavior is inadequate, with a significant underestimation of the strength of the interactions. Note, however, that this underestimation is typically less than two orders of magnitude, and hence represents a major improvement over the original DIA approaches. Note, furthermore, that there is a small but distinct difference between results for $kd = 10$ and $kd = 3$, suggesting that this approach for a conventional single DIA results in some spurious changes in interaction strength while going from deep water ($kd = 10$) into borderline depth-limited water ($kd = 3$).

Figure 2.22 addresses the shape of the interactions for smaller water depths. Shapes appear reasonable, in spite of the scaling issues encountered. Whereas the interactions are too narrow in directions and frequency compared to the exact interactions (Fig. 2.11), they do shift properly to lower frequencies with regard to the low-frequency positive lobe.

This concludes the tests of the single quadruplet DIA with the expanded formulations developed here. It is clear that the proper shallow water quadruplet layout, proper form of the product term and a proper scaling term all are important in order to obtain a DIA that scales properly across a range of relative depths. It is also clear that there are two distinct ranges of interactions, separated for this DIA for depths around $kd = 0.5$. Previously known limitations of this DIA limit its ability to properly reproduce the shape of the interactions. It is nevertheless encouraging that the interactions become more one-dimensional (oriented in frequency space) as in the WRT approach.

The logical next step is to test a DIA with multiple quadruplets (multiple or MDIA), that has shown the capability to reproduce the shape of the nonlinear interactions more accurately in deep water. An MDIA with four quadruplet layouts defined by two parameters (λ, μ) is used as a first illustration here. The MDIA is moderately optimized and the quadruplet settings are presented in Table 2.3. As
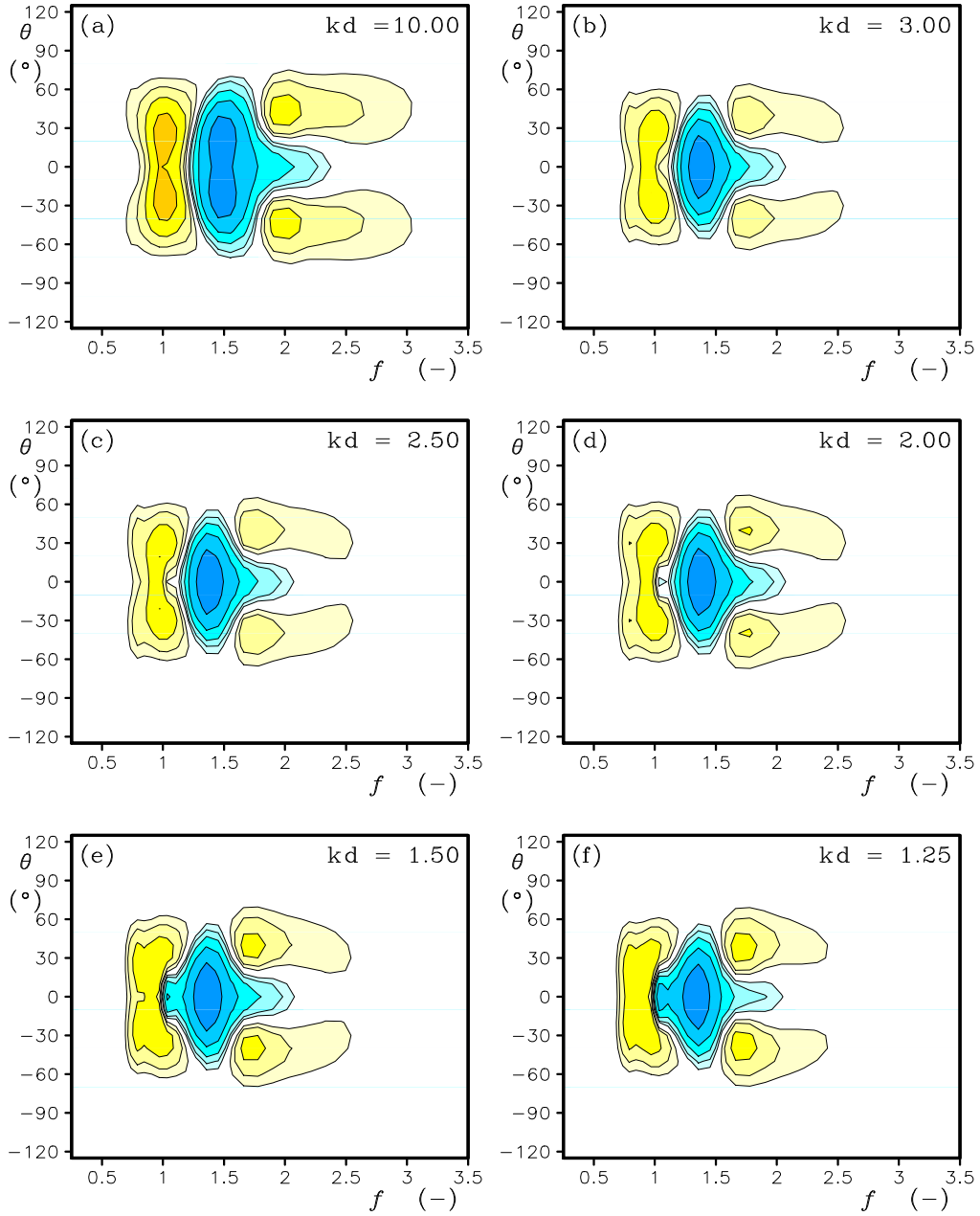
Fig. 2.21 : Like Fig. 2.12 for the expanded DIA approach of Eqs. (2.100) and (2.102) with $\lambda = 0.306$, and $C = 2.49\,10^6$.

55
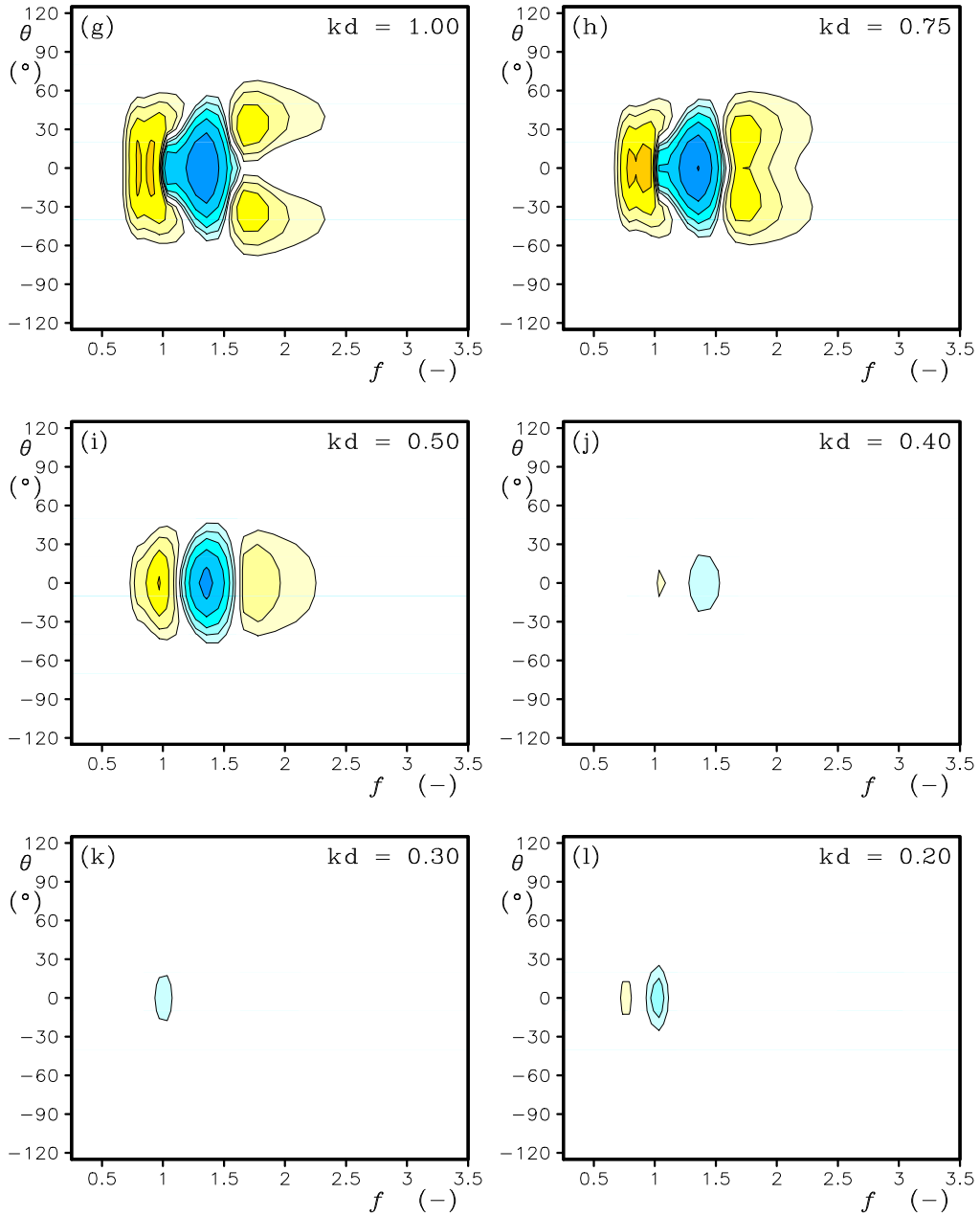
Figure 2.21 continued.

56
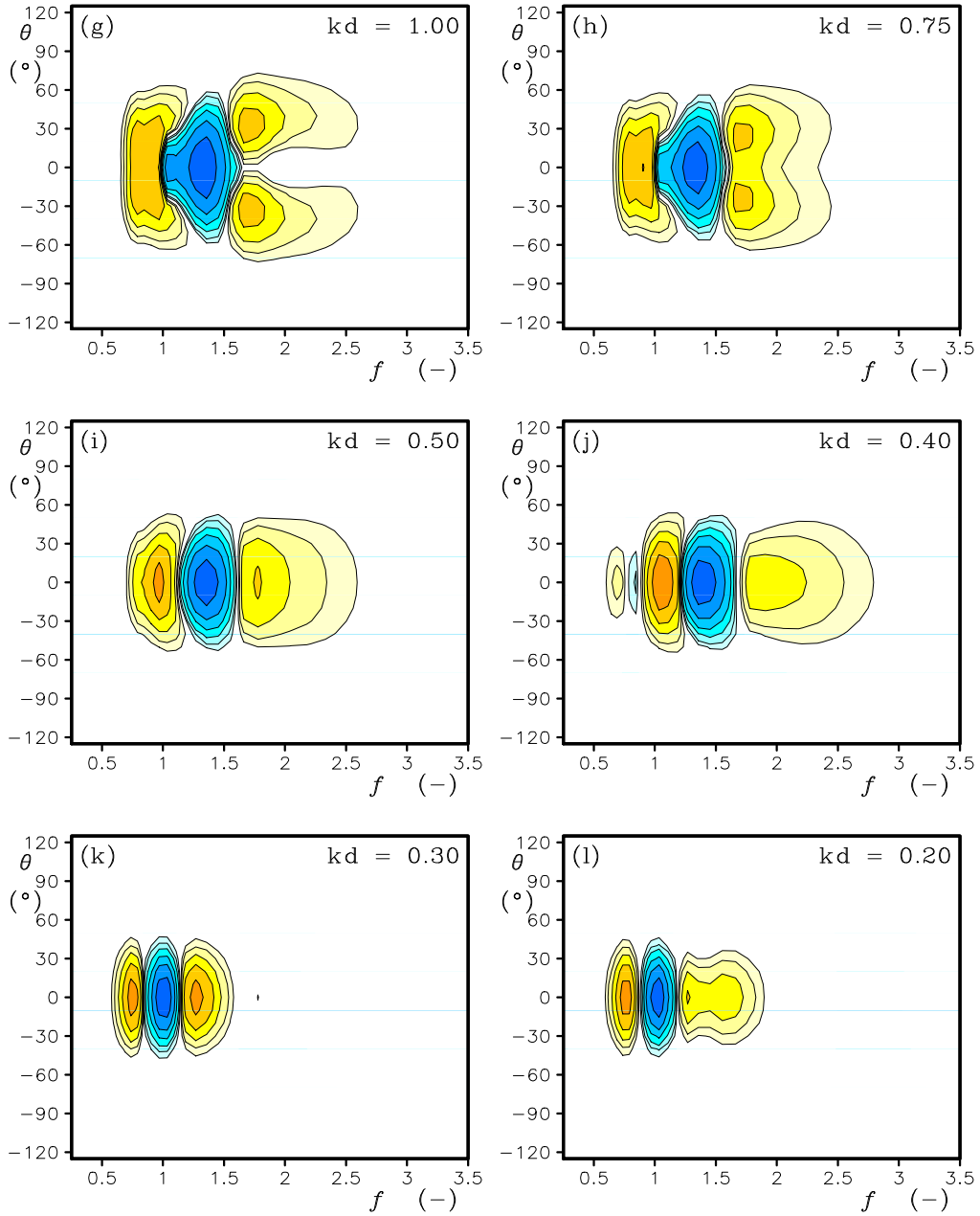
Fig. 2.22 : Like Fig. 2.21, scaled with maximum interaction for the DIA at each relative depth.

Table 2.3: *Quadruplet layout used in the MDIA scaling test. Quadruplet layout defined by two parameters* (λ, μ). *Left columns correspond to scaling from Eq. (2.101). Right columns correspond to scaling from Eq. (2.114) with* $n = -3.5$.

quad.	λ	μ	C	λ	μ	C
1	0.064	0.050	$3.92\ 10^8$	0.078	0.050	$4.69\ 10^6$
2	0.175	0.100	$1.21\ 10^7$	0.350	0.100	$1.83\ 10^6$
3	0.300	0.150	$1.62\ 10^7$	0.397	0.150	$1.38\ 10^6$
4	0.403	0.200	$8.51\ 10^6$	0.500	0.200	$8.67\ 10^6$

discussed above, there is no need to test this MDIA with the traditional scaled deep-water approach from the original DIA. The first case considered will be the fully expanded (M)DIA based on Eq. (2.100) with the parametric scaling from Eq. (2.101) with $m = 0$. Results for this MDIA are presented in Figs. 2.23 and 2.24. Consistent with the corresponding results for the single component DIA (Fig. 2.17), this MDIA shows good scaling behavior for $kd \geq 1$. For $kd \geq 0.5$ reasonable scaling behavior is obtained, as well as a transition to of more one-dimensional signature of the interactions. For smaller depths, the more one-dimensional signature remains, but the magnitude of the interactions is severely underestimated.

Alternately, the asymptotic scaling for shallow water from Eq. (2.114) can be used. Rather than using this scaling with the deep-water optimized quadruplets, this approach can be used with quadruplets specifically optimized for shallow water. Such quadruplets, moderately optimized for $kd = 0.20$ with $n = -3.5$, are presented in the right columns of Table 2.3. The corresponding interactions for the more shallow relative depths are presented in Fig. 2.25. The corresponding interactions show excellent scaling behavior for $kd \leq 0.5$, and a severe underestimation for deeper water, consistent with the corresponding results for the single DIA. Several features of the exact interactions are well represented, including the one-dimensional character, and the broadening of the interactions near $kd = 0.5$. In general the interactions are too narrow in directional space.

Figure 2.26 shows the interactions for the scaling function of Eq. (2.115) with $m = 4$ and $n = -3.5$, which combines deep and shallow scaling and quadruplets. This approach indeed provides good scaling behavior across depths, but with similar shortcomings in shapes as seen in the individual components.

The final approach to be tested is the scaling function (2.102), which includes the actual interaction coefficient G from Eqs. (2.86) through (2.89). The results of this approach are presented in Figs. 2.27 and 2.28. This MDIA is based on the deep-water optimized quadruplet on the left side of Table 2.3. This approach
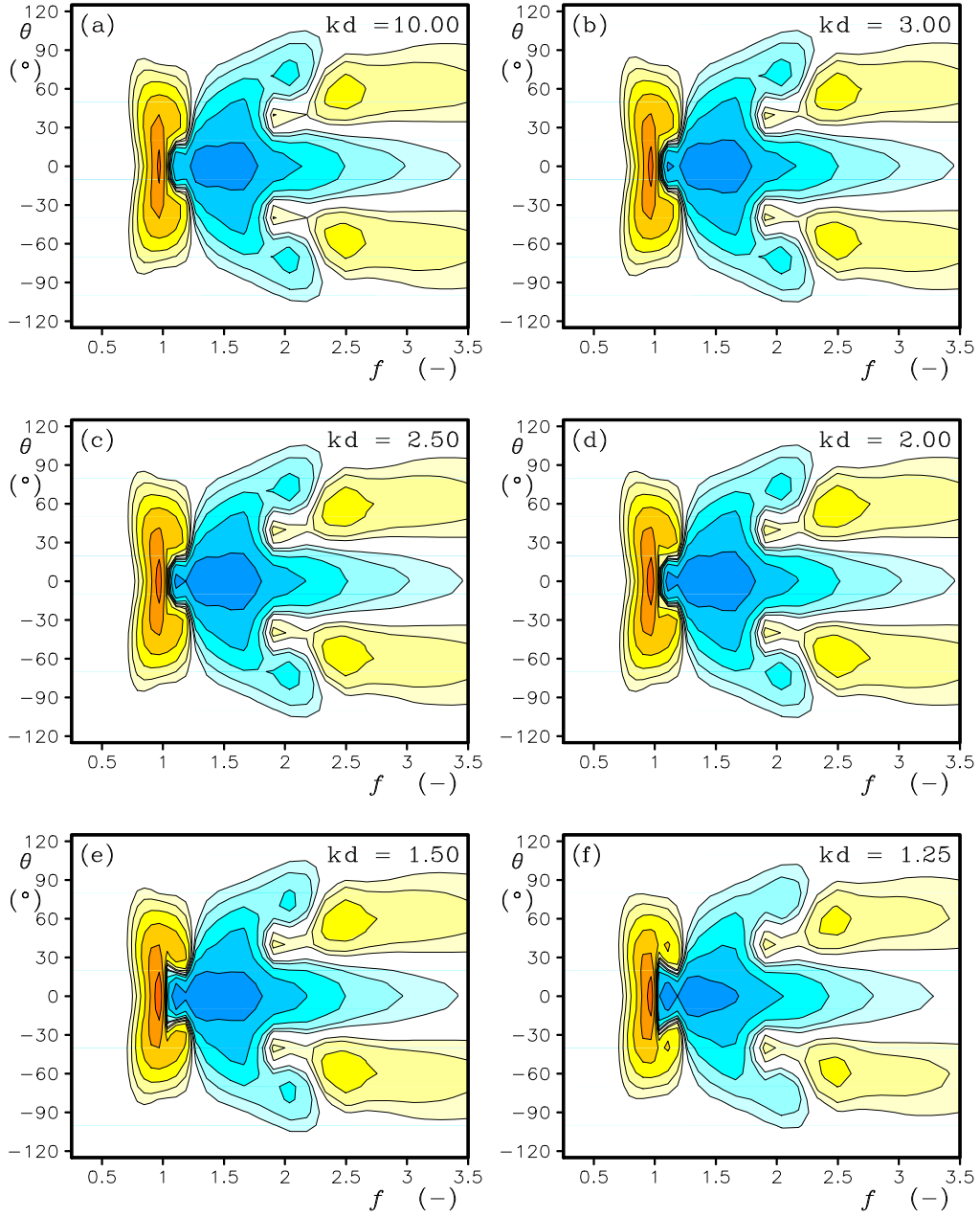
Fig. 2.23 : Results for an MDIA based on Eq. (2.100) and (2.101) with $m = 4$ for the corresponding quadruplets from Table 2.3. Each panel scaled as in Fig. 2.11.
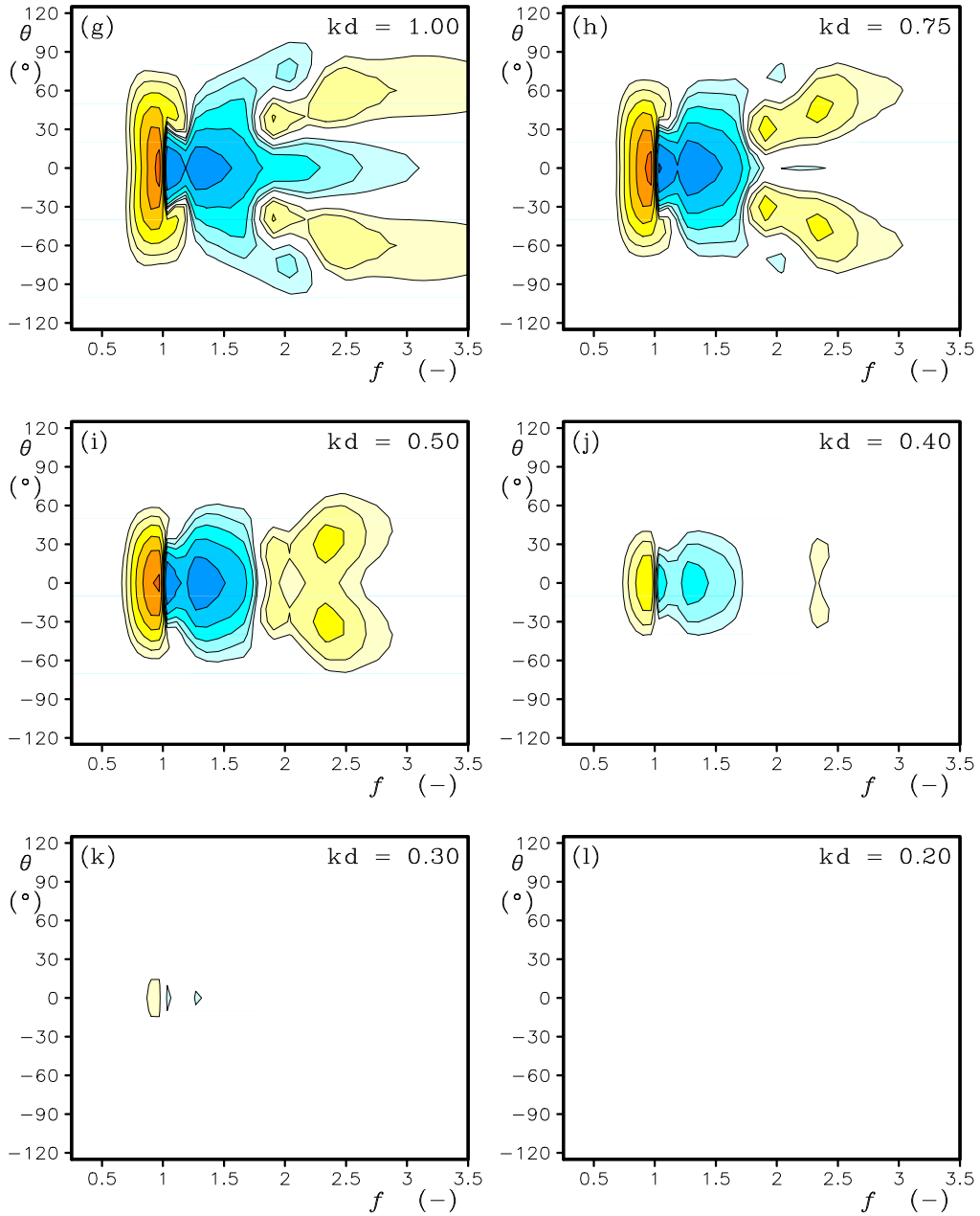
Figure 2.23 continued.

60
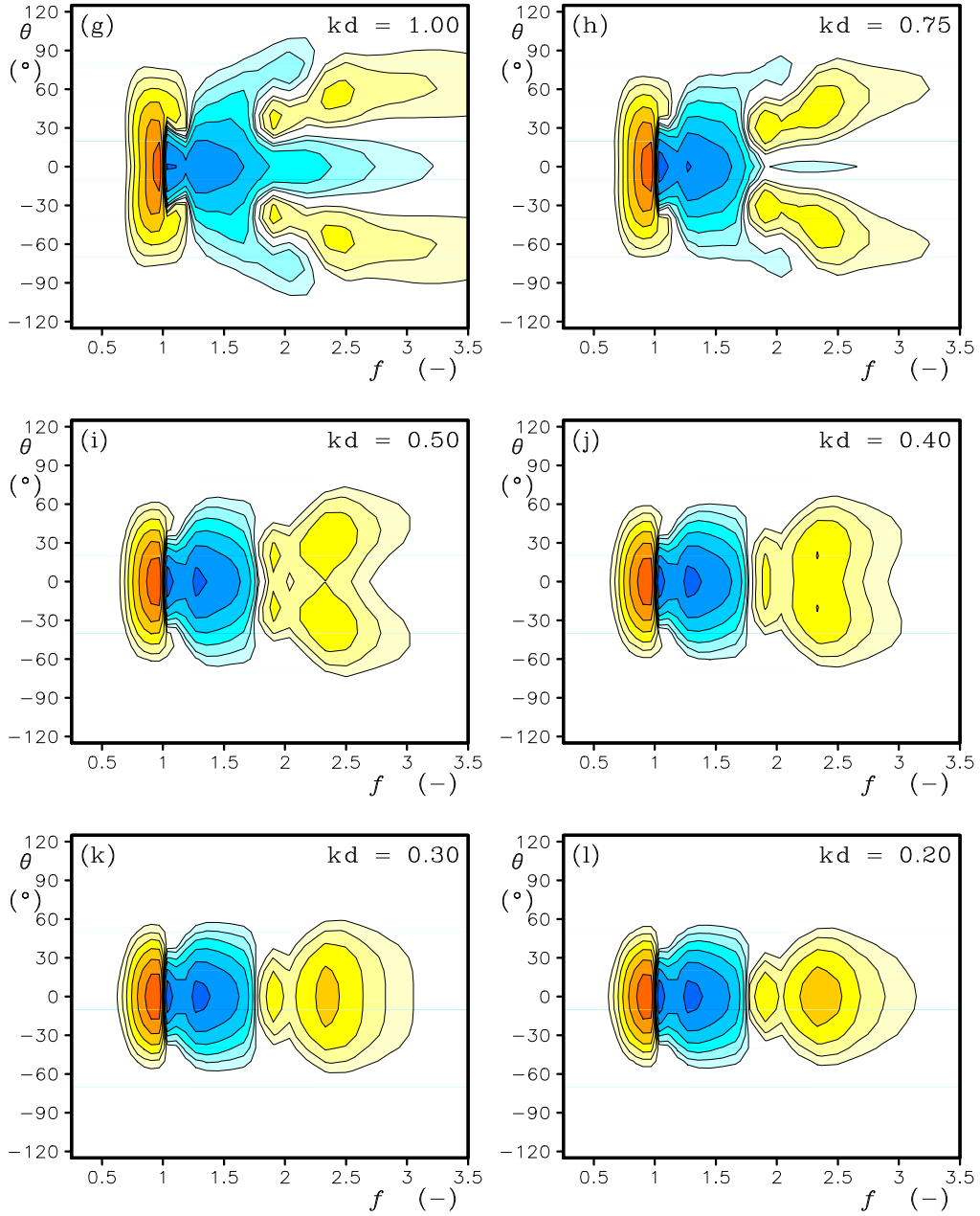
Fig. 2.24 : Like Fig. 2.23 with each panel scaled with its own absolute maximum value.
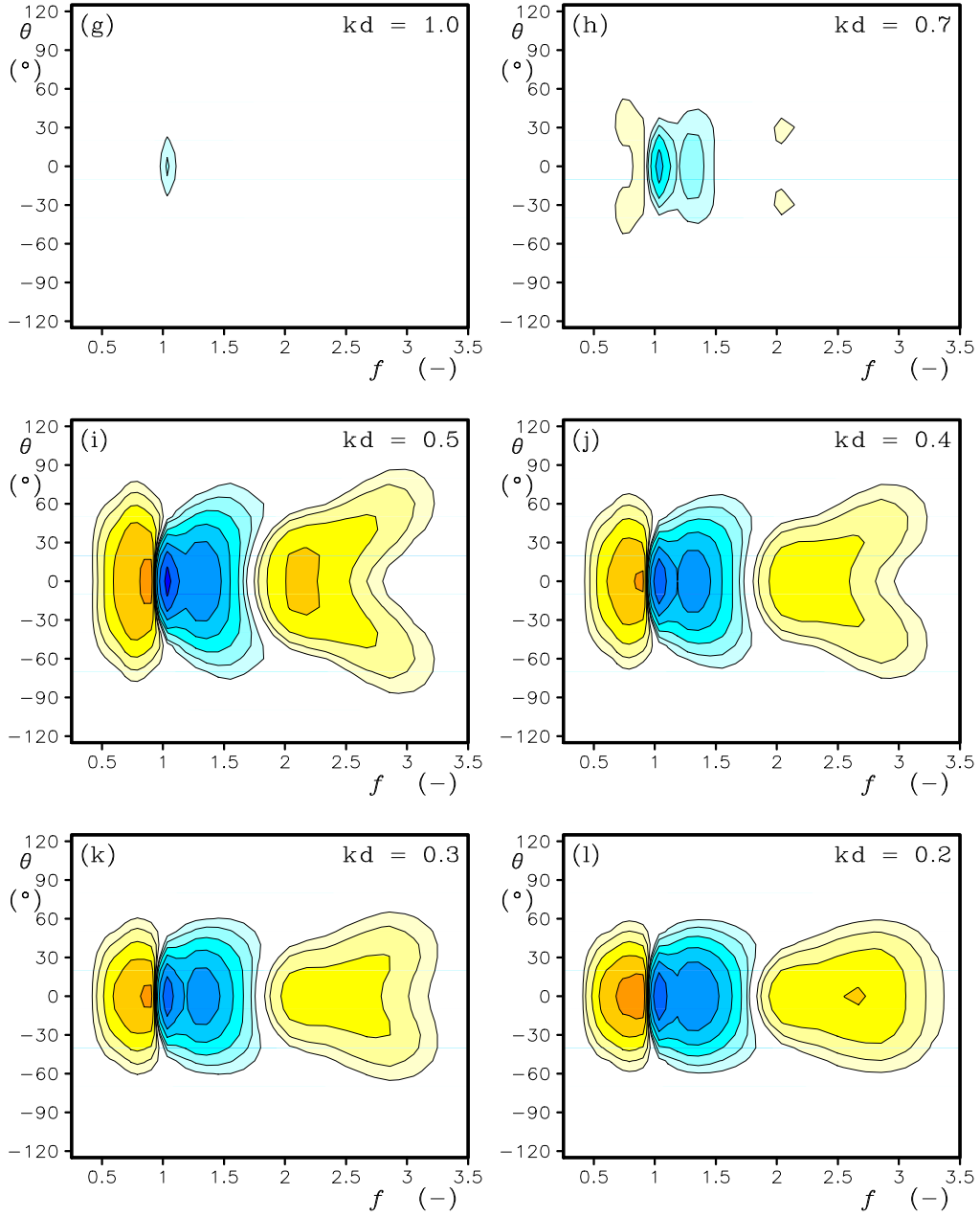
Fig. 2.25 : Results for an MDIA based on Eq. (2.100) and (2.114) with $n = -3.5$ for the corresponding quadruplets from Table 2.3. Each panel scaled as in Fig. 2.11.

62
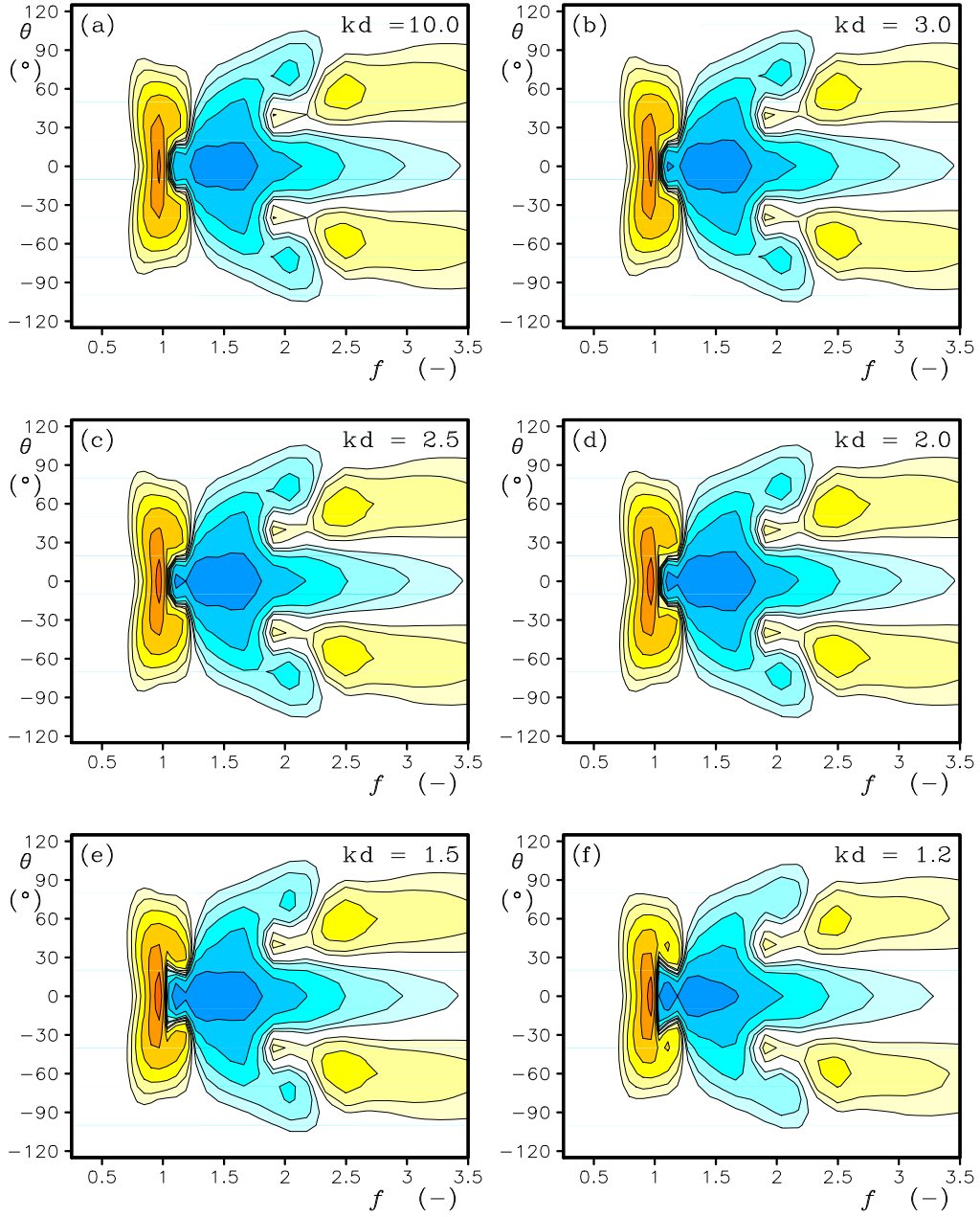
Fig. 2.26 : Results for an MDIA based on Eq. (2.100) and (2.115) with $m = 4$
and $n = -3.5$ for the quadruplets from Table 2.3. Each panel scaled as
in Fig. 2.11.

63
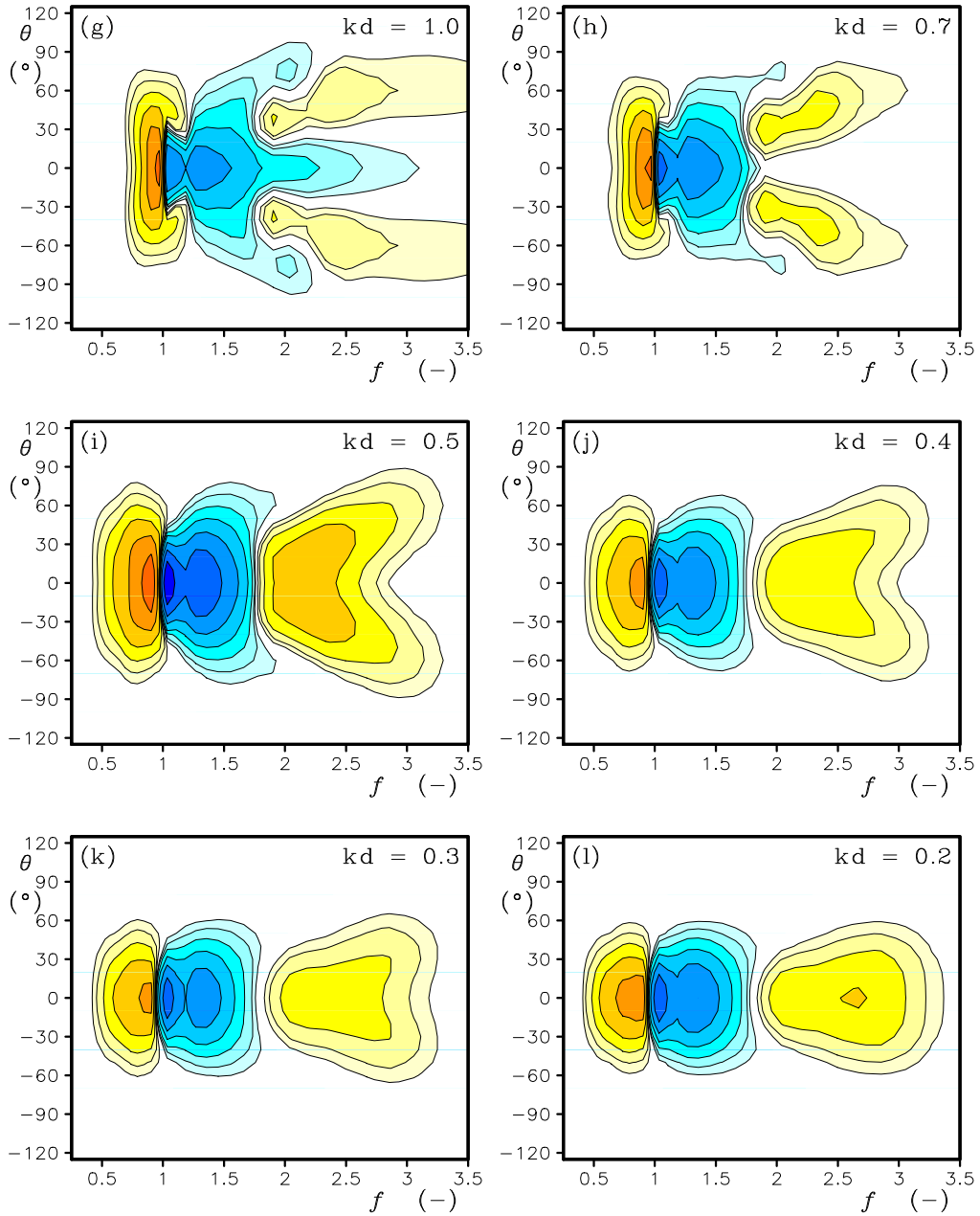
Figure 2.26 continued.

64
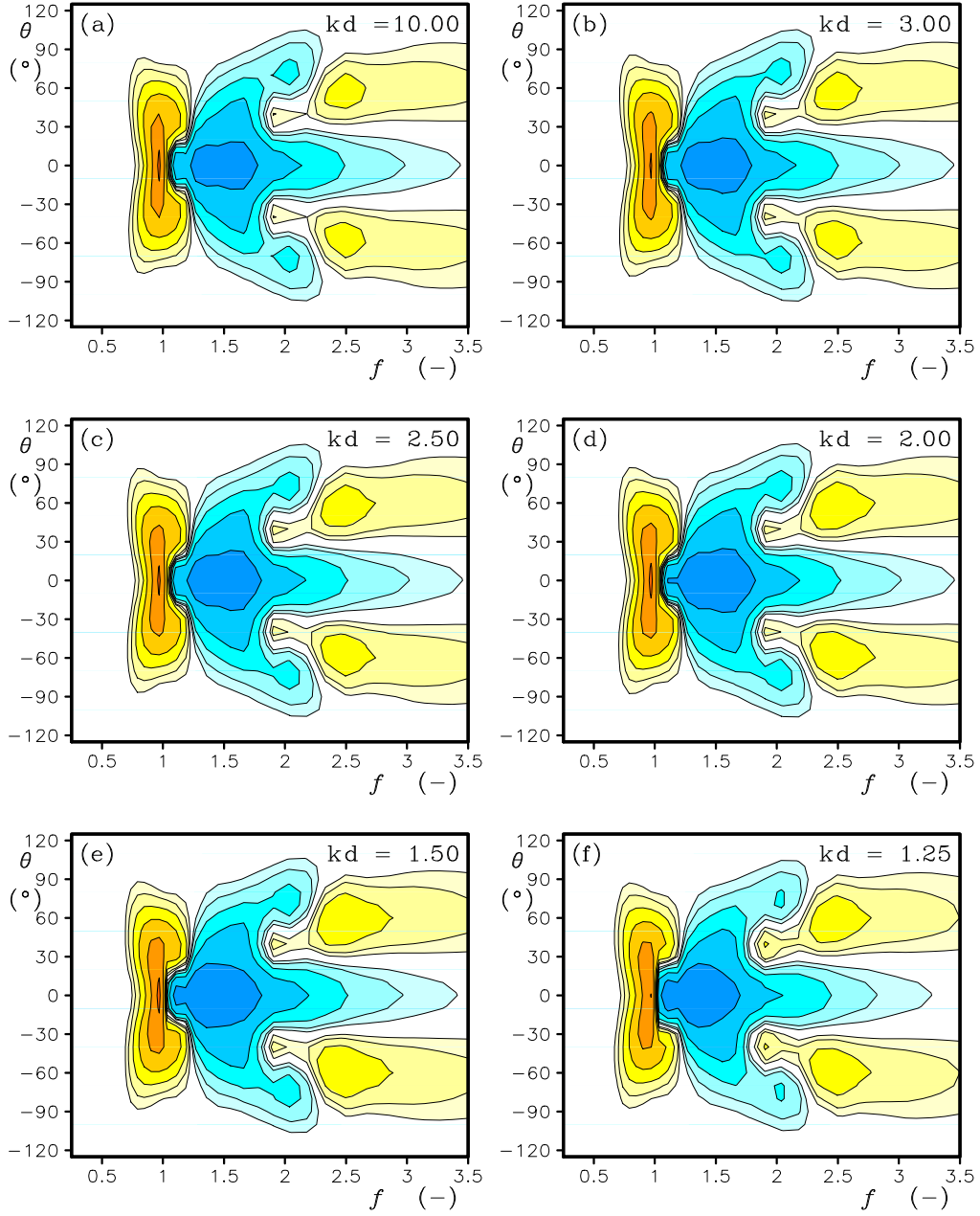
Fig. 2.27 : Results for an MDIA based on Eq. (2.100) and (2.102) for the
quadruplets from Table 2.3. Each panel scaled as in Fig. 2.11.

65
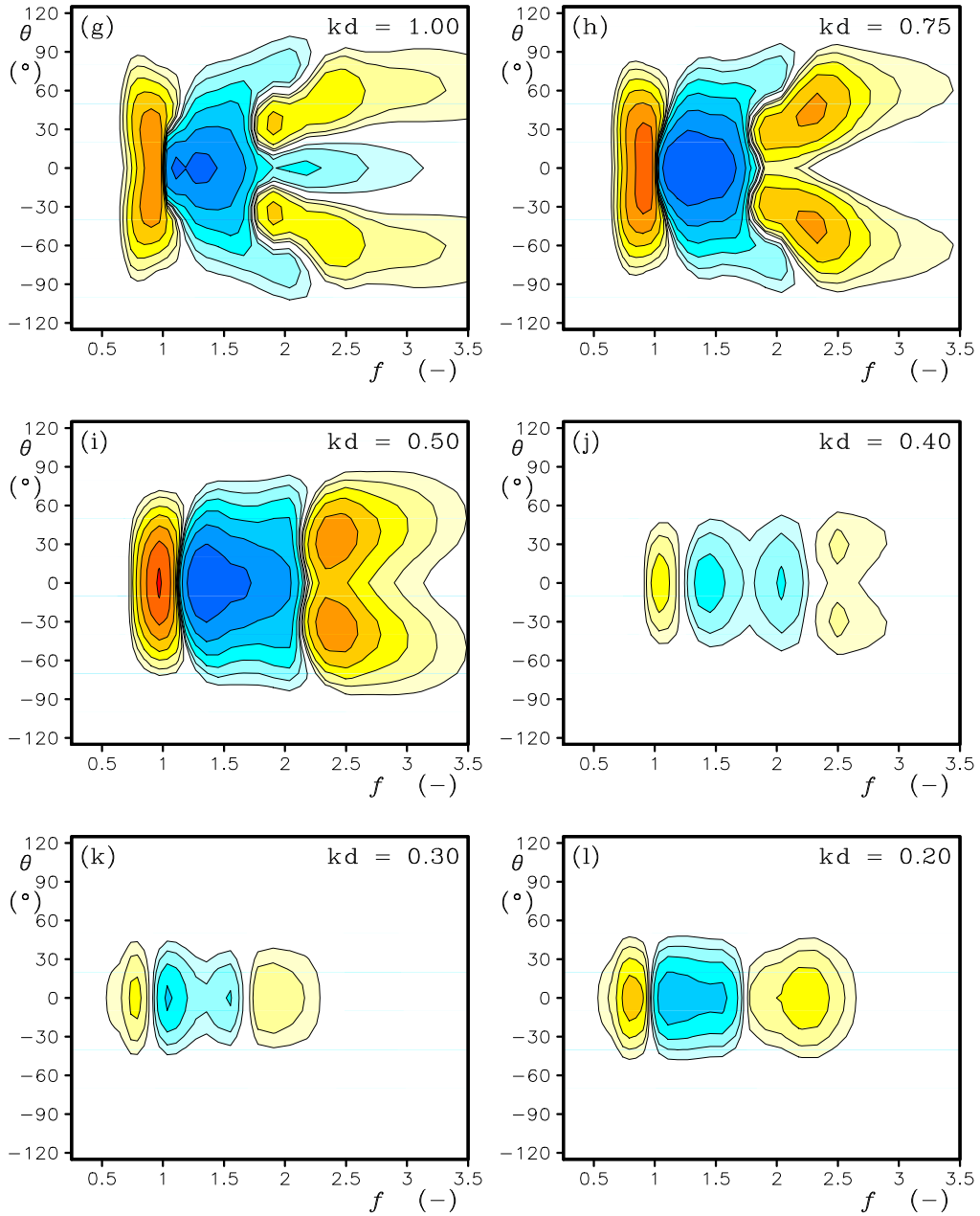
Figure 2.27 continued.
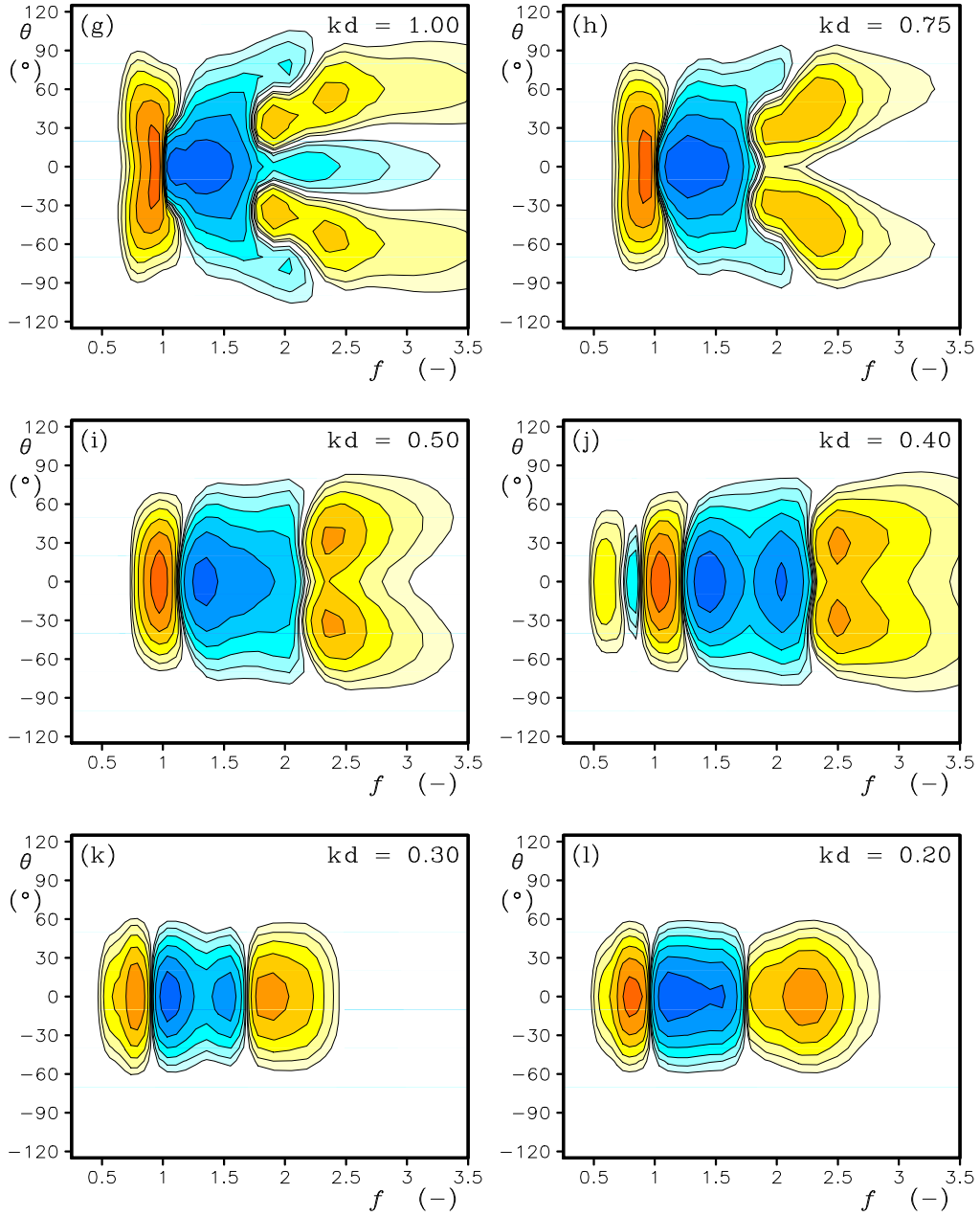
Fig. 2.28 : Like Fig. 2.27 with each panel scaled with its own absolute maximum value.

provides decent scaling behavior across depths without further modifications. Interactions are moderately overestimated for transition depths, and somewhat underestimated for the most shallow water depths. The scaling behavior may be improved further by adding a simple rescaling function based on kd, as in the original DIA. Unlike in the original DIA, this function represents a minor correction to scaling behavior. In the former case, it represented all scaling behavior.

The major shortcoming of MDIAs based on the scaling functions (2.115) or (2.102) is that the shape of the spectra is too narrow in the shallowest water (compare the WRT interactions in Fig. 2.11 with MDIAs in Figs. 2.26 through 2.28). A reason for this may be found in the evolution of the one and two parameter quadruplet layout with depth as identified in Fig. 2.2. Both the one parameter quadruplet layout (λ) and the two-parameter quadruplet layout (λ, μ) show a reduction of the internal quadruplet layout with reduced depth. Among others, this implies that some viable quadruplet layouts for shallow water can never be achieved, and that by definition, the quadruplet becomes more one-dimensional in shallow water. For the three parameter quadruplet layout $(\lambda, \mu, \Delta\theta)$, the behavior is (or can be) significantly different. The natural extension to restricted water depths is to keep $(\lambda, \mu, \Delta\theta)$ independent of the relative water depth. Note that this only keeps the angle between $\boldsymbol{k}_1$ and $\boldsymbol{k}_2$ constant. A more advanced method would be to allow particularly $\Delta\theta$ to become a function of the depth. In the present context it is most relevant to address the systematically different behavior induced by keeping the quadruplet parameters, in particular $\Delta\theta$, unchanged. A simple way to achieve this is to compute deep-water $\Delta\theta$ equivalent to the two-parameter quadruplet from the left column of Table 2.3, to extend these two-parameter quadruplets to three-parameter quadruplets. Hence, deep-water behavior should be similar or identical, but shallow water behavior is bound to change.

Figures 2.29 and 2.30 present results obtained with this three parameter quadruplet definition. Results in deep water ares somewhat different from the results for the two parameter quadruplet layout, because of different sampling of the spectral space (the two parameter layout still uses the sampling techniques from Part 2). Considering the deep water differences between the two- and three-parameter quadruplet definitions, results for shallow water are remarkably similar. The three parameter quadruplet shows slightly poorer scaling characteristics in extremely shallow water, as well as even directionally narrower interactions. Hence, the tree parameter quadruplet definition does not seem to improve the behavior in shallow water.
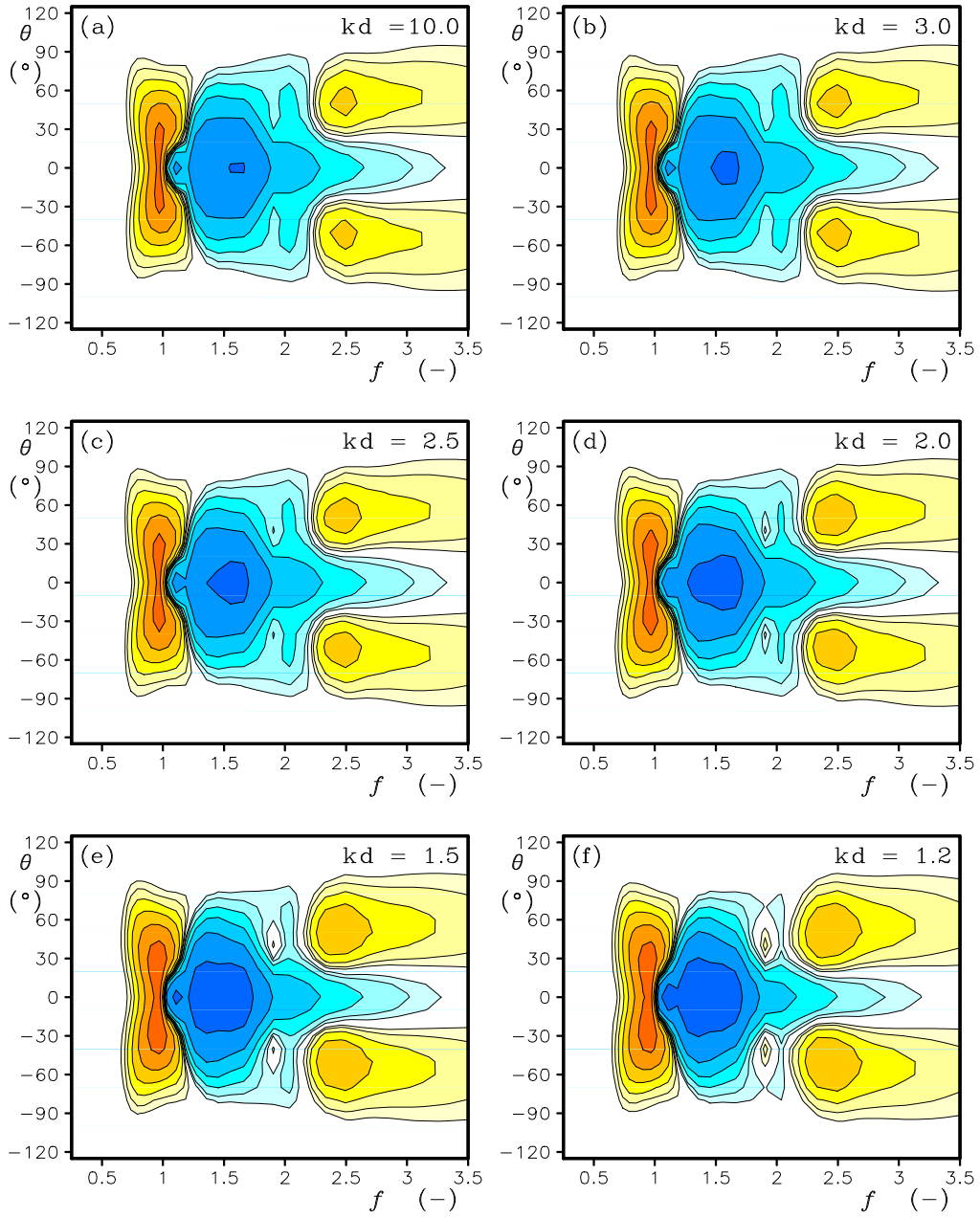
Fig. 2.29 : Results for an MDIA based on Eq. (2.100) and (2.102) for the
quadruplets from Table 2.3, assuming a three-parameter quadruplet def-
inition with $\Delta\theta$ obtained from the two-parameter quadruplet definition
in deep water. Each panel scaled as in Fig. 2.11.
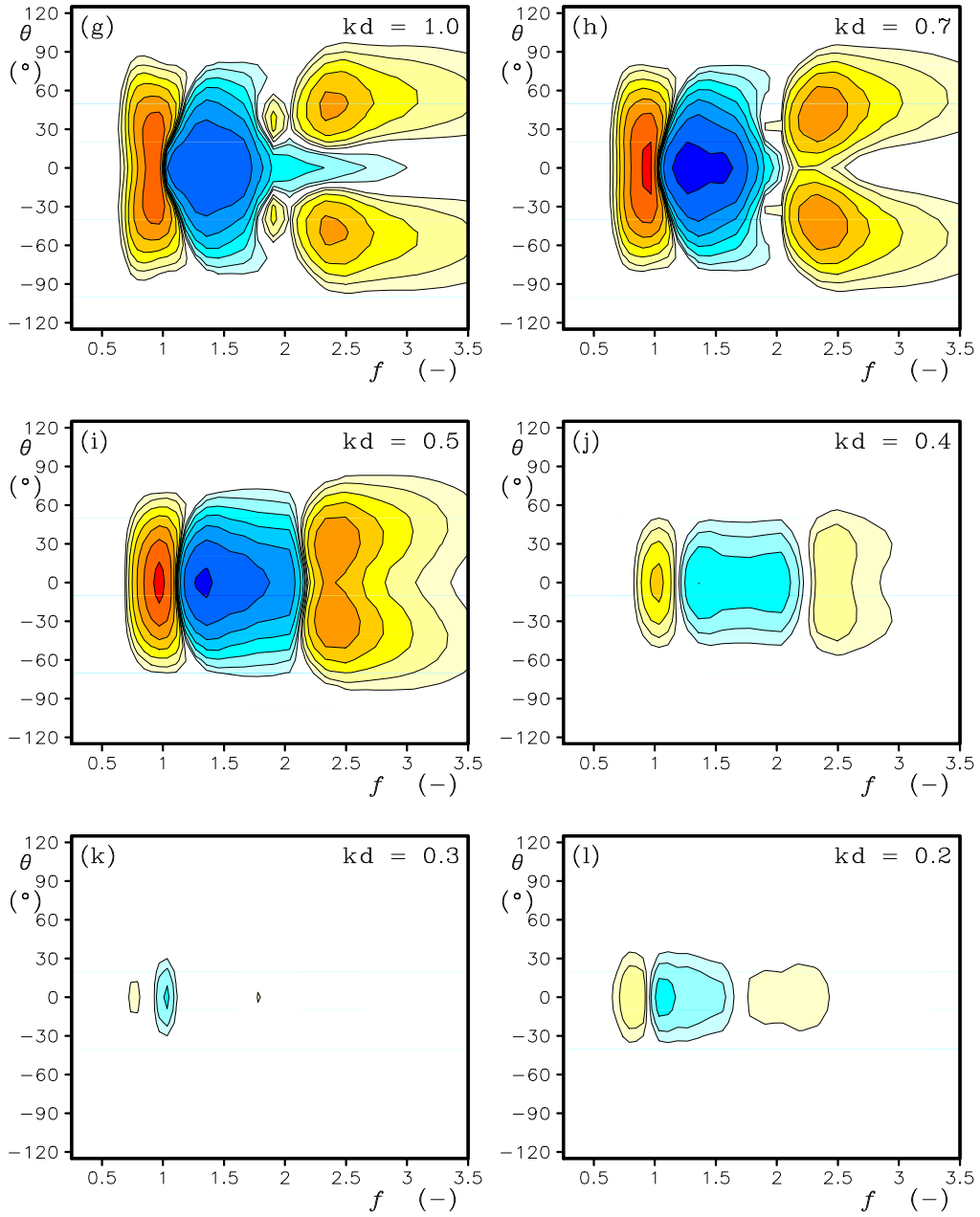
Figure 2.29 continued.
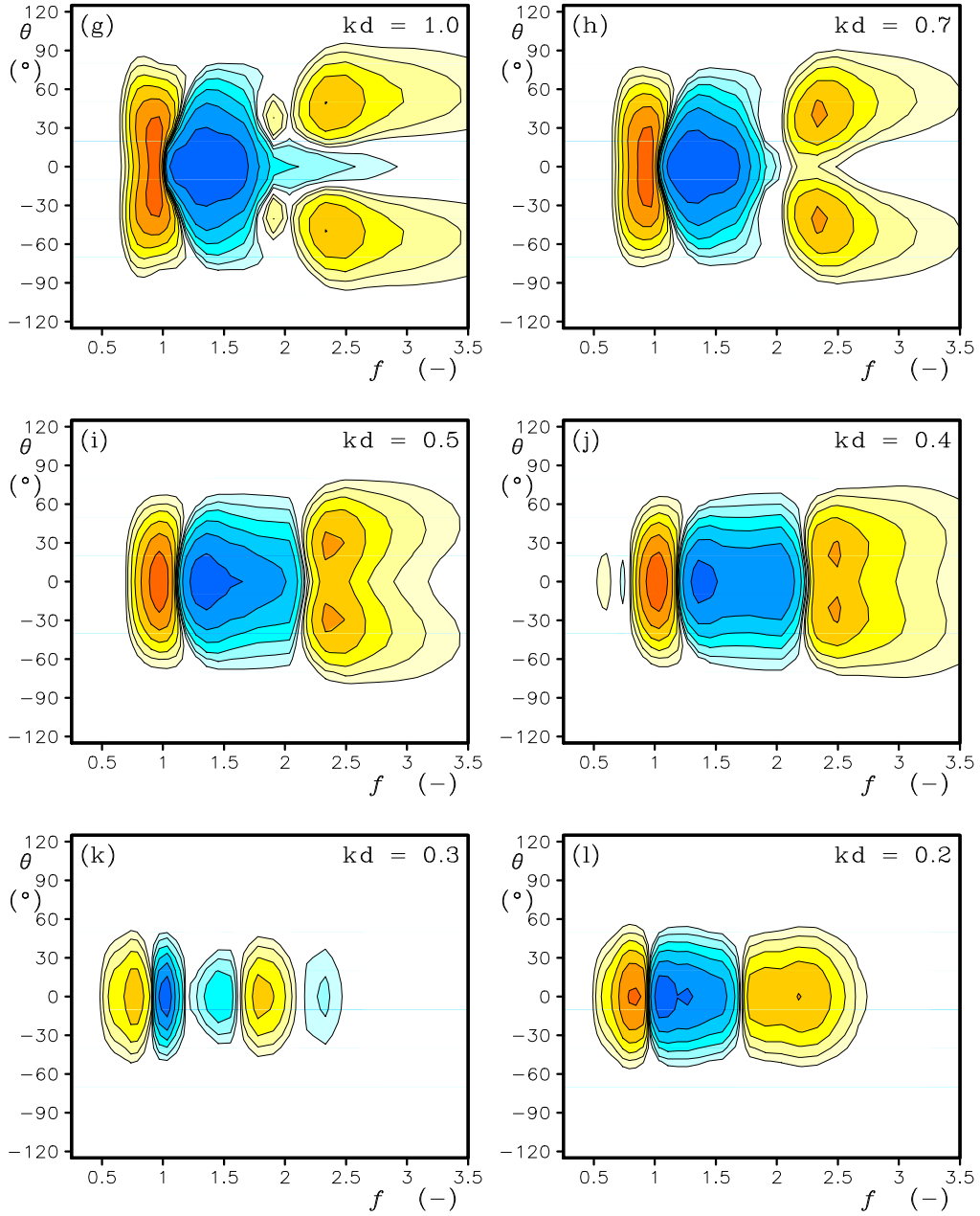
Fig. 2.30 : Like Fig. 2.29 with each panel scaled with its own absolute maximum value.

2.8 Conclusions

The simple numerical experiments performed here with the DIA and MDIA in restricted water depths clearly identify the superiority of a properly derived shallow-water DIA over the conventional re-scaled deep-water DIA. Applying the proper shallow water dispersion relation in the determination of the layout of the quadruplet(s) is essential to assure that the interactions conserve wave momentum. If the proper shallow water quadruplet layout is used, the shape of the interactions becomes highly unrealistic, unless the proper shallow water product term and scaling functions not associated with the coupling coefficient are also introduced [Eq. (2.100)]. The latter modification in fact produces a much more realistic 'one-dimensional' signature of the interactions in extremely shallow water. However, the scaling behavior of such interactions in shallow water is highly inadequate, with the strength of the interaction underestimated by several orders of magnitude. The argument could be made that this is a positive attribute when applying such a DIA in an operational model; if the assumption is made that the four-wave interactions are not the dominant process in shallow water, then a parameterization that naturally 'filters out' these interactions in extremely shallow water in fact may be acceptable or even desirable.

Further improvements can be made by considering appropriate scaling functions representing the coupling coefficient G in the DIA. A simple and tentatively robust approach is presented in Eq. (2.101), where the parameter m represents the level at which wavenumbers rather than frequencies should be considered in the scaling function. Tentatively, the value of m should range from 0 to 8, with values of $m \approx 4$ suggested by assessment of the behavior of G in Figs. 2.8 and 2.9. Increasing m indeed increases the range of proper scaling if the DIA to shallow water, and into the transition range from weak to strong interactions around $kd \approx 0.5$. This approach, however, cannot produce the asymptotic scaling behavior for extremely shallow water. To produce such scaling behavior, a proper shallow water scaling function needs to be introduced [Eq. (2.114)]. This function with $n \approx -5.0$ indeed gives proper asymptotic scaling behavior in extremely shallow water. The 'deep' and 'shallow' scaling functions can be combined into one [Eq. (2.115)], or an MDIA can be constructed with a mixture of quadruplets with both scaling functions to produce acceptable scaling behavior across all depths. Alternately, the full shape of the interaction coefficient G can be retained in the scaling function [Eq. (2.102)], resulting in significantly improved scaling behavior across arbitrary depth. Such an MDIA could tentatively be improved further with a corrective scaling function as a function of the relative depth kd.

It should be noted that the DIA approaches considered here have not been fully optimized. Considering the results from Part 2, such an optimization should be based on holistic model behavior, and it is therefore not sensible to optimize methods presented here in more detail. It is, however, obvious from the present results, that there are ample opportunities to optimize the expanded DIA, in

particular its scaling functions, for arbitrary depths. It is more appropriate to discuss actual techniques, after the discussion of the numerical optimization of the expanded DIA in Section 5. It does remain important to realize that the extremely shallow water conditions are not realistic or the four-wave interactions not locally dominant for practical wave modelings.

This page is intentionally left blank.

3 Diffusion operators

Diffusion operators have been presented as a possible alternative to the DIA by several authors, for instance, Hasselmann et al. (1985), Zakharov and Pushkarev (1999), and Jenkins and Phillips (2001). Although these approaches are cheap, they appear to lack the desired accuracy. In the context of the present study diffusion operators may nevertheless be useful to improve the economy of the resulting algorithm. In particular for higher frequencies, time scales of spectral evolution are short, requiring small numerical time steps for accuracy and stability. Applying selective smoothing (diffusion) in this spectral range may well improve numerical model integration economy (by allowing for larger time steps), while proper optimization may well assure that the accuracy of model results does not suffer from such an approach.

The traditional one-dimensional diffusion equation for an arbitrary parameter A evolving in time t and space x is given as

$$\frac{\partial A}{\partial t} - D\frac{\partial^2 A}{\partial x^2} = 0 \quad , \tag{3.1}$$

where D is the diffusion coefficient. In a traditional forward time central space (FTCS) finite difference approach, the numerical solution to this equation becomes

$$A_j^{n+1} = A_j^n + \frac{D\Delta t}{(\Delta x)^2}\left(A_{j-1}^n - 2A_j^n + A_{j+1}^n\right) \quad , \tag{3.2}$$

where j and n are discrete space and time counters, and Δx and Δt are discrete space and time counters, respectively. Stability requires that (e.g., Fletcher, 1988)

$$\mathcal{P} = \frac{D\Delta t}{(\Delta x)^2} < 0.5 \quad , \tag{3.3}$$

where $\mathcal{P}$ is the Peclet number. Equation (3.2) can also be interpreted as a smoothing algorithm. If the diffusion coefficient D varies in space, a conservative version of Eq. (3.2) can be obtained if the algorithm is implemented as a redistribution rather than averaging algorithm. For the grid point j, the parameter value A contributes to this grid point and its neighbors as

$$\begin{pmatrix} \delta A_{j+1} \\ \delta A_j \\ \delta A_{j-1} \end{pmatrix}^{n+1} = A_j^n \begin{pmatrix} 0 \\ 1 \\ 0 \end{pmatrix} + A_j^n \mathcal{P} \begin{pmatrix} 1 \\ -2 \\ 1 \end{pmatrix} \quad , \tag{3.4}$$

where the first term on the right represents the unchanged state, and the second term represent the 'source term' for smoothing. Such an equation is very similar to the local contributions of the DIA with a traditional one-parameter quadruplet
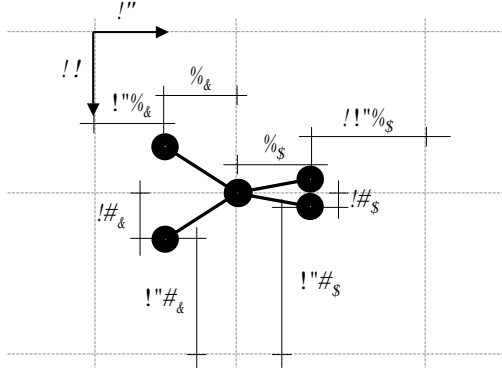
Fig. 3.1 : *Small-scale one-parameter quadruplet inside a nine-point grid sten-cil in the spectral grid, with definition of relative distances in the spectral grid. Central component of quadruplet coincides with central grid point in stencil.*

definition. Considering that in this approach the first two components of the quadruplet are identical, and that component 3 has a larger frequency, Eq. (2.83) can be rearranged as

$$
\begin{pmatrix} \delta s_{nl,3} \\ \delta s_{nl,1} \\ \delta s_{nl,4} \end{pmatrix} = \frac{C'}{2^2(2\pi)^{10}} \, g^{-4} f^{11} P_{1234} \begin{pmatrix} 1 \\ -2 \\ 1 \end{pmatrix} \; . \tag{3.5}
$$

Hence, the traditional DIA can be considered as a diffusion operator applied in the direction of the locus in spectral space given by the resonance conditions, and with a discrete step size defined by the quadruplet parameter λ. Note that the analogy between the DIA and a local diffusion operator is solely due to the choice of the quadruplet layout, and is not reproduced for more complex quadruplet layouts. This may well explain the inherent stability of the traditional DIA, and why this stability is not shared by DIAs with more complex quadruplet layouts.

Whether or not the DIA as described in Eq. (3.5) acts as a true diffusion operator in the discretized spectral space depends on the spatial scale of the quadruplet in spectral space as defined by λ, relative to the discrete spectral increments used to discretize this space. If $|f_3 - f_1| > \Delta f$ (and for similar directional considerations), individual contributions of the DIA are resolved by the discrete spectral space, and the direct link between Eqs. (3.4) and (3.5) is lost as components of the quadruplet do not correspond to adjacent grid points in spectral space. If, however, λ is selected sufficiently small so that the components of the quadruplet fall within three adjacent discrete grids points in the frequency and direction spaces, an equivalence between Eqs. (3.4) and (3.5) is established.

Figure 3.1 shows the layout of small scale quadruplet inside a nine-point

stencil of grid points in spectral space. The central component of the quadruplet $[f_1, \theta_1) = (f_2, \theta_2)]$ is collocated with the central grid point in the discrete spectral space, and a_3, a_4, b_3 and b_4 are normalized distances in the nine-point stencil (i.e., normalized with distances between the corresponding spectral grid lines). If ΔF_1 and ΔF_2 are the discrete spectral changes for the two mirror image quadruplets, the changes of spectral density in the nine-point stencil become

$$\delta F = M_1 \Delta F_1 + M_2 \Delta F_2 \quad , \tag{3.6}$$

where M_1 and M_2 are 3×3 matrices with rows representing discrete directions and columns representing discrete frequencies. With the relative distances as defined in Fig. 3.1, these matrices become

$$M_1 = \begin{pmatrix} a_4 b_4 & (1-a_4) b_4 & 0 \\ (1-a_4) b_4 & M_c & (1-a_3) b_3 \\ 0 & (1-a_3) b_3 & a_3 b_3 \end{pmatrix} \quad , \tag{3.7}$$

$$M_2 = \begin{pmatrix} 0 & (1-a_3) b_3 & a_3 b_3 \\ (1-a_4) b_4 & M_c & (1-a_3) b_3 \\ a_4 b_4 & (1-a_4) b_4 & 0 \end{pmatrix} \quad , \tag{3.8}$$

$$M_c = a_3 b_3 + a_4 b_4 - a_3 - a_4 - b_3 - b_4 \quad . \tag{3.9}$$

The distribution scheme can be simplified for interactions on scales that are much smaller than the discretization of spectral space, where $a_3, a_4, b_3, b_4 \ll 1$. In such conditions Eqs (3.7) and (3.8) become

$$M_1 \approx \begin{pmatrix} 0 & b_4 & 0 \\ b_4 & -a_3 - a_4 - b_3 - b_4 & b_3 \\ 0 & b_3 & 0 \end{pmatrix} \quad , \tag{3.10}$$

$$M_2 \approx \begin{pmatrix} 0 & b_3 & 0 \\ b_4 & -a_3 - a_4 - b_3 - b_4 & b_3 \\ 0 & b_4 & 0 \end{pmatrix} \quad , \tag{3.11}$$

and the corresponding redistribution of spectral energy closely resembles the two-dimensional version of the diffusion equation (3.4), which in turn closely corresponds to the simple diffusion equation suggested by Jenkins and Phillips (2001). Note that this diffusion equation is alway having main axes lined up with the discrete grid axes.

If the quadruplet falls within the nine-point grid stencil but with relative distances a_3, a_4, b_3 and b_4 not much smaller than 1, M_1 and M_2 retain their diagonal structures, and the orientation of the quadruplet in Fig. 3.1 become effective (non-orthogonal) axes of a diffusion or smoothing operator, with the ratio of ΔF_1 and ΔF_2 determining the actual shape of the smoother within the stencil. To address the evolution of the shape of the stencil a little more, consider

the case with $\Delta F_1 = \Delta F_2$ and with $a_3 = a_4 = b_3 = b_4$. For a, $b = \frac{1}{2}$, $\frac{2}{3}$ and 1, the shape of the distribution stencil becomes

$$\begin{pmatrix} 1 & 2 & 1 \\ 2 & -12 & 2 \\ 1 & 2 & 1 \end{pmatrix} \ , \quad \begin{pmatrix} 1 & 1 & 1 \\ 1 & -8 & 1 \\ 1 & 1 & 1 \end{pmatrix} \ , \quad \begin{pmatrix} 1 & 0 & 1 \\ 0 & -4 & 0 \\ 1 & 0 & 1 \end{pmatrix} \ , \qquad (3.12)$$

respectively. For a, b increasing from 0 to $\frac{1}{2}$ the smoother evolves from operating along grid axes only to becoming a two-dimensional smoother in spectral space with weights decreasing with the distance to the central point of the smoother. For further increasing a and b larger weights fall upon the corners of the nine-point stencil, evolving toward a quadruplet redistribution that becomes resolved by the discrete spectral grid. From a practical perspective, it therefore appears required that $a, b < 0.5$ for a quadruplet to become the basis of a diffusion or smoothing algorithm.

Note that the basic conservation properties of this smoother are all encapsulated in the detailed balance version of the interaction and DIA formulations [e.g., Eq. 2.2] as already noted by Webb (1978) and in Section 2.2; energy and action are conserved as long as the components of the quadruplet satisfy the resonance conditions for frequencies, and momentum is conserved if wavenumber resonance conditions are also met. Furthermore, a logarithmic discretization of frequency space is implicit to diffusion character of the DIA equations. Thus, a diffusion operator with the proper conservation properties for nonlinear interactions can be constructed by a) redistributing energy over a quadruplet as in the original DIA, b) having a, $b \leq 1$ in Fig. 3.1, and by having a and b based on the full resonance conditions by using the one-parameter quadruplet definition based on λ only. Thus, a simple diffusion operator similar to Jenkins and Phillips (2001) can be constructed without any further derivations. It also suggests that such an approach is representative only for interaction scales that are not resolved by the discrete spectral grid.

A consequence of this behavior is that a valid (in terms of conservation properties) smoother can be constructed *independent of the actual computation of* ΔF_1 *and* ΔF_2. There are two systematically different approaches to estimating these increments; consider it as a pure numerical smoother, or consider it as an attempt to model unresolved stabilizing interactions in the tail of the spectrum. Both approaches will be considered here.

If a purely numerical smoother is to be considered, the strength of the smoother is easily controlled if it is defined by the discrete change of the spectral density at the central point of the grid stencil ΔF_c, and if the distribution matrices are normalized consistently as in

$$\delta F = (M_1 + M_2) M_c^{-1} \Delta F_c \ . \qquad (3.13)$$

This change can be normalized with the the corresponding spectral density F_c, $\Delta\tilde{F}_c = \Delta F_c/F_c$. Note that the stability criterion (3.3) then tentatively corresponds to

$$\Delta\tilde{F}_c < \Delta\tilde{F}_{c,lim} \approx 0.5 \quad . \tag{3.14}$$

The strength of the smoother can then be controlled by a user-supplied maximum value of the normalized change of the central spectral density $\Delta\tilde{F}_{c,\max} \leq \Delta\tilde{F}_{c,lim}$. Furthermore, the smoother is needed only for the high-frequency flank of the spectrum. This can be achieved by introducing a filter function $\Phi(f)$, taken from the JONSWAP spectral definition.

$$\Phi(f) = \exp\left[-c_1\left(\frac{f}{c_2 f_p}\right)^{-c_3}\right] \quad , \tag{3.15}$$

where f_p is the peak frequency of the (wind sea part of the) spectrum. In the original JONSWAP expression, $c_1 = 1.25$ and $c_3 = 4$. The constant c_2 is added to allow for a shift of the filter from the spectral peak (as in JONSWAP where $c_2 = 1$) to higher frequencies ($c_2 > 1$).

Furthermore, the smoother at least needs to be independent of the numerical time step, or ideally to be numerically convergent. The first requirement demands that the strength of the filter for small time steps scales with the time step, similar to the time step scaling of the model physics. To achieve this a nondimensional time step $\Delta\tilde{t}$ needs to be introduced. Typical ways to generate a nondimensional time can be taken from, e.g., Hersbach and Janssen (1999), and include a normalizing time step (Δt_n) or a representative frequency (f_r)

$$\Delta\tilde{t} \propto \Delta t \, \Delta t_n^{-1} \quad , \quad \Delta\tilde{t} \propto f_r \, \Delta t \quad ,$$

Finally considering that $\tilde{F}_{c,lim}$ should scale with $\Delta\tilde{t}$ and should be an asymptotic constant for large $\Delta\tilde{t}$,

$$\Psi(\Delta\tilde{t}) = \tanh\Delta\tilde{t} \tag{3.16}$$

and a relatively simple numerical filter can be defined as

$$\Delta\tilde{F}_c = \Phi(f)\,\Psi(\Delta\tilde{t})\,\Delta\tilde{F}_{c,\max} \quad , \tag{3.17}$$

Thus, the filter is defined by five parameters; λ defining the quadruplet geometry, $\Delta\tilde{F}_{c,\max}$ defining the filter strength, and c_1 through c_3 limiting the filter to high frequencies only. Furthermore, a definition of the nondimensional time step needs to be developed further. Ideally, these parameters are optimized holistically together with the other parameters of the MDIA as in Part 2. Note that for the logarithmic frequency grid (1.8) used here

$$a_3 = a_4 = a_{34} = \frac{\lambda}{X-1} \quad . \tag{3.18}$$

Thus, either a_{34} or λ can be user defined.

A drawback of this filter scheme is that it is non-convergent. Due to the linear dependence on $\Delta \tilde{t}$ the impact of the filter remains in existence for $\Delta t \to 0$. If the filter is non-convergent, it appears more elegant to define it more closely consistent with the nonlinear interactions, possibly as a reduced part of a multiple DIA. Computing the change of spectral energy consistent with the quadruplet strength of the traditional DIA (3.5) with a time step Δt, and filtering the change relative to the peak frequency as in (3.15) the nondimensional spectral change strength $\Delta \tilde{F}_{1,2}$ for the quadruplet becomes

$$\Delta \tilde{F}_{1,2} = -M_c \, \Phi(f) \, \frac{C'}{2(2\pi)^{10}} \, g^{-4} f^{11} \, P_{1234} \, \Delta t \, F^{-1} \quad . \tag{3.19}$$

Note that the factor $-M_c$ represents the fact that the quadruplet is not resolved by the discrete frequency grid, and that hence contributions of changes at F_3 and F_4 are also attributed to the central bin of the smoothing stencil. A user defined maximum filter strength $\Delta \tilde{F}_{\max}$ needs to be filtered with respect to the frequency and distributed over the two quadruplet representations. Equal distribution over maximum changes $\Delta \tilde{F}_{m,1}$ and $\Delta \tilde{F}_{m,2}$ results in

$$\tilde{F}_{m,1} = 0.5 \Delta \tilde{F}_{\max} \Phi(f) \quad , \tilde{F}_{m,2} = 0.5 \Delta \tilde{F}_{\max} \Phi(f) \quad , \tag{3.20}$$

or can be distributed relative to interaction strengths.

$$\Delta \tilde{F}_{m,1} = \frac{|\Delta \tilde{F}_1| \, \Phi(f)}{|\Delta \tilde{F}_1| + |\Delta \tilde{F}_2|}) \quad , \Delta \tilde{F}_{m,2} = \frac{|\Delta \tilde{F}_2| \, \Phi(f)}{|\Delta \tilde{F}_1| + |\Delta \tilde{F}_2|}) \quad . \tag{3.21}$$

With this, the central energy changes corresponding to Eq. (3.17) become

$$\Delta \tilde{F}_{c,1} = \Delta \tilde{F}_{m,1} \tanh \left(\frac{\Delta \tilde{F}_1}{\Delta \tilde{F}_{m,1}} \right) \quad , \quad \Delta \tilde{F}_{c,2} = \Delta \tilde{F}_{m,2} \tanh \left(\frac{\Delta \tilde{F}_2}{\Delta \tilde{F}_{m,2}} \right) \quad . \tag{3.22}$$

Note that $\Delta F_{1,2}1$ can be both negative and positive, describing either anti-diffusion or diffusion, but that both are fully consistent with the previous smoother, Practical applications of this smoother will be discussed in Section 5.2. Note, furthermore, that from Eq. (3.19) a consistent source term can be defined, for which the ensuing equations represent a time integration method fully consistent with a diffusion-based filter.

4   Numerical aspects

Two additional numerical aspects of the nonlinear interactions have not been addressed yet. The first deals with the fact that the discrete spectrum does not cover the entire spectral space; the second is important for time integration of physics in a numerical wave model.

By definition, the discrete description of spectral space contains a minimum and maximum discrete spectral frequency or wavenumber. Because the nonlinear interactions are by definition non-local in spectral space, parts of quadruplets contributing to interactions inside the discrete spectral space reside outside this space. This implies that the discrete frequency or wavenumber space needs to be expanded to encompass all contributing quadruplets in their entirety. This in turn implies the addition of discrete low-frequency grid point in spectra space. For such grid points, absence of spectral energy can be assumed. Furthermore, it implies addition of discrete high-frequency grid points, for which a power law spectral energy distribution is considered, as has been published in many previous papers.

Numerical integration of source terms in WAVEWATCH III is executed in a separate fractional step, that solved the following reduced version of Eq. (1.2)

$$\frac{\partial N(k, \theta)}{\partial t} = S(k, \theta) \quad . \tag{4.1}$$

The numerical solution of this equation employs a semi-implicit method where

$$\Delta N(k, \theta) = \frac{S(k, \theta)\Delta t}{1 - \alpha D(k, \theta)\Delta t} \quad , \tag{4.2}$$

where D represents the diagonal terms of the partial derivative of the nonlinear interactions with respect to the spectrum, $D(k_i, \theta_j) = \partial S(k_i, \theta_j)/\partial N(k_i, \theta_j)$ This method was originally introduced in WAMDIG (1988), using a central scheme with $\alpha = 0.5$. Hargreaves and Annan (1998, 2001) modified this scheme by introducing $\alpha = 1$ for increased stability and accuracy for high frequencies. The latter scheme forms the basis for the dynamical source term integration scheme of WAVEWATCH III (Tolman, 1992, 2002b). For WAVEWATCH III, the diagonal term D follows from Eq. (2.107) or (2.108) as

$$\begin{pmatrix} \delta D_1 \\ \delta D_2 \\ \delta D_3 \\ \delta D_4 \end{pmatrix} = \begin{pmatrix} -K_1' \\ -K_2' \\ K_3' \\ K_4' \end{pmatrix} C' B' \quad , \tag{4.3}$$

where B' is the appropriate scaling function, and where

$$K_1' = k_1^{-1} \left[\frac{N_2}{k_2} \left(\frac{N_3}{k_3} + \frac{N_4}{k_4} \right) - \frac{N_3 N_4}{k_3 k_4} \right] \quad , \tag{4.4}$$

$$K_2' = k_2^{-1} \left[\frac{N_1}{k_1} \left(\frac{N_3}{k_3} + \frac{N_4}{k_4} \right) - \frac{N_3 N_4}{k_3 k_4} \right] \quad , \tag{4.5}$$

$$K_3' = k_3^{-1} \left[\frac{N_1 N_2}{k_1 k_2} - \frac{N_4}{k_4} \left(\frac{N_1}{k_1} + \frac{N_2}{k_2} \right) \right] \quad , \tag{4.6}$$

$$K_4' = k_4^{-1} \left[\frac{N_1 N_2}{k_1 k_2} - \frac{N_3}{k_3} \left(\frac{N_1}{k_1} + \frac{N_2}{k_2} \right) \right] \quad , \tag{4.7}$$

Note that the extra computational effort required to evaluate D is more than compensated for by a much smoother spectral integration with significantly larger dynamically computed time steps.

5   Numerical optimization

In order to be able to optimize parameter settings in the MDIA, a numerically efficient implementation needs to be constructed. There are two aspects to numerical efficiency. The first is the raw computational effort required to assess the MDIA, which is relevant in relation to the computational effort needed for the conventional DIA. Development of a computationally efficient MDIA will be addressed in Section 5.1. The second aspect is the smoothness of integration, which will impact the dynamical time step in the source term integration in WAVEWATCH III. Mostly, this can be addressed only in conjunction with the parameter optimization of the MDIA. In the present study, only filter techniques for the high frequency part of the spectrum as discussed in Section 3 will be addressed inside WAVEWATCH III in Section 5.2. For completeness, the actual equations used in WAVEWATCH III will be summarized in detail here.

Keys to the 'final' version of the MDIA implementation are (i) the formulation in terms of the action spectrum $N(k, \theta)$ [Eq. (2.107)], (ii) using for deep water a proportionality constant compatible with HHAB [Eq. (2.105)], and (iii) using a composite deep and shallow scaling function consistent with Eq. (2.115). This results in the basic equation for discrete interaction contributions

$$
\begin{pmatrix} \delta S_{nl,1} \\ \delta S_{nl,2} \\ \delta S_{nl,3} \\ \delta S_{nl,4} \end{pmatrix} = \begin{pmatrix} -1 \\ -1 \\ 1 \\ 1 \end{pmatrix} \left(\frac{1}{M_d} C_d B_d + \frac{1}{M_s} C_s B_s \right)
$$
$$
\times \left[\frac{N_1}{k_1} \frac{N_2}{k_2} \left(\frac{N_3}{k_3} + \frac{N_4}{k_4} \right) - \frac{N_3}{k_3} \frac{N_4}{k_4} \left(\frac{N_1}{k_1} + \frac{N_2}{k_2} \right) \right], \quad (5.1)
$$

and the corresponding diagonal contributions

$$
\begin{pmatrix} \delta D_1 \\ \delta D_2 \\ \delta D_3 \\ \delta D_4 \end{pmatrix} = \begin{pmatrix} -K_1' \\ -K_2' \\ K_3' \\ K_4' \end{pmatrix} \left(\frac{1}{M_d} C_d B_d + \frac{1}{M_s} C_s B_s \right) \quad , \qquad (5.2)
$$

with the corresponding diagonal contributions K_i' from Eqs. (4.4) through (4.7). In these equations C_d in the proportionality constant for the deep water scaling consistent with the constant in HHAB, C_s is the corresponding constant in the shallow water scaling, B_d and B_s are the deep and shallow water scaling functions,

$$
B_d = \frac{k^{4+m} \, \sigma^{12-2m}}{(2\pi)^9 \, g^{4-m} \, c_g} \quad , \tag{5.3}
$$

$$
B_s = \frac{g^2 \, k^{10}}{(2\pi)^9 \, c_g} (kd)^n \quad , \tag{5.4}
$$

respectively. Consistent with the MDIA experiments of Section 2, quadruplets should have separate proportionality constants for both scaling ranges, or should be identified for one range only. M_d and M_s are the number of quadruplet definitions used for for the deep and shallow scaling, respectively. Formally, these normalization factors belong in the summation of all contributions from all quadruplet realizations (2.63). However, because M_d and M_s do not need to be equal, these factors are more elegantly included in Eq. (5.1). Furthermore considering that the devision by 2 in Eq. (2.63) is included in the scaling functions (5.3) and (5.4), the former equation simply becomes

$$S_{nl} = \sum \delta S_{nl} \quad . \tag{5.5}$$

Note that the spectral conversion from $F(f, \theta)$ to $N(k, \theta)$ does not influence the value of m and n, since both parameters address the scaling behavior of the coupling coefficient G only.

5.1 Computational optimization

Numerical optimization of any computer code addresses minimization of the work done, and making work done efficient by using 'vector' style operations. In the present context, it is irrelevant to address parallelization, since WAVEWATCH III incorporates effective parallel paradigms at a higher level in the code (Tolman, 2002a). Most relevantly, this wave model uses a parallelization method where source terms for different spatial grid points are addressed in parallel.

A first inspection of shallow water energy distribution equations like Eq. (2.100) and (2.107) indicates that the complexity of the product term greatly depends on the spectral description chosen. Clearly, the description for the action spectrum $N(k, \theta)$ [Eq. (2.107)] is much simpler than the equation for the energy spectrum $F(f, \theta)$ [Eq. (2.100)], and the simplest form is obtained for the action spectrum $n(\boldsymbol{k})$, cf. Eqs. (2.2) and (2.4). Note that for any spectral description, the equation can be recast in terms of a pseudo spectrum $\mathcal{F}$

$$\begin{pmatrix} \delta S_{nl,1} \\ \delta S_{nl,2} \\ \delta S_{nl,3} \\ \delta S_{nl,4} \end{pmatrix} = \begin{pmatrix} -1 \\ -1 \\ 1 \\ 1 \end{pmatrix} CB \left[\mathcal{F}_1 \mathcal{F}_2 \left(\mathcal{F}_3 + \mathcal{F}_4 \right) - \mathcal{F}_3 \mathcal{F}_4 \left(\mathcal{F}_1 + \mathcal{F}_2 \right) \right] \quad , \tag{5.6}$$

where the scaling function B still depends on the actual spectrum for which the DIA is formulated. For application in WAVEWATCH III, solving Eq. (2.107), the pseudo spectrum is defined as

$$\mathcal{F}_i = \frac{N(k_i, \theta_i)}{k_i} \quad , \tag{5.7}$$
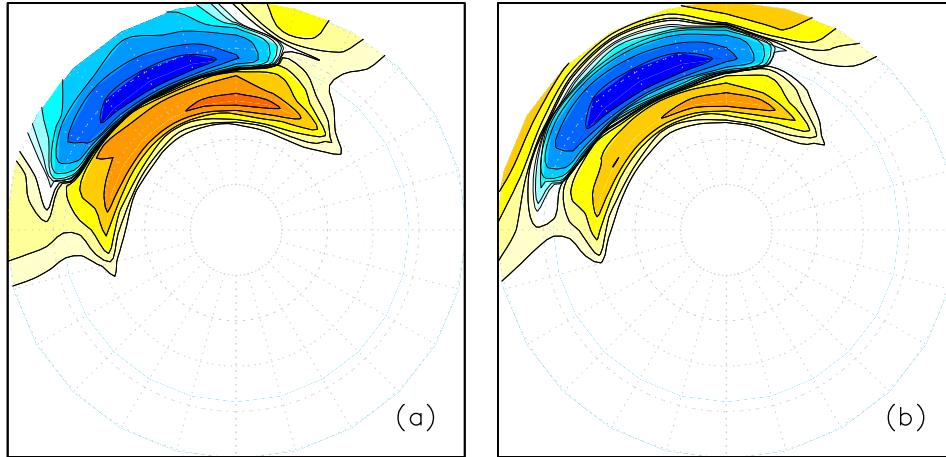
Fig. 5.1 : *Interactions computed from a given model spectrum in deep water for the traditional DIA and its quadruplet for (a) computations of interactions in terms of $F(f, \theta)$ and (b) in terms of $\mathcal{F} = N(k, \theta)/k$.*

and similar pseudo spectra can be defined for each spectral description for which the DIA is defined directly. With the pseudo spectra, the spectrum is converted only once, after which components of quadruplets are interpolated from the pseudo spectrum directly, thus simplifying the computation of the product term. This mainly result in much simpler expressions, but has only a moderate to negligible impact on the numerical economy.

However, the choice of (pseudo) spectral description does have a distinct impact on the resulting interactions. These differences occur because, depending on the description used, factors in the product term are directly evaluated at the quadruplet components, or are implicitly interpolated from the discrete spectral grid. The highly nonlinear nature of S_{nl} results in a rather significant impact of choices of spectra description. This is illustrated in Fig. 5.1, with interactions computed from either $F(f, \theta)$ or $N(k, \theta)/k$. Clearly, the differences are significant. The first interaction is consistent with the traditional DIA, whereas the second is consistent with the original description of interaction in terms of actions. For now, the action description will be used here, acknowledging that a switch back may be needed of the interaction parameters are optimized.

Another way to speed up computations is to pre-compute where possible. For the nonlinear interactions, this mostly concerns quadruplet layouts. This is particularly true for the conventional DIA, where the quadruplet layout remains unchanged throughout the spectral grid. Only one set of interpolation addresses and weights then needs to be saved. In WAVEWATCH III, the traditional DIA is furthermore optimized by organizing computations in long vector loops. The structure of the computational subroutine is illustrated in Fig. 5.2. In order to effectively execute the long loops over (extended) discrete spectral space, arrays

85

computational subroutine

| Compute depth scaling factor
Expand discrete spectral space to high and low frequencies
Initialize working arrays |
| Do for all bins in expended spectral space |
| Compute energy at quadruplet components
    Compute interaction strength
    Compute diagonal strength |
| Do for all bins in model spectral space |
| Combine interaction contributions
    Combine diagonal contributions |

Fig. 5.2 : Algorithm for computing the conventional DIA in the WAVE-WATCH III model.

with addressing information are constructed in an initialization routing, that is only run once during program execution (see w3snl1md.ftn for details). This highly optimized routine will be used as a timing benchmark.

The routines used so far in this study and in Part 2 have been designed to strike a balance between ease and transparency of coding and numerical efficiency. The corresponding algorithm is presented in Fig. 5.3. Note that this algorithm uses a minimum of preprocessing, and that the quadruplet layout is recomputed in the computational algorithm for each quadruplet and frequency separately. Because these settings are used for each direction, the overhead of re-establishing the quadruplet layouts in fact is modest.

To address the numerical efficiency of various DIA implementations, three test cases are considered. The first is the traditional DIA with the one-parameter quadruplet definition with $\lambda = 0.25$,. The second is a DIA with a single quadruplet definition, but with a two-parameter quadruplet definition with $\mu = 0.10$ and $\lambda = 0.25$. Note that this DIA definition does not result in stable model integration (see Part 2). However, in the context of model economy it is relevant as it identifies the origin of differences in computational effort between algorithms. The final test case is a four component MDIA, as described in the left side of Table 2.3. The 'out-of-the-box' test provided with WAVEWATCH III is used with a discrete spectrum with 24 direction and 25 frequencies. All computations are performed on a Linux system with a Portland compiler (aggressive optimization), by calling the subroutines 1000 times for a given wave spectrum. The differences in the computational cost, however, can be related directly to the amount of operations performed, and should therefore be more generally applicable.

Timing results for the algorithm of Fig. 5.3, normalized with the results of

computational subroutine

| Expand discrete spectral space for pseudo spectrum |
| Initialize working arrays |

Do for all quadruplet definitions

  Do for all frequencies (expanded range)

    Determine quadruplet layout
    Compute proportionality constant

    Do for all directions

      Do for all four quadruplet realizations

        Get quadruplet energies
        Compute interaction and diagonal strength
        Apply contributions in expanded spectral space

Go from expanded to normal spectral space
Normalize for number of quadruplets

Fig. 5.3 : Algorithm for computing the generalized DIA in the previous sections of the present study.

the conventional DIA of Fig. 5.2 are presented in Table 5.1. Note that the conventional DIA is run only for the first case.

The generalized MDIA in its non-optimized configuration is significantly slower to run than the optimized conventional DIA, typically by a factor of 10. This factor can be explained by the increased amount of computations to be performed in the generalized algorithm. A factor of 2 can be expected because the generalized MDIA assesses 4 realizations of a quadruplet layout, whereas the conventional DIA assesses only 2 realizations. Furthermore, the computational effort of a DIA is dominated by the work done to gather quadruplet energies, and to distribute contributions over spectral space. In the conventional DIA, the gathering and redistribution concern 9 discrete spectral bins, whereas for the generalized MDIA 16 discrete bins are considered, accounting for another factor of approximately 2. The remaining factor 2.5 in run time difference is consistent with general optimization procedures used in the conventional DIA, but absent in the generalized MDIA. In the generalized algorithm of Fig. 5.3, the computational effort scales linearly with the number of representative quadruplet definitions. This explains why the MDIA with four representative quadruplets (case 3) is 4 times more expensive to run than the MDIAs with one representative quadruplet (cases 1 and 2).

One method to optimize nonlinear computations is the so-called triplet method. This method uses the property of the nonlinear interactions that each discrete

Table 5.1: Run times for various DIA and MDIA algorithms normalized with the run time for the convention DIA with one representative quadruplet, defined by λ alone. Case 1: traditional quadruplet ($\lambda = 0.25$). Case 2: two parameter quadruplet ($\lambda = 0.25$, $\mu = 0.10$). Case 3: four component MDIA from Table 2.3. For reference, the normalized run time of the exact interactions used here is approximately 1500.

Algorithm		Case 1	Case 2	Case 3
Conventional DIA	(Fig. 5.2)	1	–	–
First MDIA	(Fig. 5.3)	10.	10.	41.
Triplet unfiltered	(Fig. 5.4)	60.	750.	3300.
Triplet $\epsilon_1 = \epsilon_2 = 0.25$	(Fig. 5.4)	7.6	62.	350.
Optimized MDIA	(Fig. 5.8)	2.1	3.6	13.

interaction $S_{nl}(k_i, \theta_j)$ consisting of all contributions from Eq. (5.6) can be constructed as a sum of triple products (triplets) of pseudo spectral values corresponding to individual quadruplet realizations.

$$S_{nl}(k_i, \theta_j) = \sum_{l,m,n} w_{i,j,l,m,n} \mathcal{F}_l \mathcal{F}_m \mathcal{F}_n = \sum_{l,m,n} w_{i,j,l,m,n} \mathcal{T}_{l,m,n} \quad , \qquad (5.8)$$

where w represents a weight, and $\mathcal{F}_l$, $\mathcal{F}_m$ and $\mathcal{F}_n$ represent pseudo spectral values in the discrete spectral space. This method was originally introduced by Snyder et al. (1993, 1998) as an efficient way to compute exact interactions on a relatively coarse discrete spectral grid. More recently Van Vledder (2005) used this method to optimize an MDIA based on the convectional single-parameter quadruplet definition, and has shown good numerical efficiency in this case. However, it does not appear that this method is generally efficient for a generalized quadruplet definition.

In a continuous spectral space, each individual quadruplet results in 4 triplets $\mathcal{T}_{l,m,n}$ in the evaluation of the product term in Eq. (5.6). In a discrete space, however, $\mathcal{F}_l$ etc. are a weighted average of up to four discrete spectral values. Hence, the evaluation of the product term in Eq. (5.6) for a single quadruplet can require the evaluation of as many as $4 \times 4^3 = 256$ triplets $\mathcal{T}_{l,m,n}$. Furthermore, these results need to be redistributed to the four discrete spectral locations from which all for quadruplet elements are gathered (a total of 4^2 locations), or conversely, up to to 4^2 quadruplets contribute to the interaction at each discrete spectral grid point. Finally, each quadruplet has up to 4 realizations. Hence, the evaluation of the nonlinear interactions for a given spectral point can require up to $4^7 = 16,384$ triplets $\mathcal{T}_{l,m,n}$.

For the conventional quadruplet definition, much fewer triplets need to be

evaluated. First, $\mathcal{F}_1$ and $\mathcal{F}_2$ coincide with one single discrete spectral grid point, whereas $\mathcal{F}_3$ and $\mathcal{F}_4$ are obtained by interpolation from 4 grid points. It can be shown that the corresponding evaluation of the product term in Eq. (5.6) then only requires 24 triplets $\mathcal{T}_{l,m,n}$. Furthermore, only 9 discrete spectral grid points contribute to the interactions in a given point, and only 2 realization exist of each quadruplet. Hence, for the conventional quadruplet definition, only $24 \times 9 \times 2 = 432$ triplets $\mathcal{T}_{l,m,n}$ can contribute. This is in stark contrast to the 16,384 triplets found above.

This leaves a significant number of triplets to be evaluated for each individual spectral grid point, even for the conventional quadruplet. To address the economical feasibility of the triplet method in the present context, a simplified triplet code has been developed here. The three main simplifications and assumptions are (1) deep water will be considered for an initial assessment of the economical feasibility, (2) the diagonal term will not yet be considered, and (3) triplet tables are evaluated for frequencies only, requiring indirect addressing for application in the full spectral space. The latter is not as efficient as direct addressing for each individual discrete spectral component, but will be essential for reduction of internal storage required in an application for arbitrary depths. The basic algorithm for the triplet method is presented in Fig. 5.4.

The actual computational routine for the triplet method is almost trivial, consisting of three nested loops, including the summation in Eq. (5.8). Most coding is required for the computation of triplet data in the initialization routine. This, however, needs to be done only once, and the resulting triplet data can easily be retained in memory. Resulting run times of this approach are presented in Table 5.1, and resulting triplet counts are presented in Table 5.2.

Run times for the raw triplet methods are significantly longer that those of the initial MDIA algorithm of Fig. 5.3. For case 3, this approach in fact is slower than the exact interaction routines used in this study. The more complex quadruplet layout of case 2 (compared to case 1) results in an increase of the number of triplets of a factor of approximately 15, and in a similar increase in computing time. For the multiple quadruplet approach of case 3, the number of triplets increases by another factor of 4, and a comparable increase in computing time. Apparently, the number of duplicate quadruplets in the MDIA environment with the expanded definition of the quadruplet is negligible, unlike for a similar approach with the conventional quadruplet definition of the DIA (Van Vledder, 2005).

However, the triplet approach can be sped up significantly by filtering the triplets to be used in the computation. In Fig. 5.4, three different filter locations are identified (ϵ_1, ϵ_2 and ϵ_3). In all these cases, only triplets are retained for which

$$w \geq \epsilon_i \, w_{\max} \quad , \tag{5.9}$$

where w are (partial) weigh factors for triplets (see discussion of individual filters

initialization subroutine

Expand discrete spectral space as needed
Initialize working arrays

Do for all frequencies

> Do for all quadruplet definitions
>
> > Determine quadruplet layout
> > Compute proportionality constant
> >
> > Do for four realizations of quadruplet
> >
> > > Construct 256 triplets of product term of Eq. (5.6)
> > > Combine into unique triplets
> > > Filter based on relative weight (ϵ_1)
> > >
> > > Distribute resulting triplets to 16 contributing
> > > discrete spectral grid points, filter on distribution
> > > weight (ϵ_2). Proportionality constant added

Do for all frequencies

> Combine results into unique triplets
> Filter based on relative weight (ϵ_3)
> Store resulting quadruplet information

computational subroutine

Expand discrete spectral space for pseudo spectrum
Do for all frequencies

> Do for all directions
>
> > Evaluate Eq. (5.8)

Fig. 5.4 : *Algorithm for computing the generalized DIA using triplets.*

Table 5.2: Triplet counts for a single discrete spectral nonlinear interaction for various MDIA applications. Cases as in Table 5.1

	Case 1	Case 2	Case 3
Maximum number of triplets	432	16,384	65,536
Actual unique triplets	426	6,674	25,986
Triplets for $\epsilon_1 = 0.25$	144	1,042	5,645
Triplets for $\epsilon_1 = 0.25$, $\epsilon_2 = 0.25$	64	526	2,937
Triplets for $\epsilon_1 = 0.25$, $\epsilon_2 = 0.25$, $\epsilon_3 = 0.001$	32	230	738

below). Effects of these filters are illustrated in Figs 5.5 through 5.7 for cases 1 through 3, respectively.

The first filter (ϵ_1) is applied for the triplets $\mathcal{T}_{l,m,n}$ that make up the product term in Eq. (5.6) which determines the strength of the local interactions. Applying this filter may modify the local interaction strength, but does in no way impact conservation properties of the nonlinear interactions. Tentatively, filter levels of $\epsilon_1 \approx 0.001$ filters out only very small contributions, and hence is expected to have little or no impact on resulting interactions. This is easily verified with numerical computations. Somewhat surprisingly, this filter can be applied aggressively with values as large as $\epsilon_1 = 0.25$. This is illustrated in the (b) panels of Figs 5.5 through 5.7, which show interaction from the triplet method with $\epsilon_1 = 0.25$. Clearly, the filtering has only a moderate impact on the resulting interactions, with a larger impact on the more complex cases. Note that the number of resulting triplets is reduced by factors of approximately 3, 6 and 5 for the three separate cases (Table 5.2), with similar impacts on computational effort (results not presented here).

The second filter (ϵ_2) is applied to the distribution of the triplets that describe the interactions strength to individual discrete spectral components, and again deals directly with interpolation weights. If the interpolation weight for an individual spectral contribution is too small in the filter, none of the triplets describing the interaction strength are applied to the discrete spectral grid point considered. Note that this filter does impact the conservation properties of the interactions, as discrete contributions within a quadruplet are selectively ignored. This filter, however, can also be applied aggressively with moderate impact on the resulting interactions. This is illustrated with results for $\epsilon_1 = 0.25$ and $\epsilon_2 = 0.25$ in the (c) panels of Figs 5.5 through 5.7. Results are again only moderately changes, whereas the number of triplets used again is reduced by a factor of typically 2.

The third filter (ϵ_3) is applied after all resulting triplets have been combined. Therefore, weight factors used in this level of filtering include proportionality
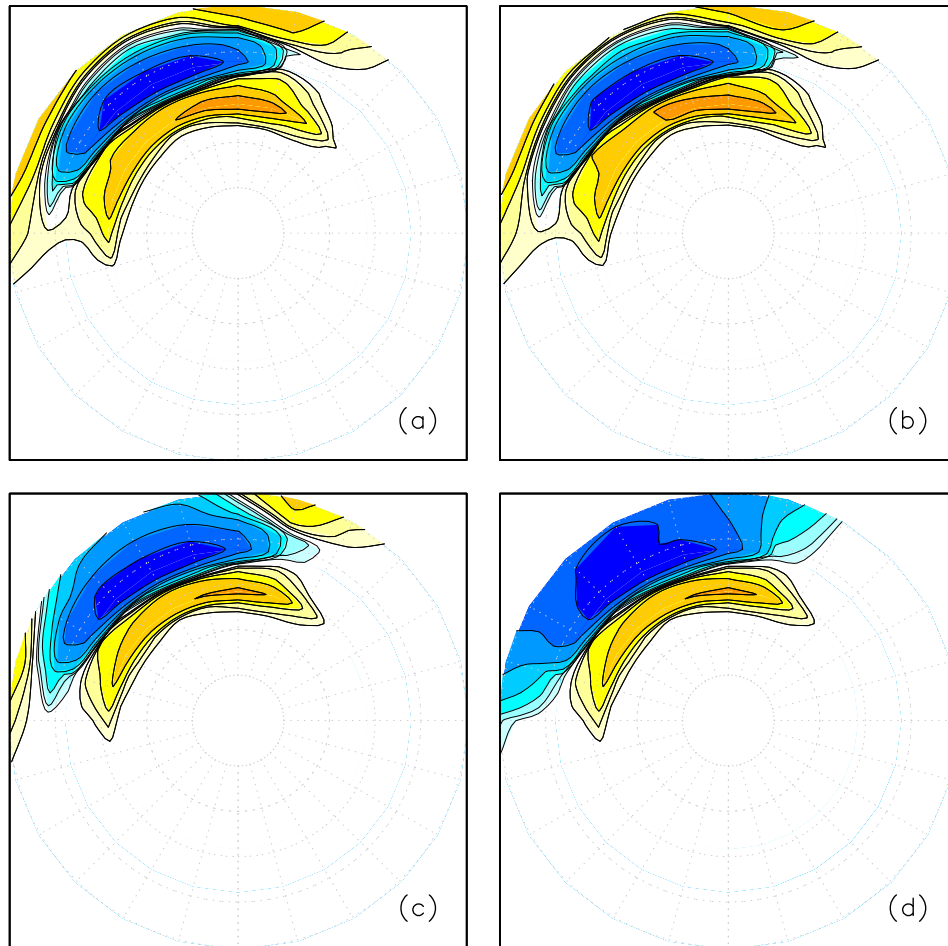
Fig. 5.5 : Effects of filtering on the triplet method for a test spectrum and
case 1 (traditional DIA quadruplet with $\lambda = 0.25$). (a) Unfiltered results.
(b) Adding filter with $\epsilon_1 = 0.25$. (c) Also adding $\epsilon_2 = 0.25$. (d) Also
adding $\epsilon_3 = 0.001$. Scaling identical in all panels.

92
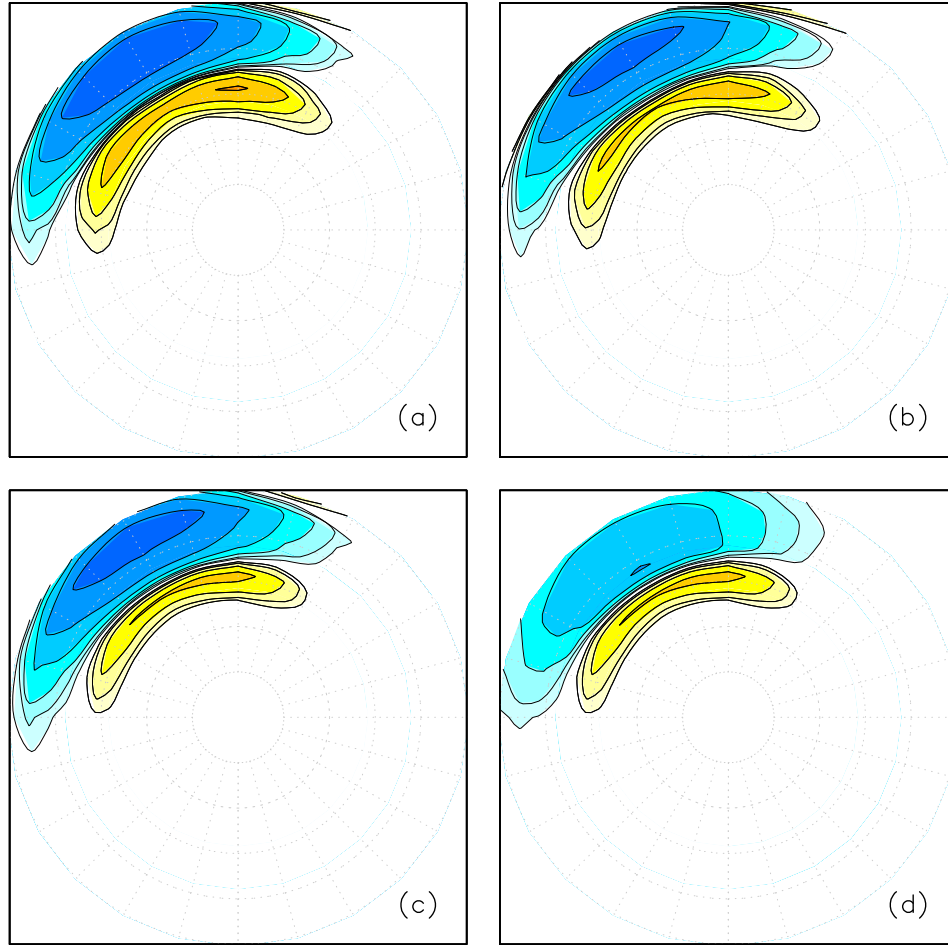
Fig. 5.6 : Like Fig. 5.5 for case 2, with expanded quadruplet definition ($\lambda =$ 0.25, $\mu = 0.10$). Scaling as in Fig. 5.5.

constants. Due to the strong dependency of the proportionality constant with frequency. this filter will have a distinct impact even for smaller values of the filter. This is illustrated in the (d) panels of the figures for $\epsilon_3 = 0.001$. Clearly this filter has a particularly large impact on high-frequency interactions. It is therefore not advisable to use this filter.

Considering the above, the triplet approach can be used with aggressive setting of the first two filters, but should not be used with the third filter. To obtain a representative estimate of the numerical economy of such an approach, run times for $\epsilon_1 = \epsilon_2 = 0.25$ and $\epsilon_3 = 0$ are presented in Table 5.1. These results correspond to Figs 5.5c through 5.7c. Note that this filtering technique mostly weakens the interactions. If the filter is used in the holistic optimization of the interaction (see Part 2), then this weakening is automatically accounted for as part of the optimization. Alternatively, resulting weights after filtering can be
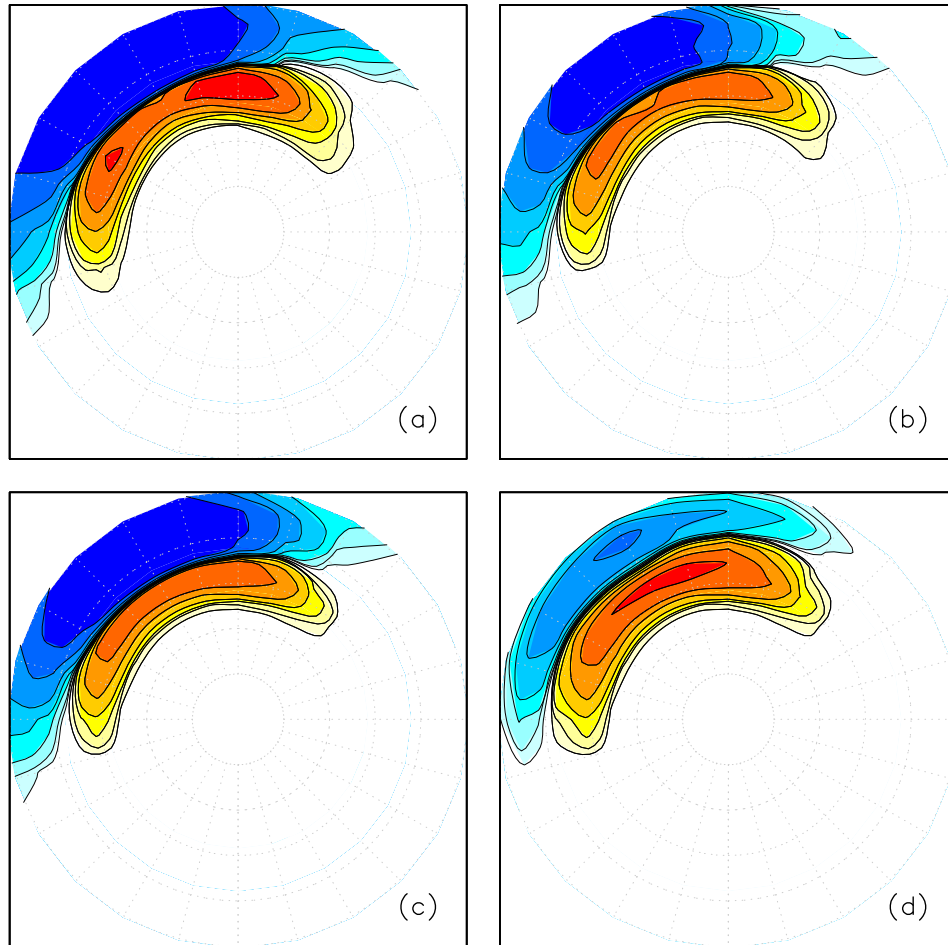
Fig. 5.7 : Like Fig. 5.5 for case 3, (MDIA from Table 2.3). Scaling as in
Fig. 5.5.

renormalized for the first two filters.

With the aggressive filtering, the economy of case 1 is improved compared
to the general implementation used in the previous section. For more com-
plex quadruplets and the MDIA with more complex quadruplets, the triplet
method remains substantially slower that the partially optimized direct method
of Fig. 5.3. Considering that this triplet method does not yet include the eval-
uation of the diagonal terms, nor actual applications to shallow water, it does
not appear that this triplet method will be an economically feasible approach for
the generalized multiple DIA presented in the present study. The only exception
may be an MDIA with the traditional single parameter quadruplet definition and
with many representative quadruplet. The latter would be consistent with the
results of Van Vledder (2005).

Considering the above results with the triplet method, it is prudent to merge optimization techniques used for the traditional DIA (Fig. 5.2) with the previously used algorithm for the generalized multiple DIA (Fig. 5.3). The resulting algorithm is presented in Fig. 5.8. This algorithm is more involved than previous algorithms, because it balances the basic approach of the traditional DIA of Fig. 5.2 with the need to efficiently store precomputed interpolation and distribution data. The latter requires compact storage and the use of indirect addressing in spectral space, rather than providing absolute offset data for each individual discrete spectral grid point. First, it is recognized that all relative addresses and interpolation or redistribution data for all discrete directions for a given discrete frequency are identical. For each frequency, however, interpolation data may be different due to differences in relative depths kd for each discrete frequency. Instead of recomputing these data for each frequency for each subroutine call, such data are stored for discrete nondimensional depths kd.

For these discrete relative depths to be equally accurate in various spectral ranges, increments in kd need to be consistent with frequency increments in the spectral grid. From the dispersion relation (1.6) a non-dimensional frequency $\tilde{\sigma}$ can be defined as

$$\tilde{\sigma}^2 = \frac{\sigma^2 d}{g} = kd \tanh kd \quad . \tag{5.10}$$

By defining a minimum and maximum relative depths $kd_{\min}$ and $kd_{\max}$, the corresponding frequencies $\tilde{\sigma}_{\min}$ and $\tilde{\sigma}_{\max}$ are defined. Using a nondimensional frequency grid consistent with (1.8)

$$\tilde{\sigma}_{i+1} = \tilde{X}\tilde{\sigma}_i \quad , \tag{5.11}$$

assures that the resolution of in interpolation table is uniform in the discrete spectral space. Using n_d discrete relative depths, $\tilde{X}$ becomes

$$\tilde{X} = (\tilde{\sigma}_{\max}/\tilde{\sigma}_{\min})^{(n_d-1)^{-1}} \quad . \tag{5.12}$$

For a typical low lowest model frequency of 0.03 Hz, and a typical minimum realistic depth of 1 m, the smallest relative depth in a model is $kd \approx 0.06$. With this in mind $kd_{\min} = 0.025$ is set as the default in the model. With a typical setting of $kd_{\max} = 10.$ and $n_d = 250$, the relative depth increment is approximately 2% ($\tilde{X} = 1.0196$), which is significantly better than the typical spectral resolution, and hence appears generally acceptable.

Note that the outer loop in the computational routine considers quadruplet realizations and not quadruplet layouts. This implies that the duplication of identical quadruplet realizations for the conventional one-parameter quadruplet layout can be avoided in a simple way (at [a] in Fig. 5.8). Note that this speeds up the computations for case 1 significantly, but that this has no impact on the

initialization subroutine

Initialize discrete nondimensional depths
Do for all nondimensional depths

> Do for all representative quadruplets
>
> > compute offsets, indices and weights
> >
> > Do for 2 or 4 quadruplet realizations   (a)
> >
> > > Put data into temporary storage

Determine extended spectral ranges
Do for all nondimensional depths

> Do for all quadruplet realizations
>
> > Store offsets, weights and factors for the computation
> > of quadruplet energies and contributions to the
> > interactions and diagonal term   (b)

Do for all nondimensional depths

> Do for all quadruplet realizations
>
> > Do for 4 elements of quadruplet
> >
> > > Do for 2 frequency offsets
> > >
> > > > Get directional indices
> > > >
> > > > Do for 2 or 4 quadruplet realizations   (a)
> > > >
> > > > > Store data for putting together interactions
> > > > > and diagonal from contributions   (c)

Finalize storage and clean up

Fig. 5.8 : Optimized algorithm for computing the generalized DIA, based on techniques used for the conventional DIA (Fig. 5.2).

computational subroutine

Expand discrete spectral space as needed Initialize working arrays			(d)
Do for all quadruplet realizations			
	Do for expanded frequency range		
		Retrieve offsets and weights	
		Do for all directions	
			Compute quadruplet energies Compute interaction and diagonal contributions (b)
	Do for expanded frequency range		
		Retrieve offsets and weights	
		Do for all directions	
			Compute interactions and diagonal strength (c)

Fig. 5.8 continued

computational effort for cases 2 and 3 (due to the representative quadruplets used).

As with the triplet approach, filtering of computations can be considered. First, the number of discrete spectral grid points from which the quadruplet energies are computed can be reduced based on the relative interpolation weighs (at [b] in Fig. 5.8). Such an approach proves to speed the code by only a few percentage points, while requiring a massively more complicated source code. This kind of filtering will therefore not be used here. Similarly, distributions of contributions to the grid can be filtered (at [c] in Fig. 5.8). A quick assessment of the potential of this filtering indicates a maximum possible speedup of 10 to 15%, at the cost of a much more complicated code. The latter may well counteract the possible gain, and therefore this filtering is also not considered here in detail.

Finally, filtering can be used to apply quadruplets defined only with deep or shallow scaling of Eqs. (5.3) and (5.4) only at depth that are consistent wit this filtering. Tentatively, it would be possible to filter based on the ratio of these two scaling functions. However, since there is no requirement or guarantee that C_d and C_s are consistent, this would not be a very robust scaling approach. Instead, the interactions based on Eqs. (5.3) only ($C_s = 0.$) will be computed only for frequencies where

$$kd \geq kd_{fd} \quad , \tag{5.13}$$

and interactions based on Eqs. (5.4) only ($C_d = 0.$) will be computed only for frequencies where

$$kd \leq kd_{fs} \quad , \tag{5.14}$$

where kd_{fd} and kd_{fs} are the nondimensional depths of the filter, as defined externally by the user of the code. This filtering modifies the computational frequency ranges at $^{(d)}$ in Fig. 5.8. Values like

$$kd_{fd} \approx 0.25 \quad kd_{fs} \approx 3.00$$

will virtually guarantee no impact of the filter. Typically, the MDIA could be tuned with such values, after which optimum filter values can be found by making the filter more restrictive until an influence can be seen in the resulting interactions. Note that this filter is not applied if both C_d and C_s are non-zero for a given quadruplet layout, and that this filter had no impact on the timing test presented here due to the moderately limited water depths.

The final run times of this code are presented in Fig. 5.1. The speed-up obtained compared to the original code are substantial, with a factor of nearly 5 for case 1 and of nearly 3 for cases 2 and 3. The new code applied with the quadruplet definition of the original DIA is a factor of 2 slower that the much simpler traditional DIA. This seems to be a reasonable price to pay for full inclusion of shallow water effects, and for appropriate scaling behavior up to extremely shallow water ($kd \approx 0.025$). With the traditional DIA taking approximately 25% of the computational effort of the total model, this will correspond to a 25% increase in overall model run time (ignoring possible impact through adjustment of time steps). Whereas the MDIA is significantly more expensive, practical applications should be well under a factor 20 more expensive than the conventional DIA. This makes the increase in costs for the model well under a factor 5, roughly corresponding to historical operational computing capability increases in two to three years. Hence, such a model is economically feasible for operational wave modeling in the near future.

As a final test of the resulting generalized MDIA codes, this code has been fully integrated in the WAVEWATCH III model. For the present purpose, it is implemented in the 'user' slot (NLX) of model version 3.13. The code is intended for distribution in release 4 of the WAVEWATCH III code. Figures 5.9 through 5.11 shows some example results of the model with different nonlinear source term options.

Figure 5.9 shows the results for the default WAVEWATCH III model with the conventional DIA (corresponding to the default setting of model version 2.22). Figure 5.10 shows the results for the new source term with the same parameters settings (case 1 in this section). Ideally, these results would be nearly identical. However, the differences introduced by different spectral descriptions (see
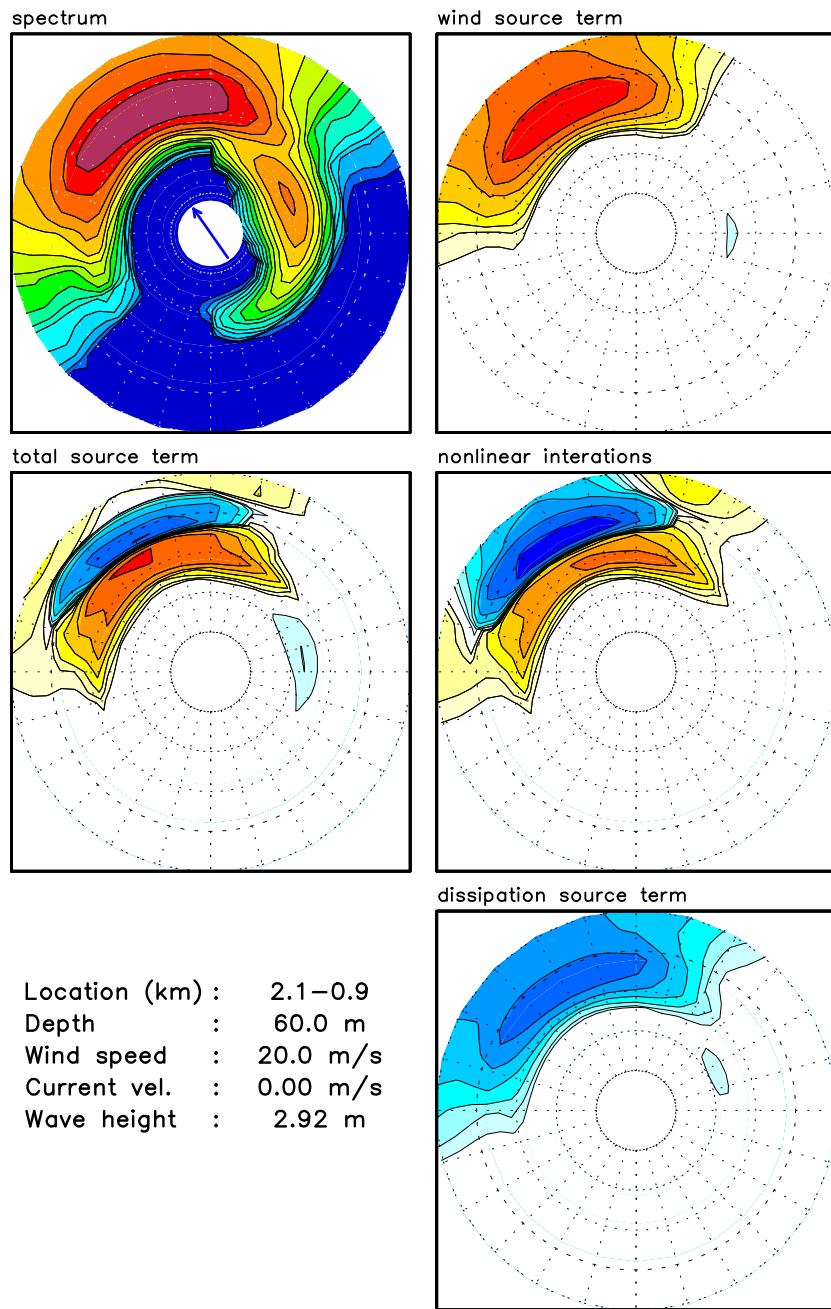
spectrum

wind source term

total source term

nonlinear interations

Location (km) :   2.1−0.9
Depth   :   60.0 m
Wind speed   :   20.0 m/s
Current vel. :   0.00 m/s
Wave height   :   2.92 m

dissipation source term

Fig. 5.9 : Spectrum and source terms from model run with traditional DIA
(default WAVEWATCH III).

99

spectrum

wind source term

total source term

nonlinear interations

dissipation source term

Location (km)	:	2.1−0.9
Depth	:	60.0 m
Wind speed	:	20.0 m/s
Current vel.	:	0.00 m/s
Wave height	:	2.43 m
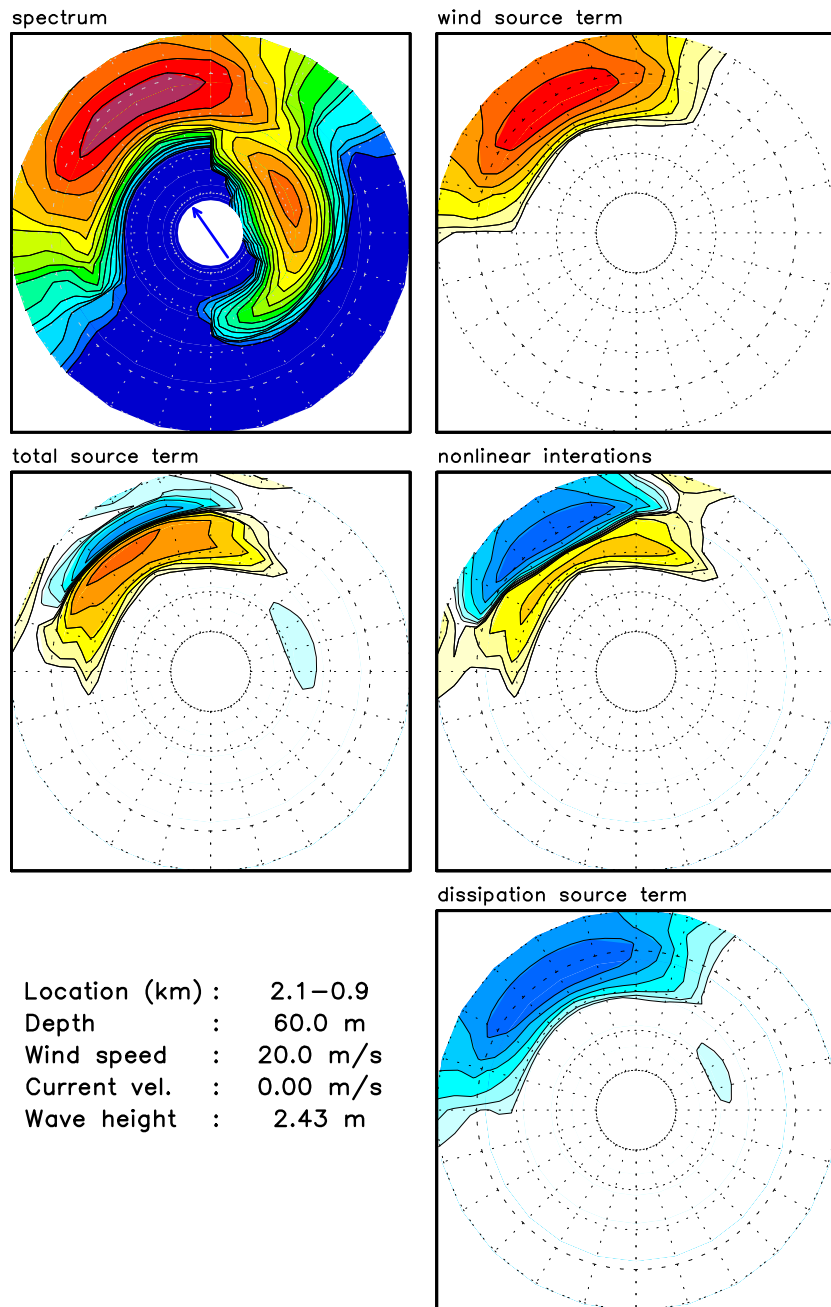
Fig. 5.10 : Like Fig. 5.9 for new model setting with quadruplet setting from case 1

.

spectrum

wind source term

total source term

nonlinear interations

dissipation source term

Location (km)	:	2.1−0.9
Depth	:	60.0 m
Wind speed	:	20.0 m/s
Current vel.	:	0.00 m/s
Wave height	:	2.38 m
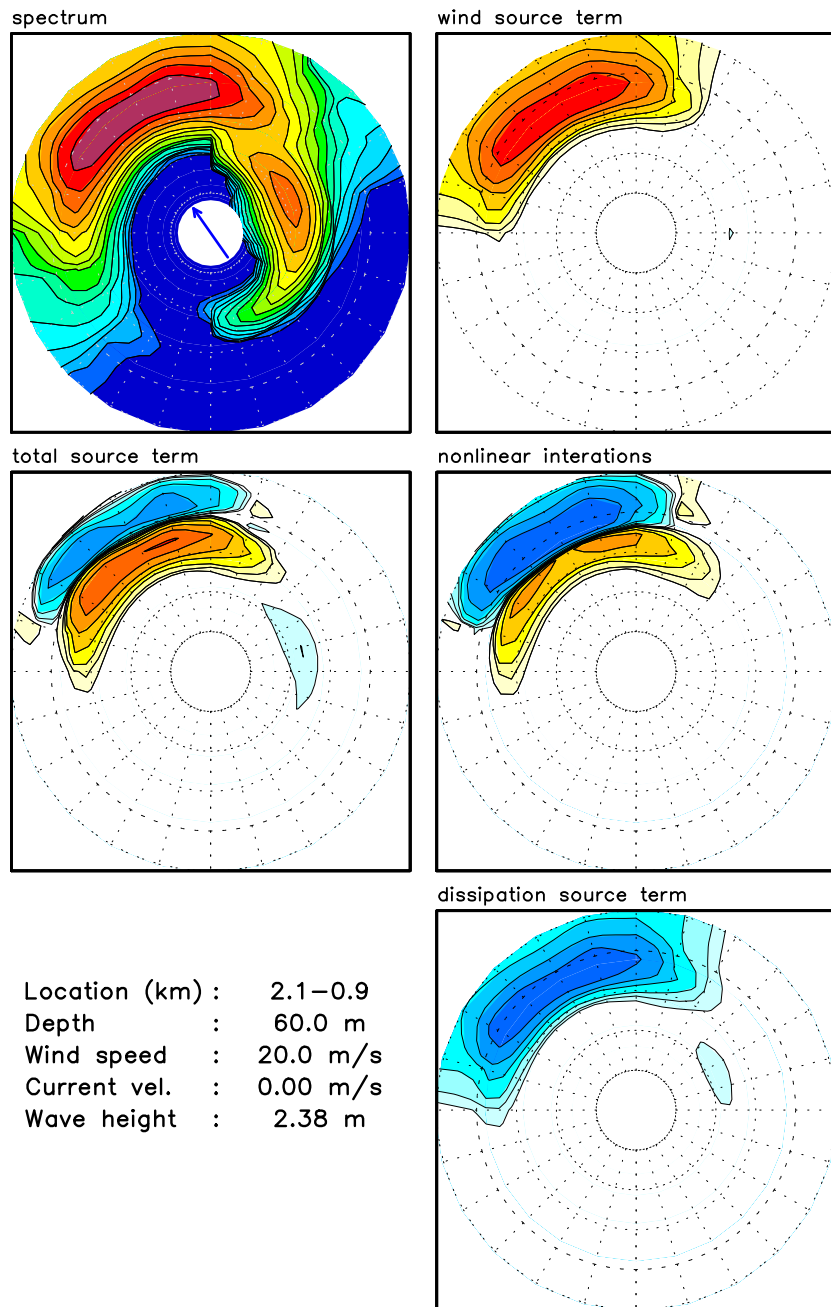
Fig. 5.11 : Like Fig. 5.9 for new model setting with quadruplet setting from case 3
.

Fig. 5.1) has a significant impact on model results. This implies that the new interaction approach is not fully 'backward compatible' with the original DIA. The new approach increased the model run time by approximately 20%, as was expected.

Figure 5.11 presents results for the MDIA used in this section (case 3). This implementation shows stable model results at approximately 3 times the cost of the default model, with clear differences in the spectral shape and (nonlinear) source terms. Note that case 2 is not run in this context because the approach was proven unstable in Part 2 (as was verified here).

5.2   Filtering for high frequencies

With the generalized interaction approximation included in the WAVEWATCH III model, only the potential benefits and inner workings of a smoothing / diffusion operator for high frequencies as outlined in Section 3 still need to be assessed. The starting point will be the diffusion equivalent high frequency interactions, with the integration method that degenerates to a conservative smoother. In Section 3, expressions are given in terms of the energy spectrum F. In the present section, the action description of WAVEWATCH III and the corresponding Eqs. (5.1) through (5.5) will be used. Using these equations and considering that the high frequency flank of the spectrum will rarely if ever correspond to extremely shallow water, only the 'deep water' scaling B_d needs to be used, and considering the approximate application used here, only a reasonable value of $m = 4$ is used in the corresponding expression. The action based equation equivalent to Eq. (3.19) then becomes

$$\Delta \tilde{N}_{1,2} = -M_c \, \Phi(f) \, C \, \frac{k^8 \, \sigma^4}{(2\pi)^9 \, c_g} \, P_{1234} \, \Delta t \, N^{-1} \quad , \tag{5.15}$$

where the product term is taken from Eq. (5.1), M_c represents the cumulative interpolation factors of all quadruplet components inside the nine point stencil from Eq. (3.9), and where $\Phi(f)$ is adopted unchanged from Eq (3.15)

$$\Phi(f) = \exp \left[-c_1 \left(\frac{f}{c_2 f_p} \right)^{-c_3} \right] \quad , \tag{5.16}$$

with c_1 through c_3 as tunable parameters, and where the quadruplet layout is defined by either λ or a_{34} as in Eqs. (3.18) and (1.8).

This corresponds to a high-frequency only source term comprised of Eq. (5.1) combined with the filter function (5.16), which is to be combined with an integration technique that reduces it to a conservative filter for large source term values. A first impression of the potential and inner workings of such a filter can be assessed by looking at the behavior of the underlying filtered source term.
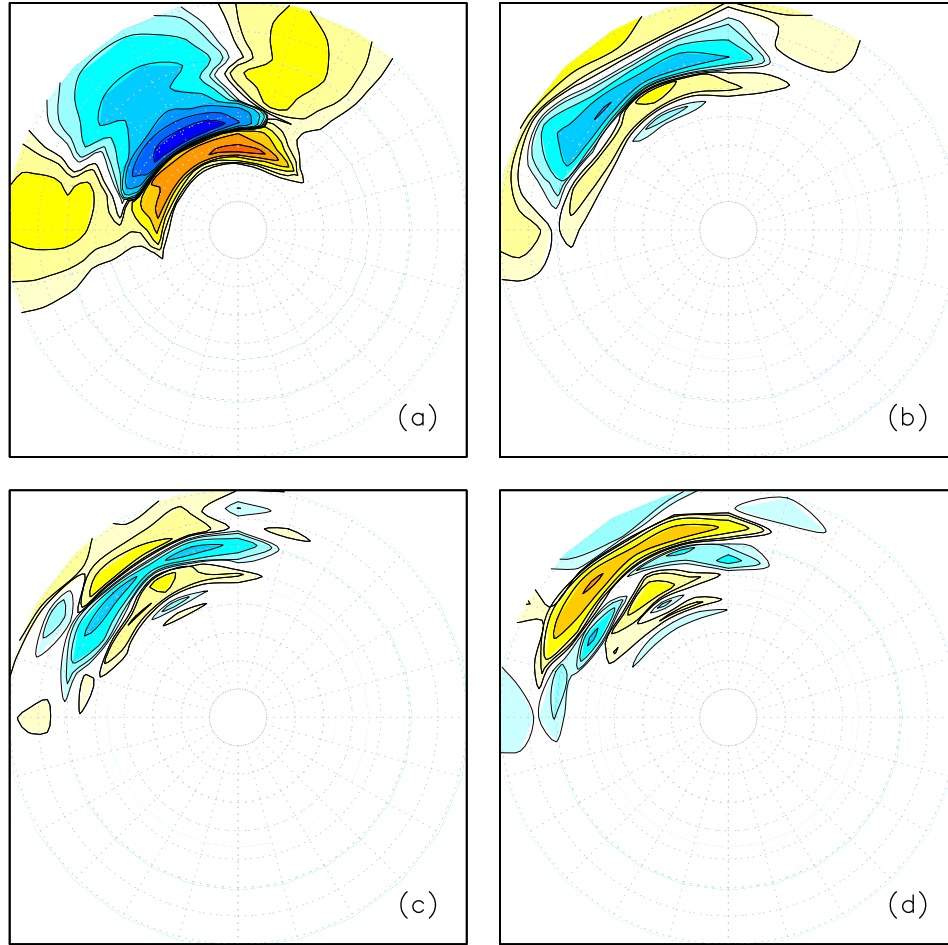
Fig. 5.12 : Nonlinear interactions used in computing the test spectrum (DIA panel a) corresponding to Fig.!5.9and the 'filter' source term for (b) $a_{34} = 1.00$, $C = 2.0 \times 10^8$. (c) $a_{34} = 0.50$, $C = 1.0 \times 10^9$. (d) $a_{34} = 0.05$, $C = 1.0 \times 10^{11}$.

This source term is defined by five free parameters, λ (or a_{34}), C, c_1, c_2 and c_3. The latter three parameters need to be chosen such that $\Phi(f_p) \approx 0$, $\Phi(3f_p) \approx 1$ and that $\Phi \approx 0.5$ for frequencies moderately larger than f_p. This can be achieved by setting

$$c_1 = 1.25 \quad , \quad c_2 = 1.50 \quad , \quad c_3 = 6.00 \tag{5.17}$$

Whereas these parameter settings could obviously be refined in a full model optimization, they will be kept at these values for the present study.

The values of λ and C define the shape and strength of the filtered nonlinear interactions. Figure 5.12a shows the full nonlinear interactions from the DIA corresponding to the test results presented in Fig. 5.9 obtained without filtering

for high frequencies. Note that compared to the latter figure, the frequency range displayed covers the entire discrete frequency range in the model (0.04 - 0.40 Hz), whereas the previous figure only displays source terms up to 0.25 Hz. Panels (b) through (d) show the filtered interaction for three values of a_{34}, with C chosen to result in a interaction strength comparable to that of the DIA (panel a).

The figure indicates that appropriate values of C increase dramatically with decreasing values of λ. This is at least partially due to the fact that interpolation values in the interactions, and the corresponding factors in the interpolation stencil (3.7) and (3.8) approach 0 for $a_{34} \rightarrow 0$ or $\lambda \rightarrow 0$. This implies some potential sensitivity of the filter to the actual spectral grid resolution. Part of the grid sensitivity related to the interpolation factors can be eliminated by defining the filter in terms of a_{34} instead of λ, in which case the interpolation factors become independent of the spectral grid resolution.

Figure 5.12 also indicates that the scales of the interactions become larger for $a_{34} > 0.5$, indicating that tentatively smaller values are more appropriate when the source term is used as a basis for a filter.

The filter function for the action spectrum in WAVEWATCH III is completed by a simple conversion of Eqs. (3.20) through (3.22) from spectral energy densities F to action densities N. The maximum changes $\Delta \tilde{N}_{m,1}$ and $\Delta \tilde{N}_{m,2}$ thus become

$$\tilde{N}_{m,1} = 0.5 \Delta \tilde{N}_{\max} \Phi(f) \quad , \tilde{N}_{m,2} = 0.5 \Delta \tilde{N}_{\max} \Phi(f) \quad , \tag{5.18}$$

or

$$\Delta \tilde{N}_{m,1} = \frac{|\Delta \tilde{N}_1| \, \Phi(f)}{|\Delta \tilde{N}_1| + |\Delta \tilde{N}_2|}) \quad , \Delta \tilde{F}_{m,2} = \frac{|\Delta \tilde{N}_2| \, \Phi(f)}{|\Delta \tilde{N}_1| + |\Delta \tilde{N}_2|}) \quad . \tag{5.19}$$

and the central energy changes corresponding to Eq. (3.17) become

$$\Delta \tilde{N}_{c,1} = \Delta \tilde{N}_{m,1} \tanh \left(\frac{\Delta \tilde{N}_1}{\Delta \tilde{N}_{m,1}} \right) \quad , \quad \Delta \tilde{N}_{c,2} = \Delta \tilde{N}_{m,2} \tanh \left(\frac{\Delta \tilde{N}_2}{\Delta \tilde{N}_{m,2}} \right) \quad . \tag{5.20}$$

Using the full implementation of this filter, an effective $S_{nl,e}$ source term can be defined as

$$S_{nl,e} = (N_f - N) \, \Delta t^{-1} \quad , \tag{5.21}$$

where N_f is the spectrum after filtering, and N is the original spectrum. When applied to Fig. 5.12 this effective source term is more than an order of magnitude smaller than the underlying source term of Fig. 5.12 (figure not presented here). This could be expected as time steps are based on nearly canceling source terms. Hence, time steps based on nonlinear interactions only would be an order of magnitude smaller than actual time steps, and similarly the filtering introduced here is expected to suppress the source term by an order of magnitude.

The next step is to test the effects of using the filtered source term as a smoother, and to address the various additional parameter settings in Eqs. (5.15) through (5.20). Still to be considered are the parameter setting for a_{34}, C and $\Delta \tilde{N}_{\max}$. First, the necessity and impact of setting $\Delta \tilde{N}_{\max}$ is addressed. Using a median value of $a_{34} = 0.50$ and effectively removing the asymptotic filter behavior by setting $\Delta \tilde{N}_{\max} = 10^6$, C is systematically increase with the intention to go from no impact to model instability. For $C = 10^7$ no impact on the model is notable (figures not presented here). This was expected since the corresponding strength of he interaction is smaller than the residual source term by up to an order of magnitude. For $C = 10^8$, the filtered nonlinear source term is of the same order of magnitude as the residual source term, and a small impact can be seen on the spectra shape and the resulting wave hight. For $C = 10^9$, the resulting source term is incompatible with the model time step, and the model integrations becomes unstable as expected (figures not presented here).

The next step of this experiment is to reduce $\Delta \tilde{N}_{\max}$ for $a_{34} = 0.50$ and $C = 10^9$, to assure that the corresponding limitation of the spectral changes indeed result in stable numerical results. Using $\Delta \tilde{N}_{\max} = 1.00$ is not expected to result in a stable filter, but for the most part result in stable model integration, with minor spurious secondary spectral peaks at high frequencies. This can be explained since the full interactions used in the model will counteract instabilities in the high-frequency filter. For $\Delta \tilde{N}_{\max} = 0.50$ the filter is theoretically stable, and indeed stable model results are obtained, with a minor squaring of spectral contours at high frequencies. For a more conservative $\Delta \tilde{N}_{\max} = 0.25$ the filter is actively engaged, but smooth spectral results with a minor impact on wave height (less than 2% reduction) is found. As a final test the strength C of the interactions is increased radically to $C = 10^{15}$, effectively applying the maximum filter strength consistently. For $\Delta \tilde{N}_{\max} = 0.50$ this results in stable but noisy model results, and for $\Delta \tilde{N}_{\max} = 0.25$ this results in stable and smooth model results. Hence the filter appears to work as designed, with required maximum filter strengths in the 0.25 to 0.50 range.

Also addressed in these experiments is the impact of choosing Eq. (5.18) or (5.19) to distribute maximum changes for the two quadruplet realizations. The latter approach give consistently smoother spectral results and is therefore used exclusively in the experiments below.

The above experiments have been repeated for other values of a_{34}. For $a_{34} = 1.00$ results are similar to those described above, with the following minor differences. The model integration appears fully stable with smooth high-frequency spectral contours for $\Delta \tilde{N}_{\max} = 1.00$ but with a somewhat larger impact on the wave height (3% reduction). For lower $\Delta \tilde{N}_{\max}$ the results convert to he results for $a_{34} = 0.50$. For $a_{34} = 0.05$ results are also generally similar, but with a smaller impact on the wave height. Results for $\Delta \tilde{N}_{\max} = 1.00$, 0.50 and 0.25 corresponding to the results presented in Fig. 5.9 are presented in Figs. 5.13

spectrum

wind source term

total source term

nonlinear interations

dissipation source term

Location (km): 2.1−0.9
Depth   :   60.0 m
Wind speed   :   20.0 m/s
Current vel. :   0.00 m/s
Wave height :   2.89 m
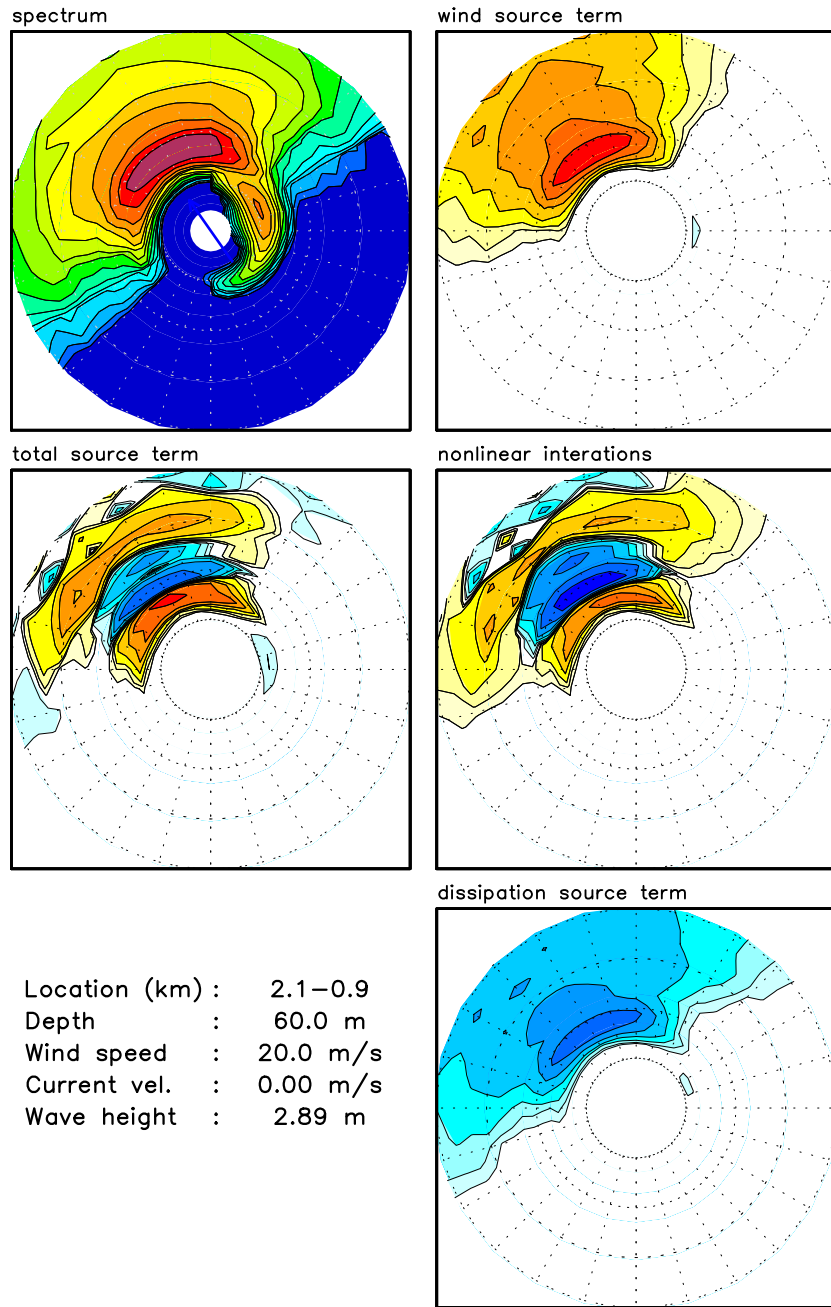
Fig. 5.13 : Spectrum and source terms from model run with traditional DIA (default WAVEWATCH III). with filter added with $a_{34} = 0.05$ and $\Delta \tilde{N}_{\max} = 1.00$ (compare to Fig. 5.9, note difference in frequency range of plots).

spectrum

wind source term

total source term

nonlinear interations

dissipation source term

Location (km)	:	2.1−0.9
Depth	:	60.0 m
Wind speed	:	20.0 m/s
Current vel.	:	0.00 m/s
Wave height	:	2.94 m
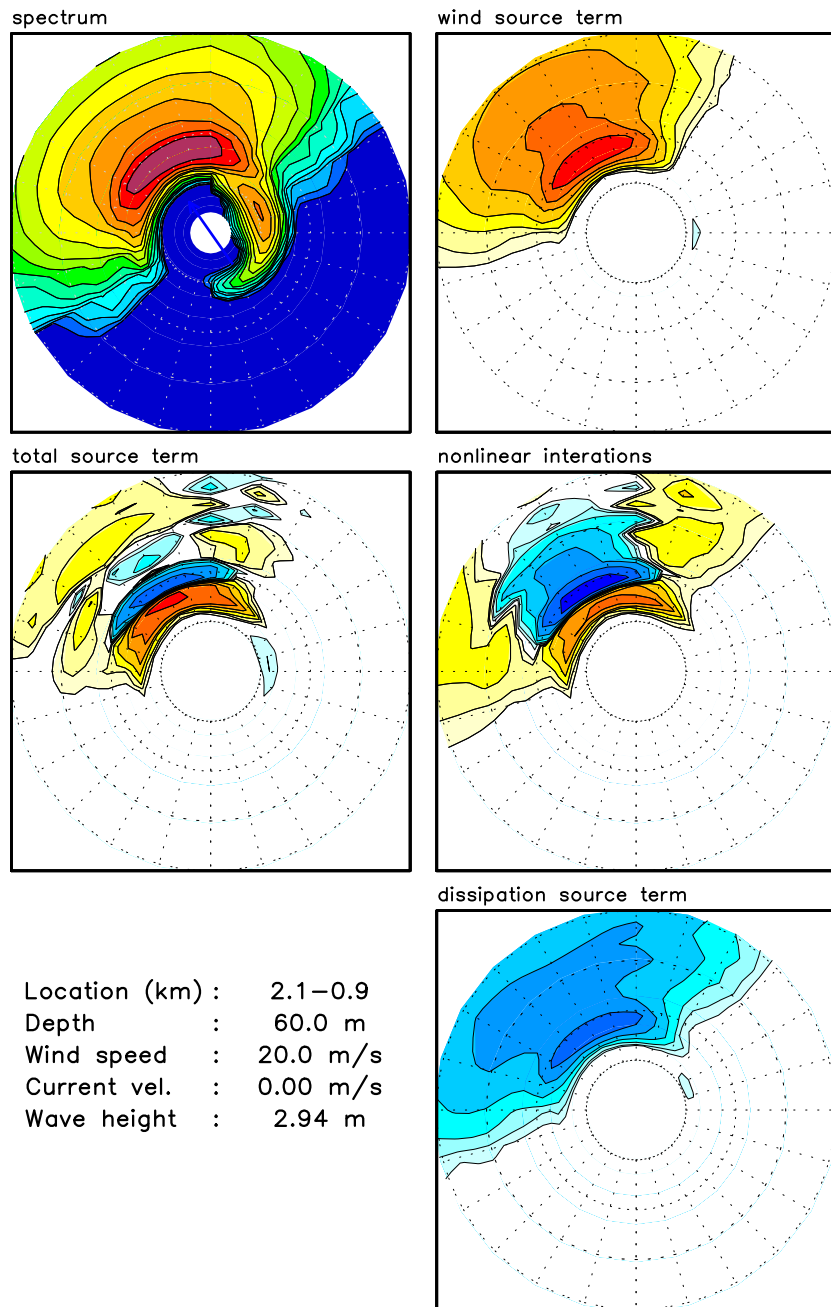
Fig. 5.14 : Like Fig. 5.13 with $\Delta\tilde{N}_{\max} = 0.50$.

spectrum

wind source term

total source term

nonlinear interations

dissipation source term

Location (km) :   2.1−0.9
Depth   :   60.0 m
Wind speed   :   20.0 m/s
Current vel. :   0.00 m/s
Wave height   :   2.93 m
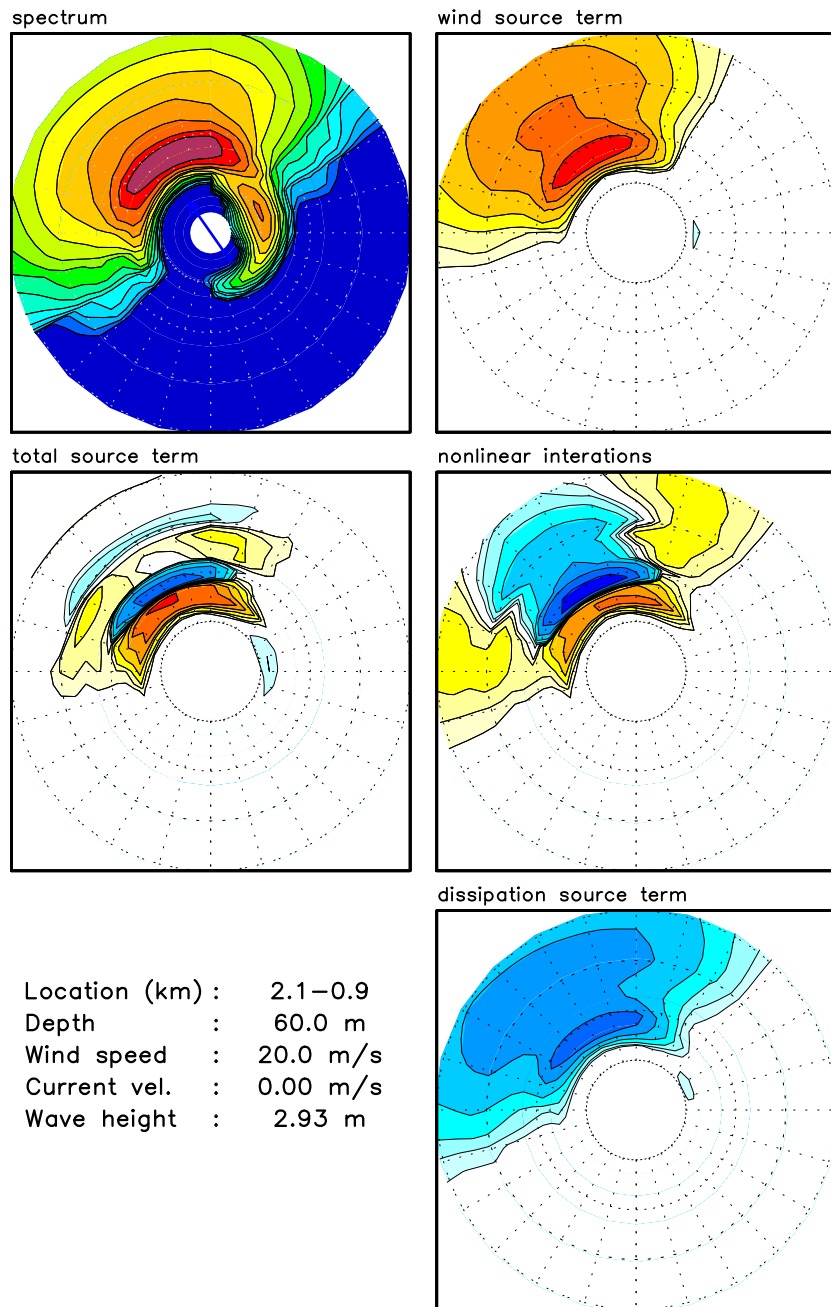
Fig. 5.15 : Like Fig. 5.13 with $\Delta \tilde{N}_{\max} = 0.25$.

108

spectrum

wind source term

total source term

nonlinear interations

dissipation source term

Location (km)	:	2.1−0.9
Depth	:	60.0 m
Wind speed	:	20.0 m/s
Current vel.	:	0.00 m/s
Wave height	:	2.92 m
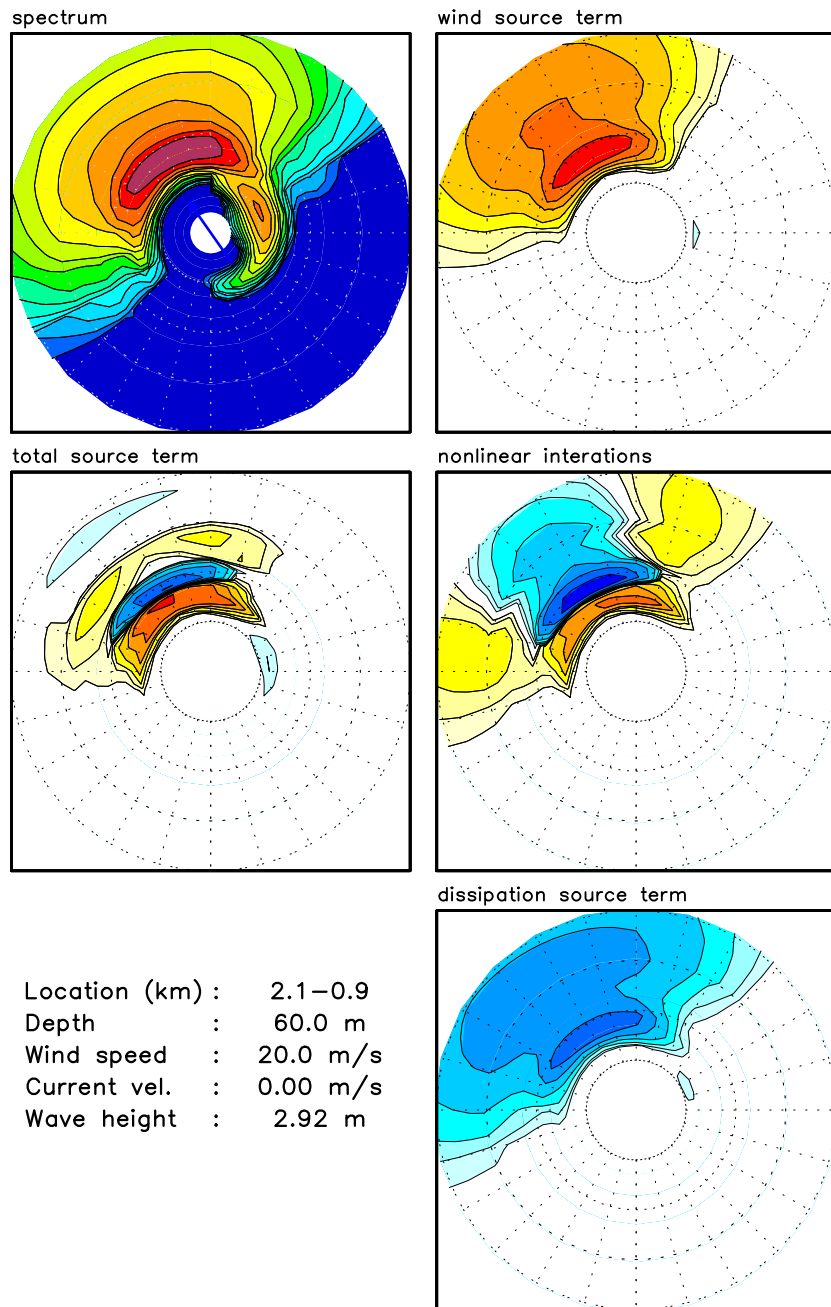
Fig. 5.16 : Like Fig. 5.13 with $\Delta \tilde{N}_{\max} = 0..$

through 5.15. Fig. 5.16 represents the case without filtering. Note that in the latter four figures the spectral range considers the entire discrete spectral domain to highlight high-frequency model behavior.

Figure 5.13 with $\Delta \tilde{N}_{\max} = 1.00$ clearly shows local instabilities in the spectrum for high frequencies (upper left panel). These instabilities are clearly shown in the source terms, particularly the nonlinear interactions, and manifest as bullseye patters in the latter. Note that the nonlinear interactions in this figure neither include, nor are corrected for the nonlinear behavior of the filter. However, noise introduced in the spectrum due to the filter does result in a direct response of the full nonlinear interaction term, shown here as the bullseye patterns. When the maximum filter strength is reduced to $\Delta \tilde{N}_{\max} = 0.50$ (Fig. 5.14), signatures of instability are removed from the spectrum, but can still be seen in the (nonlinear) source terms. For $\Delta \tilde{N}_{\max} = 0.25$ (Fig. 5.15), all signs of instability are removed from the source terms. However, the net effect of the filter can still be recognized from the fact that the nonlinear source term shows systematic differences when compared to the source terms obtained with the filter switched off ($\Delta \tilde{N}_{\max} = 0.$, Fig. 5.16). For this model setup, the noise disappears from the source terms for $\Delta \tilde{N}_{\max} \approx 0.35$ (figure not presented here).

Considering the above, it appears prudent to define the quadruplet by a_{34} instead of λ, and by choosing $a_{34} << 1$. In the latter case, the averaging stencil reduced from a nine-point stencil to a five point stencil [see Eqs. (3.10) and (3.11)], which allows for a more efficient implementation. Optimization of the code largely follows that of the generalized MDIA of Fig. 5.8, and will not be discussed in much detail here. The only important modification made during optimization has its root in the fact that the hyperbolic tangents function in Eq. (5.20) represents a disproportionally large part of the computational effort of the algorithm. Replacing this equation by a simple limiter

$$-\Delta \tilde{N}_{m,1} \leq \Delta \tilde{N}_{c,1} \leq \Delta \tilde{N}_{m,1} \quad , \quad -\Delta \tilde{N}_{m,2} \leq \Delta \tilde{N}_{c,2} \leq \Delta \tilde{N}_{m,2} \tag{5.22}$$

significantly reduces the cost of the algorithm, while requiring slightly lower values of $\Delta \tilde{N}_{\max}$ for smooth results. The computational cost of the resulting algorithm is depending on the local wind speed. For strongly forced conditions, the cost it roughly half of that of the traditional DIA. For small wind speeds, most computations can be avoided, and the cost of the algorithm becomes trivial compared to the traditional DIA. Tentative default parameter setting are given by Eq. (5.17) and by

$$a_{34} = 0.05 \quad , \quad C = 10^{10} \quad , \quad \Delta \tilde{N}_{\max} = 0.25 \tag{5.23}$$

which results in borderline unstable results without setting $\Delta \tilde{N}_{\max}$, and which is properly stabilized with this setting of $\Delta \tilde{N}_{\max}$ for the test model integration used

in the previous figures. This finalizes the nonlinear filtering approach introduced here.

This filter can be used in several ways. In combination with the generalized MDIA developed in this report, it may be used in two ways. It may improve high-frequency behavior of the resulting model, and it might result in larger time steps in the model, thus improving the overall model economy. Both possible applications need to be considered in a holistic model optimization as introduced in Part 2.

Another application may be in combination with a Neural Network Interaction Approximation (NNIA) as discussed in Tolman et al. (2005) and Tolman and Krasnopolsky (2004). The latter paper indicates that a hybrid NNIA with an internal quality control that reverts to a full interaction computation in cases where the NNIA is inaccurate results in stable model computations. However, the computations also show that the NNIA has an intrinsic problem with stabilizing the high-frequency tail of the spectrum. Tentatively, the filter technique introduced here can be used to explicitly stabilize the tail of the spectrum, and could therefore be a crucial part of a hybrid NNIA. This concept is outside the scope of the present paper and will not be pursued further here.

This page is intentionally left blank.

6   Summary and conclusions

The present report is the third in a series assessing the potential of the Discrete Interaction Approximation for representing nonlinear interactions in wind wave models. It addresses generalization of the DIA with multiple representative quadruplets to arbitrary depth. Starting form the original DIA as introduced by Hasselmann et al. (1985), the DIA equations are derived for arbitrary depths and arbitrary definitions of the wave spectrum and spectral space. Attention is given to:

- Quadruplet layout as a function of finite depth and sampling of spectral space by such quadruplets.

- Effects of spectral discretization on conservation properties of the nonlinear interactions.

- The use of multiple representative quadruplets.

- Effects of he choice of the spectrum and spectral space.

- Scaling considerations for finite depth conditions.

Using systematic testing by incrementally including shallow water aspects into the DIA, it is shown that a full shallow water expression for the DIA is essential, and that in particular details of the scaling function are essential for a well-behaved source term parameterization.

A two-part scaling function is needed to generate a DIA with proper scaling behavior for all depths. The two parts of the scaling function represent asymptotic behavior for deep and shallow water, respectively. It should also be noted that the shallow water realizations of the nonlinear four-wave interactions are generally not a dominant physical process. Therefore, ignoring the shallow water part of the scaling function in effect will reduce a non-relevant source term in strength, and hence be physically acceptable in most model applications.

Experiments with using the full interaction strength G in combination with a single representative quadruplet were unsuccessfully.

Several more conclusions can be drawn from the optimization of the resulting DIA. It was found that the choice of spectrum and spectral space has a distinct impact on the resulting interactions, most likely due to an interplay between small numerical interpolation differences and strong nonlinear interactions in the physical process described. It was also found that the triplet method for optimizing nonlinear interactions (Snyder et al., 1993, 1998; Van Vledder, 2005) may be effective for a traditional (multiple) DIA, but is not efficient for the generalized DIA presented here.

Experiments with numerical optimization furthermore show that an optimized generalized DIA configured like the traditional DIA requires approximately twice the computing time of the latter, that generalizing the quadruplet layout increases the costs by an additional factor of just below two, and that the costs of the optimized MDIA scales linearly with the number of representative quadruplet realizations.

The present study also addresses diffusion approaches as parameterizations of nonlinear interactions (e.g., Hasselmann et al., 1985; Zakharov and Pushkarev, 1999; Jenkins and Phillips, 2001). It is shown that a simple linear diffusion style operator is obtained from a conventional DIA with a traditional one-parameter quadruplet that is not resolved by the discrete spectral grid. Such a diffusion operator shares all conservation properties with the exact interactions.

Generally, diffusion operators are considered insufficiently accurate for application as a interaction parameterization. However, the diffusion operator defined here can easily be converted into a high-frequency filter, with properties consistent with the properties of the nonlinear interactions. Such a filter can be used either in conjunction with a multiple DIA, or, for instance, in combination with a Neural Network Interaction approximation (Tolman et al., 2005; Tolman and Krasnopolsky, 2004). The latter potential application will be addressed elsewhere.

This high-frequency filter is no necessarily convergent, i.e., it may have a nett effect on the model integration even for time steps approaching 0. However, since the strength of the filter is typically compatible with the strength of the residual source term (wind + interactions + dissipation), it is expected to be small compared to the actual interactions. Hence, its impact on the mean solution is expected to be small to negligent, as has been demonstrated in the model integration test performed here.

The present study focuses on scaling behavior, not on the parameter optimization of the generalized multiple DIA. As was demonstrated in previous parts of this study, such an optimization will need to consider full model integration, rather than individual spectra and source terms. Such a parameter optimization will be performed in the next part of this study.

References

Booij, N., R. C. Ris and L. H. Holthuijsen, 1999: A third-generation wave model for coastal regions, Part I, model description and validation. *J. Geophys. Res.*, **104**, 7649–7666.

Bretherthon, F. P. and C. J. R. Garrett, 1968: Wave trains in inhomogeneous moving media. *Proc. Roy. Soc. London*, **A 302**, 529–554.

Dungey, J. C. and W. H. Hui, 1979: Nonlinear energy transfer in narrow gravity wave spectrum. *Proc. Roy. Soc. London*, **A 368**, 239–265.

Fletcher, C. A. J., 1988: *Computational techniques for fluid dynamics, part I and II.* Springer, 409+484 pp.

Hargreaves, J. C. and J. D. Annan, 1998: Integration of source terms in WAM. in *Proceedings of the 5th International Workshop on Wave Forecasting and Hindcasting*, pp. 128–133.

Hargreaves, J. C. and J. D. Annan, 2001: Comments on improvement of the short fetch behavior in the WAM model. *J. Atmos. Oceanic Techn.*, **18**, 711–715.

Hasselmann, D. E., M. Dunckel and J. A. Ewing, 1980: Directional wave spectra observed during JONSWAP 1973. *J. Phys. Oceanogr.*, **10**, 1264–1280.

Hasselmann, K., 1960: Grundgleichungen der seegangsvoraussage. *Schiffstechnik*, **1**, 191–195.

Hasselmann, K., 1962: On the non-linear transfer in a gravity wave spectrum, Part 1. General theory. *J. Fluid Mech.*, **12**, 481–500.

Hasselmann, K., 1963: On the non-linear transfer in a gravity wave spectrum, Part 2, Conservation theory, wave-particle correspondence, irreversibility. *J. Fluid Mech.*, **15**, 273–281.

Hasselmann, K., 1966: Feynman diagrams and interaction rules of wave-scattering processes. *Rev. Geophys. Space Phys.*, **4**, 1–32.

Hasselmann, K., T. P. Barnett, E. Bouws, H. Carlson, D. E. Cartwright, K. Enke, J. A. Ewing, H. Gienapp, D. E. Hasselmann, P. Kruseman, A. Meerburg, P. Mueller, D. J. Olbers, K. Richter, W. Sell and H. Walden, 1973: Measurements of wind-wave growth and swell decay during the Joint North Sea Wave Project (JONSWAP). *Ergaenzungsheft zur Deutschen Hydrographischen Zeitschrift, Reihe A(8)*, **12**, 95 pp.

Hasselmann, S. and K. Hasselmann, 1981: A symmetrical method of computing the nonlinear transfer in a gravity wave sperctrum. Hamb. Geophys. Einzelschriften, Reihe A: Wiss. Abhand. 52, 138 pp.

Hasselmann, S. and K. Hasselmann, 1985: Computations and parameterizations of the nonlinear energy transfer in a gravity-wave spectrum, Part I: A new method for efficient computations of the exact nonlinear transfer integral. *J. Phys. Oceanogr.*, **15**, 1369–1377.

Hasselmann, S., K. Hasselmann, J. H. Allender and T. P. Barnett, 1985: Computations and parameterizations of the nonlinear energy transfer in a gravity-

wave spectrum, Part II: parameterizations of the nonlinear energy transfer for application in wave models. *J. Phys. Oceanogr.*, **15**, 1378–1391.

Hersbach, H. and P. A. E. M. Janssen, 1999: Improvement of the short fetch behavior in the WAM model. *J. Atmos. Oceanic Techn.*, **16**, 884–892.

Herterich, K. and K. Hasselmann, 1980: A similarity relation for the nonlinear energy transfer in a finite-depth gravity-wave spectrum. *J. Fluid Mech.*, **97**, 215–224.

Jenkins, A. and O. M. Phillips, 2001: A simple formula for nonlinear wave-wave interactions. *Int. J. Offshore Polar Eng.*, **11**, 81–86.

Komen, G. J., L. Cavaleri, M. Donelan, K. Hasselmann, S. Hasselmann and P. E. A. M. Janssen, 1994: *Dynamics and modelling of ocean waves*. Cambridge University Press, 532 pp.

Resio, D. T. and W. Perrie, 1991: A numerical study of nonlinear energy fluxes due to wave-wave interactions. Part 1: Methodology and basic results. *J. Fluid Mech.*, **223**, 609–629.

Ris, R. C., L. H. Holthuijsen and N. Booij, 1999: A third-generation wave model for coastal regions, Part II: verification. *J. Geophys. Res.*, **104**, 7667–7681.

Snyder, R. L., R. B. Long and W. L. Neu, 1998: A fully nonlinear regional wave model for the Bight of Abaco 1. Nonlinear-transfer computation. *J. Geophys. Res.*, **103**, 3119–3141.

Snyder, R. L., W. C. Thacker, K. Hasselmann, S. Hasselmann and G. Barzel, 1993: Implementation of an efficient scheme for calculating nonlinear transfer from wave-wave interactions. *J. Geophys. Res.*, **98**, 14,507–14,525.

Tolman, H. L., 1992: Effects of numerics on the physics in a third-generation wind-wave model. *J. Phys. Oceanogr.*, **22**, 1095–1111.

Tolman, H. L., 2002a: Distributed memory concepts in the wave model WAVE-WATCH III. *Parallel Computing*, **28**, 35–52.

Tolman, H. L., 2002b: Limiters in third-generation wind wave models. *The Global Atmosphere and Ocean System*, **8**, 67–83.

Tolman, H. L., 2002c: User manual and system documentation of WAVEWATCH III version 2.22. Tech. Note 222, NOAA/NWS/NCEP/MMAB, 133 pp.

Tolman, H. L., 2003: Optimum Discrete Interaction Approximations for wind waves. Part 1: Mapping using inverse modeling. Tech. Note 227, NOAA/NWS/NCEP/MMAB, 57 pp. + Appendices.

Tolman, H. L., 2004: Inverse modeling of Discrete Interaction Approximations for nonlinear interactions in wind waves. *Ocean Mod.*, **6**, 405–422.

Tolman, H. L., 2005: Optimum Discrete Interaction Approximations for wind waves. Part 2: convergence of model integration. Tech. Note 247, NOAA/NWS/NCEP/MMAB, 74 pp. + Appendices.

Tolman, H. L., B. Balasubramaniyan, L. D. Burroughs, D. V. Chalikov, Y. Y. Chao, H. S. Chen and V. M. Gerald, 2002: Development and implementation of wind generated ocean surface wave models at NCEP. *Wea. Forecasting*, **17**,

311–333.

Tolman, H. L. and N. Booij, 1998: Modeling wind waves using wavenumber-direction spectra and a variable wavenumber grid. *The Global Atmosphere and Ocean System*, **6**, 295–309.

Tolman, H. L. and V. M. Krasnopolsky, 2004: Nonlinear interactions in practical wind wave models. in *8th international workshop on wave hindcasting and forecasting, JCOMM Tech. Rep. 29, WMO/TD-No. 1319*. Paper E1.

Tolman, H. L., V. M. Krasnopolsky and D. V. Chalikov, 2005: Neural Network approximations for nonlinear interactions in wind wave spectra: direct mapping for wind seas in deep water. *Ocean Mod.*, **8**, 253–178.

Tracy, B. and D. T. Resio, 1982: Theory and calculation of the nonlinear energy transfer between sea waves in deep water. WES Report 11, US Army Corps of Engineers.

Van Vledder, G. Ph., 2001: Extension of the Discrete Interaction Approximation for computing nonlinear quadruplet wave-wave interactions in operational wave prediction models. in *4th International Symposium on Ocean Wave Measurement and Analysis*, pp. 540–549. ASCE.

Van Vledder, G. Ph., 2002a: Improved parameterizations of nonlinear four wave interactions for application in operational wave prediction models. Report 151a, Alkyon, The Netherlands.

Van Vledder, G. Ph., 2002b: A subroutine version of the Webb/Resio/Tracy method for the computation of nonlinear quadruplet interactions in a wind-wave spectrum. Report 151b, Alkyon, The Netherlands.

Van Vledder, G. Ph., 2005: The triplet method for the computation of nonlinear four-wave interactions in discrete spectral wave models. in B. L. Edge and J. M. Hemsley, editors, *5th International Symposium on Ocean Wave Measurement and Analysis*. ASCE, Paper 48.

Van Vledder, G. Ph., 2006: The WRT method for the computation of non-linear four wave interactions in discrete spectral wave models. *Coastal Eng.*, **53**, 223–242.

WAMDIG, 1988: The WAM model – a third generation ocean wave prediction model. *J. Phys. Oceanogr.*, **18**, 1775–1809.

Webb, D. J., 1978: Non-linear transfers between sea waves. *Deep-Sea Res.*, **25**, 279–298.

Zakharov, V. E. and A. N. Pushkarev, 1999: Diffusion model of interacting gravity waves on the surface of a deep fluid. *Nonlinear Proc. Geoph.*, **6**, 1–10.

This page is intentionally left blank.